Electron Spin Resonance

by

Dr. Phil Rieger
Brown University

Electron Spin Resonance

1. Introduction

Electron spin resonance (ESR) spectroscopy has been used for over 50 years to study a variety of paramagnetic species. In this chapter, we will focus on the spectra of organic and organotransition metal radicals and coordination complexes. Although ESR spectroscopy is supposed to be a mature field with a fully developed theory [1], there have been some surprises as organometallic problems have explored new domains in ESR parameter space. We will start with a synopsis of the fundamentals of ESR spectroscopy. For further details on the theory and practice of ESR spectroscopy, refer to one of the excellent texts on ESR spectroscopy [2-9].

The electron spin resonance spectrum of a free radical or coordination complex with one unpaired electron is the simplest of all forms of spectroscopy. The degeneracy of the electron spin states characterized by the quantum number, $m_S = \pm 1/2$, is lifted by the application of a magnetic field and transitions between the spin levels are induced by radiation of the appropriate frequency, as shown in Figure 1.1. If unpaired electrons in radicals were indistinguishable from free electrons, the only information content of an ESR spectrum would be the integrated intensity, proportional to the radical con-centration. Fortunately, an un-paired electron interacts with its environment, and the details of ESR spectra depend on the nature of those interactions.
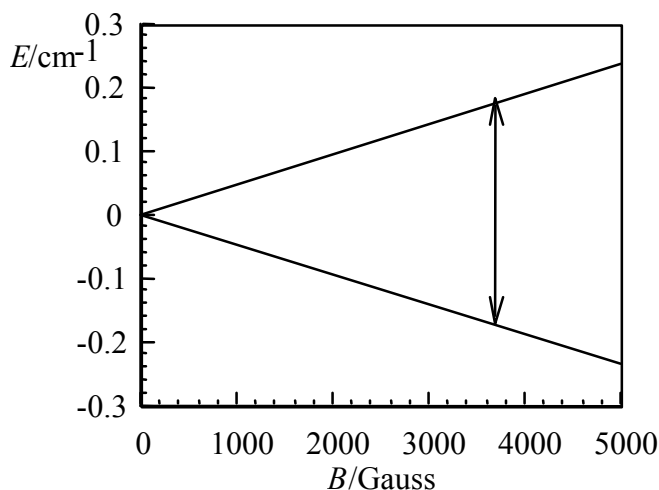

Figure 1.1. Energy levels of an electron placed in a magnetic field. The arrow shows the transitions induced by 0.315 cm^{-1} radiation.

There are two kinds of environmental interactions which are commonly important in the ESR spectrum of a free radical: (i) To the extent that the unpaired electron has unquenched orbital angular momentum, the total magnetic moment is different from the spin-only moment (either larger or smaller, depending on how the angular momentum vectors couple). It is customary to lump the orbital and spin angular momenta together in an effective spin and to treat the effect as a shift in

the energy of the spin transition. (ii) The electron spin energy levels are split by interaction with nuclear magnetic moments—the nuclear hyperfine interaction. Each nucleus of spin I splits the electron spin levels into $(2I + 1)$ sublevels. Since transitions are observed between sublevels with the same values of m_I, nuclear spin splitting of energy levels is mirrored by splitting of the resonance line.

2. The E.S.R. Experiment

When an electron is placed in a magnetic field, the degeneracy of the electron spin energy levels is lifted* as shown in Figure 1 and as described by the **spin Hamiltonian**:

$$\hat{\boldsymbol{H}}_s = g\mu_B B\, \hat{\boldsymbol{S}}_z \tag{2.1}$$

In eq (2.1), g is called the **g-value** ($g_e = 2.00232$ for a free electron), μ_B is the Bohr magneton (9.274×10^{-28} J G^{-1}), B is the magnetic field strength in Gauss, and $\boldsymbol{S_z}$ is the z-component of the spin angular momentum operator (the field defines the z-direction). The electron spin energy levels are easily found by application of $\hat{H}_s$ to the electron spin eigenfunctions corresponding to $m_S = \pm 1/2$:

$$\hat{\boldsymbol{H}}_s \left|\pm\tfrac{1}{2}\right\rangle = \pm\tfrac{1}{2}\,g\mu_B B \left|\pm\tfrac{1}{2}\right\rangle = E_\pm \left|\pm\tfrac{1}{2}\right\rangle$$

Thus

$$E_\pm = \pm\tfrac{1}{2}\,g\mu_B B \tag{2.2}$$

The difference in energy between the two levels,

$$\Delta E = E_+ - E_- = g\mu_B B$$

corresponds to the energy of a photon required to cause a transition:

$$h\nu = g\mu_B B \tag{2.3}$$

or in wave numbers,

$$\tilde{\nu} = \frac{g\mu_B B}{hc} \tag{2.4}$$

where $g_e\mu_B/hc = 0.9348 \times 10^{-4}$ cm^{-1}G^{-1}. Since the g-values of organic and organometallic free radicals are usually in the range 1.8 - 2.2, the free electron value is a good starting point for describing the experiment.

Magnetic fields of up to ca. 15000 G are easily obtained with an iron-core electromagnet; thus we could use radiation with $\tilde{\nu}$ up to 1.4 cm^{-1} ($\nu < 42$ GHz or $\lambda >$

---

* Energy level splitting in a magnetic field is called the **Zeeman effect**, and the Hamiltonian of eq (2.1) is sometimes referred to as the electron Zeeman Hamiltonian.

0.71 cm).   Radiation with this kind of wavelength is in the microwave region. Microwaves are normally handled using waveguides designed to transmit over a relatively narrow frequency range. Waveguides look like rectangular cross-section pipes with dimensions on the order of the wavelength to be transmitted. As a practical matter, waveguides can't be too big or too small—1 cm is a bit small and 10 cm a bit large; the most common choice, called X-band microwaves, has λ in the range 3.0 - 3.3 cm (ν ♠ 9 - 10 GHz); in the middle of X-band, the free electron resonance is found at 3390 G.

Although X-band is by far the most common, ESR spectrometers are available commercially in several frequency ranges:

Designation	ν/GHz	λ/cm	B(electron)/G
S	3.0	10.0	1070
X	9.5	3.15	3390
K	23	1.30	8200
Q	35	0.86	12500

Sensitivity

As for any quantum mechanical system interacting with electromagnetic radiation, a photon can induce either absorption or emission. The experiment detects net absorption, *i.e.*, the difference between the number of photons absorbed and the number emitted. Since absorption is proportional to the number of spins in the lower level and emission is proportional to the number of spins in the upper level, net absorption is proportional to the difference:

$$\text{Net Absorption} \propto N_- - N_+$$

The ratio of populations at equilibrium is given by the Boltzmann distribution

$$\frac{N_+}{N_-} = e^{-\Delta E/k_B T} = e^{-g\mu_B B/k_B T}$$

$$(2.5)$$

For ordinary temperatures and ordinary magnetic fields, the exponent is very small and the exponential can be accurately approximated by the expansion, e^{-x} ♠ $1 - x$. Thus

$$\frac{N_+}{N_-} \approx 1 - \frac{g\mu_B B}{k_B T}$$

Since N_- ♠ N_+ ♠ $N/2$, the population difference can be written

$$N_- - N_+ = N_- \left[1 - \left(1 - \frac{g\mu_B B}{k_B T} \right) \right] = \frac{N g \mu_B B}{2 k_B T}$$

$$(2.6)$$

This expression tells us that ESR sensitivity (net absorption) increases with decreasing temperature and with increasing magnetic field strength. Since field is

proportional to microwave frequency, in principle sensitivity should be greater for K-band or Q-band spectrometers than for X-band. However, since the K- or Q-band waveguides are smaller, samples are also necessarily smaller, usually more than canceling the advantage of a more favorable Boltzmann factor.

Under ideal conditions, a commercial X-band spectrometer can detect the order of 10^{12} spins (10^{-12} moles) at room temperature. By ideal conditions, we mean a single line, on the order of 0.1 G wide; sensitivity goes down roughly as the reciprocal square of the linewidth. When the resonance is split into two or more hyperfine lines, sensitivity goes down still further. Nonetheless, ESR is a remarkably sensitive technique, especially compared with NMR.

Saturation

Because the two spin levels are so nearly equally populated, magnetic resonance suffers from a problem not encountered in higher energy forms of spectroscopy: An intense radiation field will tend to equalize the populations, leading to a decrease in net absorption; this effect is called "saturation". A spin system returns to thermal equilibrium via energy transfer to the surroundings, a rate process called **spin-lattice relaxation**, with a characteristic time, T_1, the spin-lattice relaxation time (rate constant = $1/T_1$). Systems with a long T_1 (*i.e.*, spin systems weakly coupled to the surroundings) will be easily saturated; those with shorter T_1 will be more difficult to saturate. Since spin-orbit coupling provides an important energy transfer mechanism, we usually find that odd-electron species with light atoms (*e.g.*, organic radicals) have long T_1's, those with heavier atoms (*e.g.*, organotransition metal radicals) have shorter T_1's. The effect of saturation is considered in more detail in Appendix I, where the phenomenological Bloch equations are introduced.

Nuclear Hyperfine Interaction

When one or more magnetic nuclei interact with the unpaired electron, we have another perturbation of the electron energy, *i.e.*, another term in the spin Hamiltonian:

$$\hat{\boldsymbol{H}}_s = g\mu_B B \hat{\boldsymbol{S}}_z + A\vec{\boldsymbol{I}}\cdot\vec{\boldsymbol{S}}$$

(2.7)

(Strictly speaking we should include the nuclear Zeeman interaction, $\gamma B I_z$. However, in most cases the energy contributions are negligible on the ESR energy scale, and, since observed transitions are between levels with the same values of m_I, the nuclear Zeeman energies cancel in computing ESR transition energies.) Expanding the dot product and substituting the raising and lowering operators for S_x, S_y, I_x, and I_y ($\hat{S}_\pm = \hat{S}_x \pm i\hat{S}_y$, $\hat{I}_\pm = \hat{I}_x \pm i\hat{I}_y$), we have

$$\hat{\boldsymbol{H}}_s = g\mu_B B \hat{\boldsymbol{S}}_z + A\hat{\boldsymbol{I}}_z\hat{\boldsymbol{S}}_z + \frac{1}{2}\left(\hat{\boldsymbol{I}}_+\hat{\boldsymbol{S}}_- + \hat{\boldsymbol{I}}_-\hat{\boldsymbol{S}}_+\right)$$

(2.8)

Suppose that the nuclear spin is 1/2; operating on the spin functions, $\left| m_S, m_I \right\rangle$ we get:

$$\hat{H}_s \left| \tfrac{1}{2},\tfrac{1}{2} \right\rangle = \left(\tfrac{1}{2} g\mu_B B + \tfrac{1}{4} A \right) \left| \tfrac{1}{2},\tfrac{1}{2} \right\rangle$$

$$\hat{H}_s \left| \tfrac{1}{2},-\tfrac{1}{2} \right\rangle = \left(\tfrac{1}{2} g\mu_B B - \tfrac{1}{4} A \right) \left| \tfrac{1}{2},-\tfrac{1}{2} \right\rangle + \tfrac{1}{2} A \left| -\tfrac{1}{2},\tfrac{1}{2} \right\rangle$$

$$\hat{H}_s \left| -\tfrac{1}{2},\tfrac{1}{2} \right\rangle = \left(-\tfrac{1}{2} g\mu_B B - \tfrac{1}{4} A \right) \left| -\tfrac{1}{2},\tfrac{1}{2} \right\rangle + \tfrac{1}{2} A \left| \tfrac{1}{2},-\tfrac{1}{2} \right\rangle$$

$$\hat{H}_s \left| -\tfrac{1}{2},-\tfrac{1}{2} \right\rangle = \left(-\tfrac{1}{2} g\mu_B B + \tfrac{1}{4} A \right) \left| -\tfrac{1}{2},-\tfrac{1}{2} \right\rangle$$

The Hamiltonian matrix thus is

$$\begin{pmatrix} \tfrac{1}{2} g\mu_B B + \tfrac{1}{4} A & 0 & 0 & 0 \\ 0 & \tfrac{1}{2} g\mu_B B - \tfrac{1}{4} A & \tfrac{1}{2} A & 0 \\ 0 & \tfrac{1}{2} A & -\tfrac{1}{2} g\mu_B B - \tfrac{1}{4} A & 0 \\ 0 & 0 & 0 & -\tfrac{1}{2} g\mu_B B + \tfrac{1}{4} A \end{pmatrix}$$

$$(2.9)$$

If the hyperfine coupling is sufficiently small, $A \ll g\mu_B B$, the diagonal elements, which correspond to the energies to first-order in perturbation theory, will be sufficiently accurate:

$$E = \pm \tfrac{1}{2} g\mu_B B \pm \tfrac{1}{4} A$$

$$(2.10)$$

However, for large A, the matrix must be diagonalized. This is easy when there is only one hyperfine coupling:

$$E\left(\tfrac{1}{2},\tfrac{1}{2} \right) = \tfrac{1}{2} g\mu_B B + \tfrac{1}{4} A$$

$$(2.11a)$$

$$E\left(-\tfrac{1}{2},-\tfrac{1}{2} \right) = -\tfrac{1}{2} g\mu_B B + \tfrac{1}{4} A$$

$$(2.11b)$$

$$E\left(\tfrac{1}{2},-\tfrac{1}{2} \right) = -\tfrac{1}{4} A + \tfrac{1}{2} g\mu_B B \sqrt{1 + \left(\frac{A}{g\mu_B B} \right)^2}$$

$$(2.11c)$$

$$E\left(-\tfrac{1}{2},\tfrac{1}{2} \right) = -\tfrac{1}{4} A - \tfrac{1}{2} g\mu_B B \sqrt{1 + \left(\frac{A}{g\mu_B B} \right)^2}$$

$$(2.11d)$$

These equations are a special case of the general solution to eq (2.8), called the **Breit-Rabi equation** (10). The energies are plotted as functions of B in Figure 2.1 for $g = 2.00$, $A = 0.1$ cm^{-1}. Notice that at zero field, there are two levels corres-

ponding to a spin singlet ($E = -3A/4$) and a triplet ($E = +A/4$). At high field, the four levels divide into two higher levels ($m_S = +1/2$) and two lower levels ($m_S = -1/2$) and approach the first-order results, eq (2.10) (the first-order solution is called the high-field approx-imation). In order to conserve angular momentum, transitions among these levels can involve only one spin flip; in other words, the selection rules are $\Delta m_S = \pm 1$, $\Delta m_I = 0$ (ESR transitions) or $\Delta m_S = 0$, $\Delta m_I = \pm 1$ (NMR transitions); the latter involves much lower energy photons, and, in practice, only the $\Delta m_S = \pm 1$ transitions are observed. In Figure 2.1, these transitions are marked for a photon energy of 0.315 cm^{-1}.
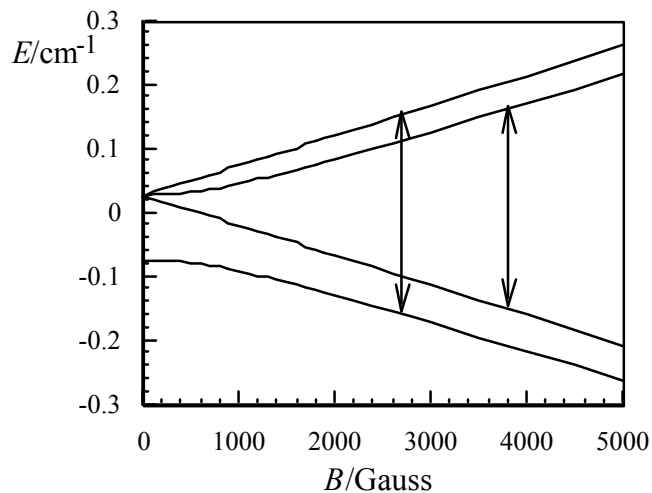

Figure 2.1. Energy levels for an electron interacting with a spin 1/2 nucleus, $g = 2.00$, $A = 0.10$ cm^{-1}. The arrows show the transitions induced by 0.315 cm^{-1} radiation.

3. Operation of an ESR Spectrometer

Although many spect-rometer designs have been produced over the years, the vast majority of laboratory instruments are based on the simplified block diagram shown in Figure 3.1. Microwaves are generated by the Klystron tube and the power level adjusted with the Attenuator. The Circulator behaves like a traffic circle: microwaves entering from the Klystron are routed toward the Cavity where the sample is
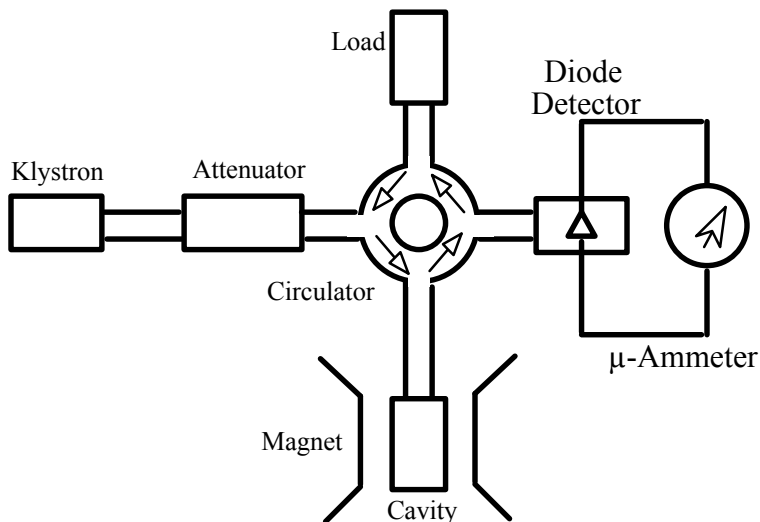

Figure 3.1. Block diagram of an ESR spectrometer.

mounted. Microwaves reflected back from the cavity (less when power is being absorbed) are routed to the diode detector, and any power reflected from the diode is

absorbed completely by the Load. The diode is mounted along the *E*-vector of the plane-polarized microwaves and thus produces a current proportional to the microwave power reflected from the cavity. Thus, in principle, the absorption of microwaves by the sample could be detected by noting a decrease in current in the microammeter. In practice, of course, such a d.c. measurement would be far too noisy to be useful.

The solution to the signal-to-noise ratio problem is to introduce small amplitude field modulation. An oscillating magnetic field is super-imposed on the d.c. field by means of small coils, usually built into the cavity walls. When the field is in the vicinity of a resonance line, it is swept back and forth through part of the line, leading to an a.c. component in the diode current. This a.c. component is amplified using a frequency selective amplifier, thus eliminating a great deal of noise. The modulation amplitude is normally less than the line width. Thus the detected
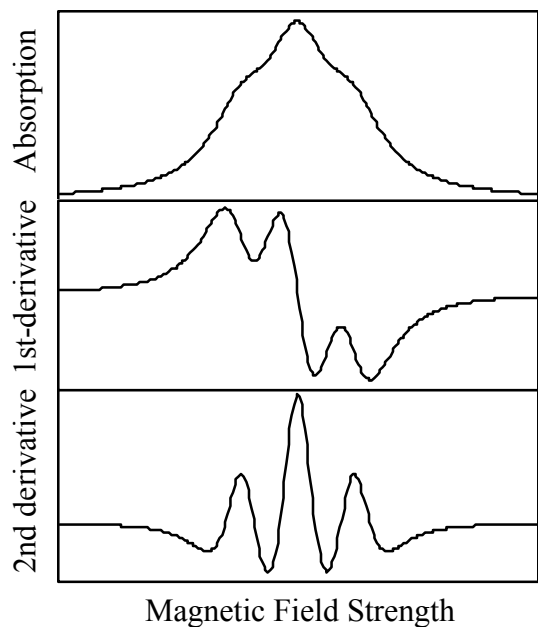

Figure 3.2. Small-amplitude field modulation converts absorption curve to first-derivative.

a.c. signal is proportional to the ***change*** in sample absorption. As shown in Figure 3.2, this amounts to detection of the first derivative of the absorption curve.

It takes a little practice to get used to looking at first-derivative spectra, but there is a distinct advantage: first-derivative spectra have much better apparent resolution than do absorption spectra. Indeed, second-derivative spectra are even better resolved (though the signal-to-noise ratio decreases on further differentiation).

Figure 3.3. First-derivative curves show better apparent resolution than do absorption curves.

The microwave-generating klystron tube requires a bit of explanation. A schematic drawing of the klystron is shown in Figure 3.3. There are three electrodes: a heated cathode from which electrons are emitted, an anode to collect
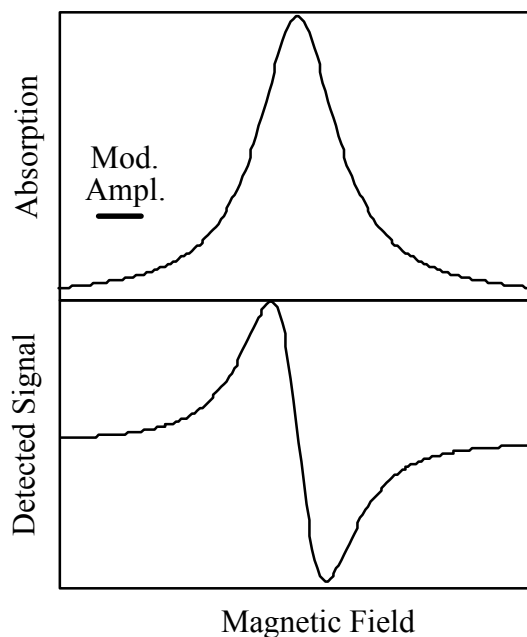
the electrons, and a highly negative reflector electrode which sends those electrons which pass through a hole in the anode back to the anode. The motion of the charged electrons from the hole in the anode to the reflector and back to the anode generates a oscillating electric field and thus electromagnetic radiation. The transit time from the hole to the reflector and back again corresponds to the period of

Figure 3.3. Schematic drawing of a microwave-generating klystron tube.

oscillation (1/ν). Thus the microwave frequency can be tuned (over a small range) by adjusting the physical distance between the anode and the reflector or by adjusting the reflector voltage. In practice, both methods are used: the metal tube is distorted mechanically to adjust the distance (a coarse frequency adjustment) and the reflector voltage is adjusted as a fine control.
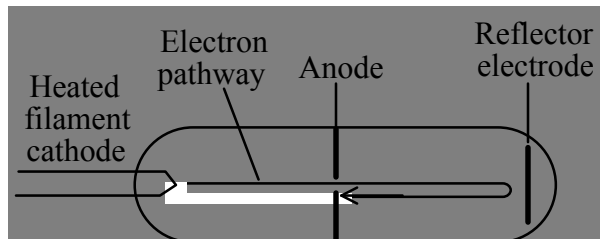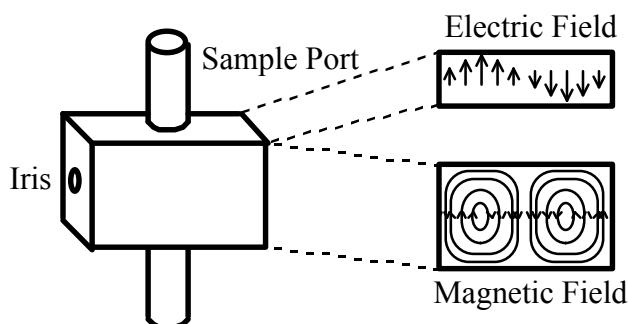

Figure 3.4. Microwave cavity.

The sample is mounted in the microwave cavity, shown in Figure 3.4. The cavity is a rectangular metal box, exactly one wavelength in length. An X-band cavity has dimensions of about $1 \times 2 \times 3$ cm. The electric and magnetic fields of the standing wave are shown in the figure. Note that the sample is mounted in the electric field nodal plane, but at a maximum in the magnetic field.

Since the cavity length is not adjustable but it must be exactly one wavelength, the spectrometer must be tuned such that the klystron frequency is equal to the cavity resonant frequency. The tune-up procedure usually includes observing the klystron power mode. That is, the klystron reflector voltage is swept, and the diode current is plotted on an oscilloscope or other device. When the klystron frequency is close to the

Figure 3.5. Klystron mode and cavity dip.

cavity resonant frequency, much less power is reflected from the cavity to the diode, resulting in a dip in the power mode as shown in Figure 3.5. The "cavity dip" is centered on the power mode using the coarse mechanical frequency adjustment with the reflector voltage used to fine tune the frequency.

4. Isotropic ESR Spectra

An isotropic ESR spectrum—the spectrum of a freely tumbling radical in liquid solution—can contain several kinds of chemically useful information: (i) The hyperfine coupling pattern provides information on the numbers and kinds of magnetic nuclei with which the unpaired electron interacts. (ii) The spacing of the lines and the center of gravity of the spectrum yield the hyperfine coupling constants, $\langle A_i \rangle$, and g-value, $\langle g \rangle$, which are related to the way in which the unpaired electron spin density is distributed in the molecule. (iii) The integrated intensity of the spectrum is proportional to the concentration of radicals in the sample. (iv) The spectral linewidths are related to the rate of the rotational motions which average anisotropies in the g- and hyperfine matrices (see §5) and to the rates of fluxional processes which average nuclear positions in a radical. (v) The saturation behavior of a spectrum—the variation of integrated intensity with microwave power—is related to the spin-lattice relaxation time, a measure of the rate of energy transfer between the electron spin and its surroundings.

The degree to which these kinds of information have been exploited varies widely. Although experimentalists often make qualitative observations relating "strong" or "weak" spectra to chemical circumstances, quantitative applications of integrated intensities are rare in ESR studies. This could be a useful analytical approach in some cases. The interested reader is referred to Wertz and Bolton [5], who discuss the technique, point out the variables which must be controlled, and suggest intensity standards.

Largely because spin-orbit coupling results in spin state admixture, electronic spin-lattice relaxation times are normally short for species containing heavy atoms such as transition metals. This has two consequences. Short relaxation times mean that saturation problems, which plague ESR spectroscopists studying organic radicals and NMR spectroscopists in general, are largely absent in organometallic ESR studies. Thus spectra ordinarily can be recorded at full microwave power with salutary consequences for sensitivity. On the other hand, relaxation times are most easily determined by measuring spectral intensity as a function of microwave power in the saturation region. If relaxation times are short, very high power is required, out of the range of operation of most spectrometers.

Line Positions in Isotropic Spectra

ESR spectra of radicals in liquid solution are usually interpreted in terms of a spin Hamiltonian

$$\hat{\boldsymbol{H}}_s = \mu_B \langle g \rangle \, \vec{\mathbf{B}} \cdot \vec{\boldsymbol{S}} + \sum_i \langle A_i \rangle \, \vec{\boldsymbol{I}_i} \cdot \vec{\boldsymbol{S}}$$

(4.1)

where μ_B is the Bohr magneton. The first term of eq (4.1) represents the Zeeman interaction of the effective electron spin, $\vec{\boldsymbol{S}}$, and the applied magnetic field, $\mathbf{B}$, and the second represents the nuclear hyperfine interaction of $\vec{\boldsymbol{S}}$ and the nuclear spins, $\boldsymbol{I}_i$. The spectral information is contained in the parameters, $\langle g \rangle$, the effective gyromagnetic ratio or g-value, and $\langle A_i \rangle$, the electron-nuclear hyperfine coupling constant for nucleus i. Using spin functions based on the quantum numbers m_S and m_i, eq (4.1) can be used to compute energy levels. Equating energy differences for the allowed transitions ($\Delta m_S = \pm 1$, $\Delta m_i = 0$) with the microwave photon energy,

$$E(m_S = 1/2) - E(m_S = -1/2) = h\nu \tag{4.2}$$

the resonant magnetic field can be predicted. To first-order in perturbation theory, the resonant field is

$$B = B_0 - \sum_i \langle a_i \rangle m_i \tag{4.3}$$

where $B_0 = h\nu/\langle g \rangle \mu_B$ represents the center of the spectrum and $\langle a_i \rangle = \langle A_i \rangle/\langle g \rangle \mu_B$ is the hyperfine coupling constant in field units.

The coupling constant in eq (4.1) has energy units, but the energies are very small so that frequency (MHz) or wave number (10^{-4} cm^{-1}) units are more commonly used. Even more often, however, isotropic coupling constants are given in units of magnetic field strength, usually gauss, though SI purists sometimes use millitesla (1 mT = 10 G). Conversions from units of gauss to frequency or wave number units involves the g-value

$$\langle A \rangle/\text{MHz} = 2.8025 \, \langle g \rangle/g_e) \, \langle a \rangle/\text{G} \tag{4.4a}$$

$$\langle A \rangle/10^{-4} \text{ cm}^{-1} = 0.93480 \, \langle g \rangle/g_e) \, \langle a \rangle/\text{G} \tag{4.4b}$$

Note that coupling constants in 10^{-4} cm^{-1} are comparable in magnitude to those expressed in gauss. Although the units used for isotropic hyperfine coupling constants is largely a matter of taste, the components of an anisotropic hyperfine coupling matrix (see §5) should be given in frequency or wave number units unless the g-matrix is virtually isotropic.

Hyperfine Coupling Patterns

Nuclear hyperfine coupling results in a multi-line ESR spectrum, analogous to the spin-spin coupling multiplets of NMR spectra. ESR spectra are simpler to understand than NMR spectra in that second-order effects normally do not alter the intensities of components; on the other hand, ESR multiplets can be much more complex when the electron interacts with several high-spin nuclei, and, as we will see below, there can be considerable variation in linewidth within a spectrum.

When several magnetically equivalent nuclei are present in a radical, some of the multiplet lines are degenerate, resulting in variations in component intensity. Equivalent spin 1/2 nuclei such as ^{1}H, ^{19}F, or ^{31}P result in multiplets with intensities given by binomial coefficients (1:1 for two nuclei, 1:2:1 for two, 1:3:3:1 for three, 1:4:6:4:1 for four, etc.). One of the first aromatic organic radical anions studied by ESR spectroscopy was the naphthalene anion [11], the spectrum of which is shown in Figure 4.1. The spectrum consists of 25 lines, a quintet of quintets as expected for hyperfine coupling to two sets of four equivalent protons.
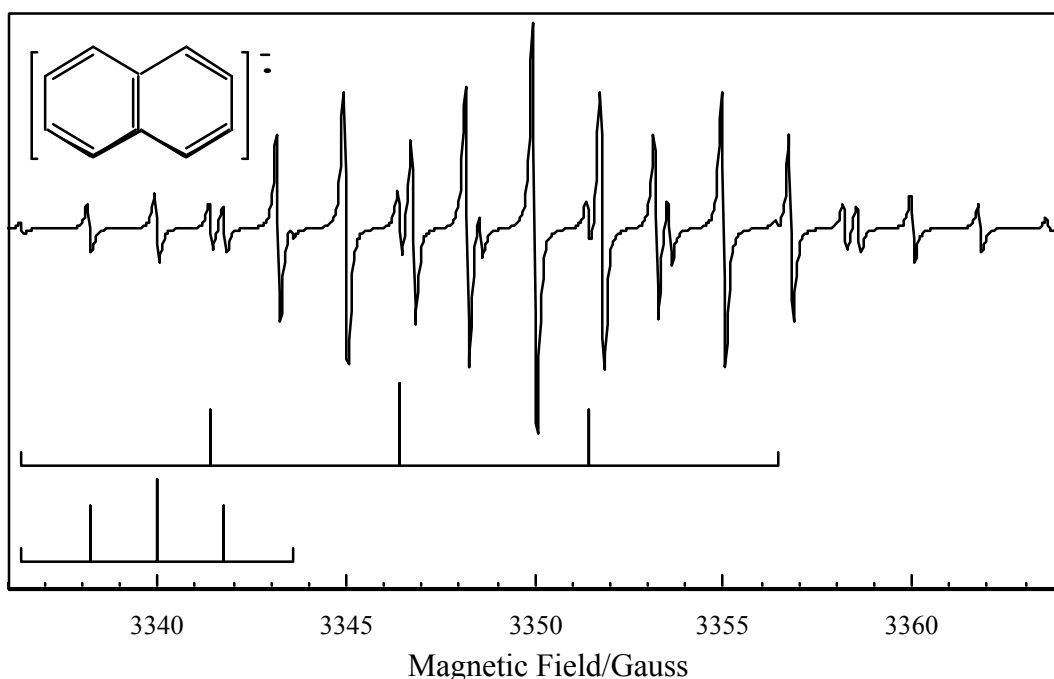
Figure 4.1. ESR spectrum of the naphthalene anion radical (from reference 11); stick spectra at the bottom show the 1:4:6:4:1 quintets corresponding to coupling to the two sets of four equivalent protons.

The naphthalene anion radical spectrum provided a number of surprises. It was a surprise at the time that such an odd-electron species would be stable, but in the absence of air or other oxidants, $[C_{10}H_8]^-$ is stable virtually indefinitely. A second surprise was the appearance of hyperfine coupling to the protons. The odd electron was presumed (correctly) to occupy a p* MO with the protons in the nodal plane. The mechanism of coupling (discussed below) requires "contact" between the unpaired electron and the proton, an apparent impossibility. A third surprise was the ratio of the magnitudes of the two couplings, 5.01 G/1.79 G = 2.80. This ratio is in surprising agreement with the ratio of charge densities predicted for the lowest unoccupied MO (LUMO) at the α and β positions by simple Hückel MO theory, 2.62. This result led to Hückel MO theory being used extensively in the semi-quantitative interpretation of ESR spectra of aromatic radicals.

Just as in NMR, a multiplet pattern gives an important clue to the identity of a radical. For example, the series of radicals derived from the nucleophilic displacement of $Co(CO)_4^-$ from $[(RCCR')Co_2(CO)_6]^-$ by CO, phosphines, or phosphites was identified in large part from the resulting hyperfine patterns [12]. Depending on the nucleophile, spectra were observed which showed coupling to 0, 1, 2, or 3 ^{31}P nuclei, but always to a single ^{59}Co nucleus. The parameters g and a^{Co} were found to depend slightly on the substituents on the acetylene moiety, suggesting that the acetylene was retained in the radical, but otherwise the parameters were nearly constant over the series, suggesting a single family of radicals. The appearance of 0 - 3 phosphorus couplings suggested three additional ligands, either CO or a phosphine or phosphite. Taken together, this information

identified the radicals as $(RCCR')CoL_3$, where $L = CO$, PR_3, or $P(OR)_3$. Figure 4.2a shows the experimental first-derivative spectrum of $(Ph_2C_2)Co(CO)_2P(OMe)_3$, **1**, and Figure 4.2c shows a first-order "stick spectrum" showing the line positions ($\langle g \rangle = 2.061$, $\langle a^{Co} \rangle = 45.2$ G, $\langle a^{P} \rangle = 176.2$ G). Hyperfine coupling to ^{59}Co ($I = 7/2$) and ^{31}P ($I = 1/2$) nuclei results in an octet of doublets. The spectrum is somewhat complicated by the obvious variation in linewidth, but the assignments are quite straightforward.
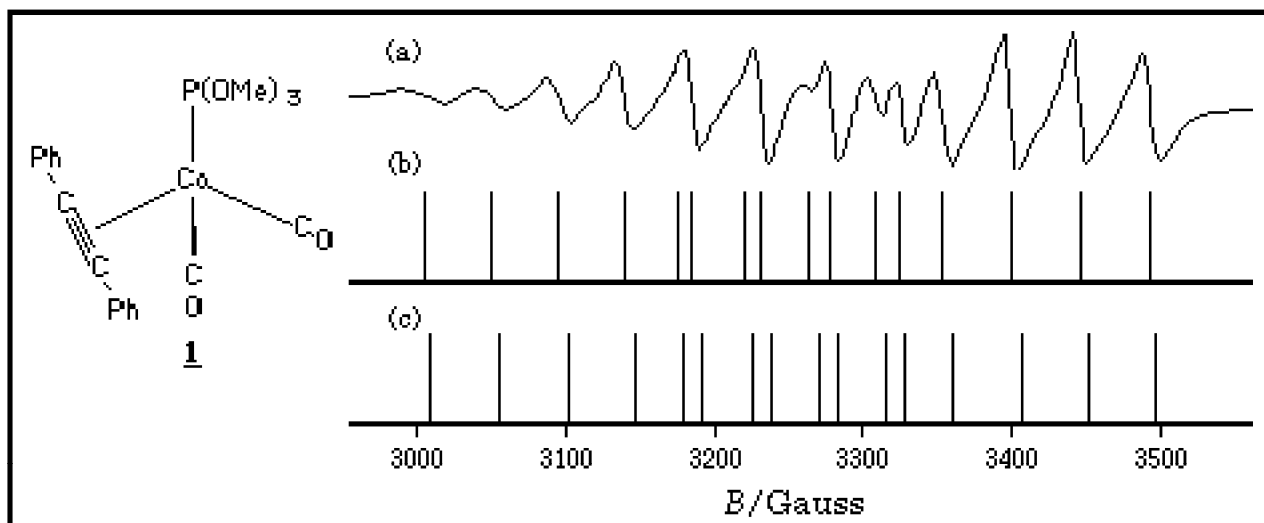

Figure 4.2. (a) Isotropic ESR spectrum of $(Ph_2C_2)Co(CO)_2P(OMe)_3$ (**1**) in THF solution at 260 K (from reference 12); (b) Second-order "stick spectrum"; (c) First-order "stick spectrum".

Nuclei with $I > 1/2$ give less familiar multiplet intensity ratios. Thus, for example, three equivalent ^{59}Co nuclei ($I = 7/2$) give (to first order) 22 lines with intensity ratios 1:3:6:10:15:21:28:36:42:46:48:48:46..., as shown in Figure 4.3a. The experimental spectrum of $[PhCCo_3(CO)_9]^-$, **2** [13], which shows this coupling pattern, is given in Figure 4.3c.

Spin Hamiltonian Parameters from Spectra

Once a hyperfine pattern has been recognized, the line position information can be summarized by the spin Hamiltonian parameters, $\langle g \rangle$ and $\langle a_i \rangle$. These parameters can be extracted from spectra by a linear least-squares fit of experimental line positions to eq (4.3). However, for high-spin nuclei and/or large couplings, one soon finds that the lines are not evenly spaced as predicted by eq (4.3) and second-order corrections must be made. Solving the spin Hamiltonian, eq (4.1), to second order in perturbation theory, eq (4.3) becomes

$$B = B_0 - \sum_i \left\{ \langle a_i \rangle\, m_i + \left[\langle a_i \rangle^2 / 2B\right]\left[I_i(I_i + 1) - m_i^2\right] + \cdots \right\}$$

(4.5)

The magnitude of the second-order corrections is often quite significant. For example, Figure 4.2b shows a stick spectrum computed to second-order for **1**.

Notice that all lines are shifted to low field, relative to the first-order spectrum, but, as expected from eq (4.5), the shift depends on m_{Co}. Failure to account for the second-order terms in an analysis results in a significant error in both the g-value and in the hyperfine coupling constants. For large I_i and $\langle a_i \rangle$, well-resolved spectra may warrant inclusion of third- or higher-order corrections. Since the third-order corrections involve cross terms among coupling constants, in principle they permit determination of the relative signs of the coupling constants. However, in the example of Figure 3.2, the third-order corrections amount to *ca.* 0.1 - 0.2 G, too small to be significant given the resolution of the experimental spectrum. When coupling constants are really large, it is better to fit line positions to the exact energy levels given by the Breit-Rabi equation [10,14].
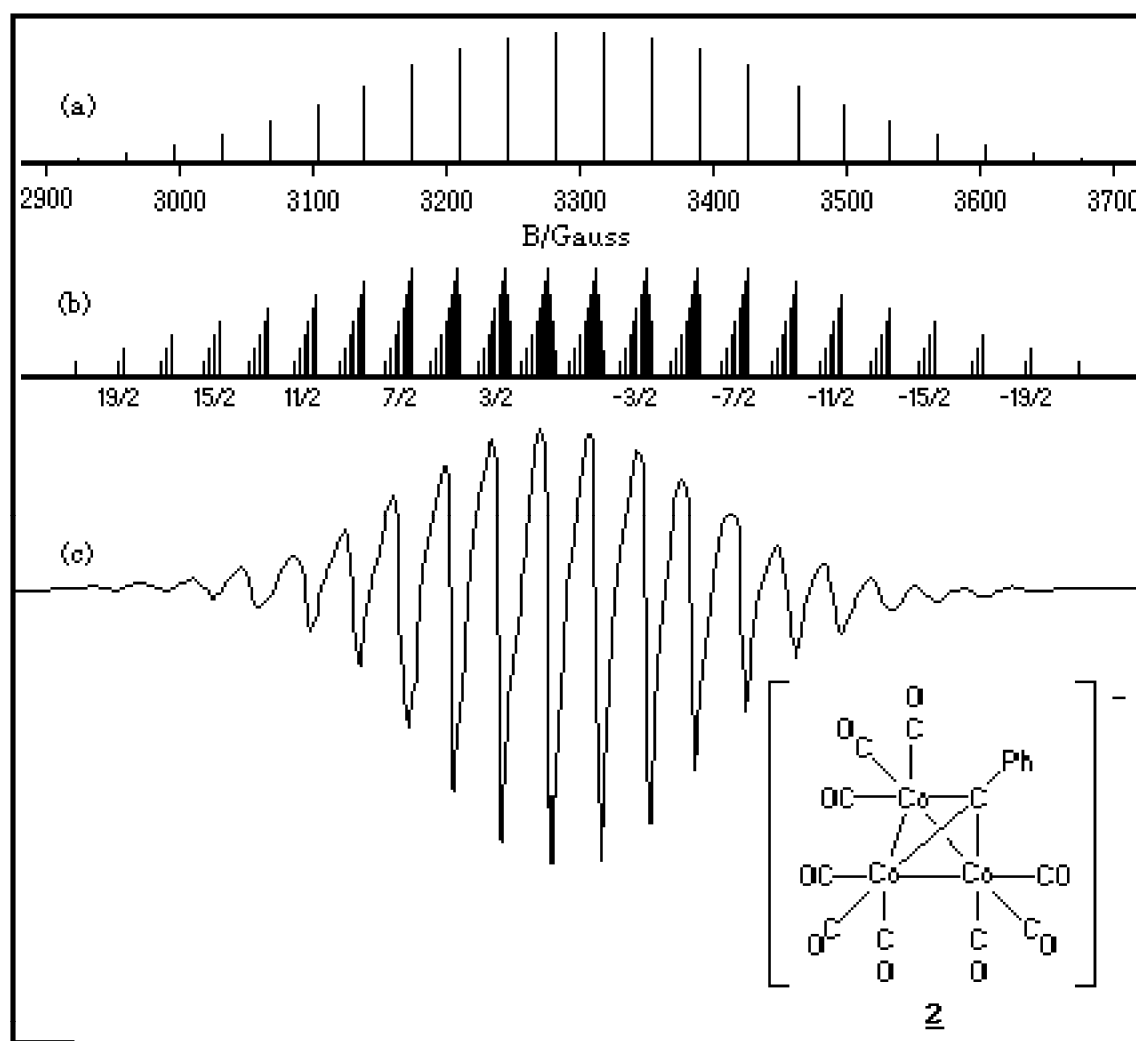

Figure 4.3. "Stick spectrum" showing hyperfine pattern for coupling to three equivalent ^{59}Co nuclei ($I = 7/2$) computed to (a) first-order and (b) second-order in perturbation theory; (c) Isotropic ESR spectrum of [PhCCo$_3$(CO)$_9$]$^-$ in THF solution at 40°C (from reference 13).

Second-order Splittings

Equation (4.5) describes line positions correctly for spectra with hyperfine coupling to two or more nuclei provided that the nuclei are not magnetically equivalent. When two or more nuclei are completely equivalent, *i.e.*, both instantaneously equivalent and equivalent over a time average, then the nuclear spins should be described in terms of the total nuclear spin quantum numbers J and m_J rather than the individual I_i and m_i. In this "coupled representation", the degeneracies of some multiplet lines are lifted when second-order shifts are included. This can lead to extra lines and/or asymmetric line shapes. The effect was first observed in the spectrum of the methyl radical, CH_3 (). The three equivalent protons lead to a nondegenerate nuclear spin state with $J = 3/2$ ($m = \pm 3/2, \pm 1/2$) and a two-fold degenerate state with $J = 1/2$ ($m = \pm 1/2$). Thus six hyperfine lines are observed under conditions of high resolution, as shown in Figure 4.4.
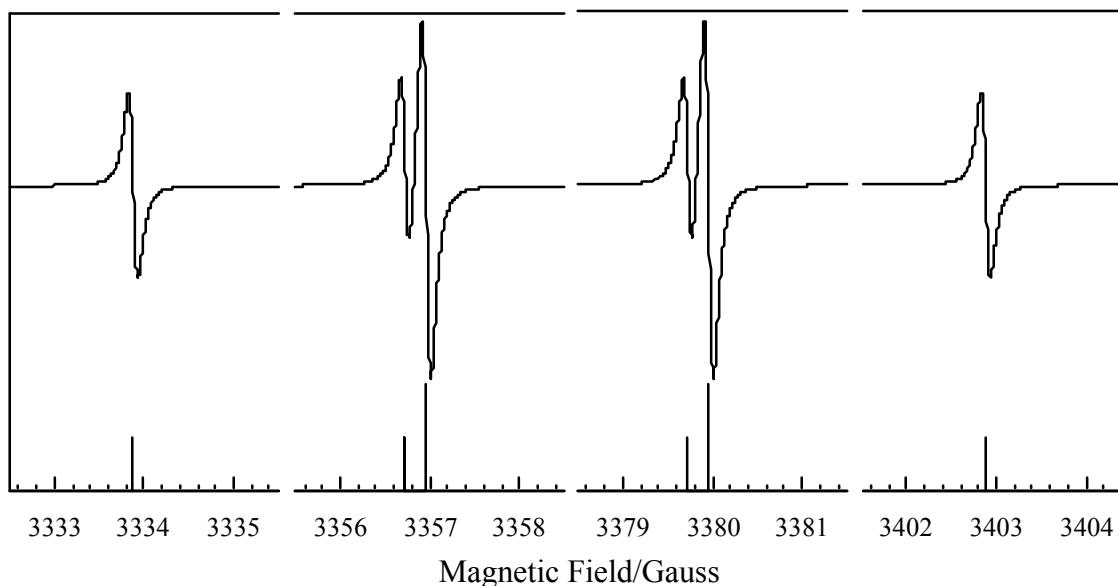

Figure 4.4. ESR spectrum of the methyl radical, CH_3 (from reference 15; note discontinuities in magnetic field axis).

Another example is the spectrum of a tricobaltcarbon radical anion, where the three equivalent spin 7/2 ^{59}Co nuclei should be described in terms of 11 J-states with J ranging from 21/2 to 1/2. The $m_J = 17/2$ feature, for example, has three components with $J = 21/2$, $19/2$, and $17/2$, degeneracies of 1, 2, and 3, and second-order shifts of $97 \langle a \rangle^2/4B$, $55 \langle a \rangle^2/4B$, and $17 \langle a \rangle^2/4B$, respectively. The shifts are too small to be resolved, but they lead to an asymmetric absorption line envelope with apparent broadening on the low-field side, as shown in Figure 4.3a and as is observed in the experimental spectrum of **2**, shown in Figure 4.3c [13].

Interpretation of Isotropic Parameters

When ESR spectra were obtained for the benzene anion radical, $[C_6H_6]^-$, and the methyl radical, CH_3, the proton hyperfine coupling constants were found to be

3.75 G and 23.0 G, respectively. Since each carbon atom of the benzene anion carries an electron spin density of 1/6, the two results suggest that the proton coupling to an electron in a p* orbital is proportional to the spin density on the adjacent carbon atom,

$$\langle a^H \rangle = Q_{CH}{}^H \rho_C{}^p \qquad (4.6)$$

where the parameter $Q_{CH}{}^H$ = 23.0 G, based on CH_3, 22.5 G, based on $[C_6H_6]^-$, or 23.7 G, based on a valence-bond theoretical calculation [16]. An isotropic hyperfine coupling to H can only arise through the so-called Fermi contact interaction of the unpaired electron with the H nucleus, and this is symmetry forbidden for organic p-radicals where the H nuclei lie in the plane of symmetry. The interaction arises in a slightly more complicated way: "spin polarization". As shown in Figure 4.5, the C $2p_z$ orbital has zero probability at the H nucleus, but there is significant overlap of the C $2p_z$ and H 1s orbitals, Suppose the H 1s orbital is part of a σ-bonding MO and the C $2p_z$ part of the singly-occupied p* MO. In the overlap region of these two MO's, there is a tendency for the unpaired spin in the SOMO to polarize the pair of electrons in bonding MO such that the spins in the overlap region are parallel, necessarily leaving an oppositely oriented spin near the H nucleus.

Figure 4.5. Schematic representation of spin polarization of a C-H σ-orbital by electron spin in a p* orbital. Note that the polarization effect is far from complete; only a tiny fraction of the electron density near the H nucleus is excess spin-down.
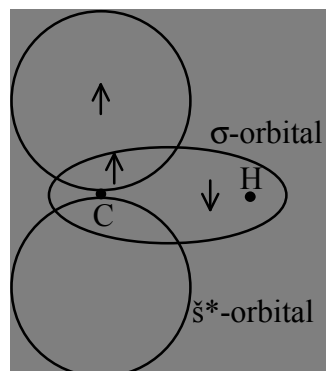
It is sometimes assumed that there is a relation analogous to eq (4.6) for metal or ligand hyperfine couplings in spectra of organometallic radicals. Such an assumption is usually unwarranted. An isotropic hyperfine coupling has three contributions: (i) Fermi contact interaction between the nuclear spin and electron spin density in the valence-shell s-orbital; (ii) Fermi contact interaction between the nuclear spin and spin density in inner-shell s-orbitals arising from spin polarization by unpaired electron density in valence-shell p- or d-orbitals; and (iii) a contribution from spin-orbit coupling. The first contribution is positive (for a positive nuclear magnetic moment), the second is normally negative, and the third may be of either sign. Because direct involvement of hydrogen 1s character in the SOMO of an organic π-radical is symmetry-forbidden and spin-orbit coupling is negligible in carbon-based radicals, proton couplings in such radicals result solely from spin polarization and thus are proportional to the polarizing spin density. All three contributions are usually significant for organometallic radicals. Although there are a few cases where polarization constants, analogous to $Q_{CH}{}^H$, have been estimated [17], they are of use only in a more complete analysis based on the results of a solid state ESR study.

As we will see below, g-matrices are often difficult to interpret reliably. The interpretation of isotropic g-values is even more dangerous. Thus isotropic ESR spectra should be used to characterize a radical by means of the hyperfine coupling pattern, to study its dynamical properties through linewidth effects, or to measure its concentration by integration of the spectrum and comparison with an appropriate standard, but considerable caution should be exercised in interpreting the g-value or nuclear hyperfine coupling constants.

Linewidths in Isotropic Spectra

Incomplete Averaging of Anisotropies. Isotropic ESR spectra usually show variations in linewidth from one hyperfine component to another (see, for example, Figures 4.2a and 4.3). The widths can often be expressed as a power series in the nuclear spin quantum numbers,

$$\text{Width} = \alpha + \sum_i \left(\beta_i m_i + \gamma_i m_i^2 + \cdots \right)$$

$$(4.7)$$

Much of the width arises from incomplete averaging of anisotropies in the g- and hyperfine matrices (see §5), and the parameters of eq (4.7) depend on $\Delta g = g_\parallel - g_\perp$, $\Delta A_i = A_{i,\parallel} - A_{i,\perp}$ and τ_R, the rotational correlation time:

$$\alpha - \alpha_0 \propto (\Delta g)^2 \tau_R \qquad\qquad (4.8a)$$

$$\beta_i \propto \Delta g \, \Delta A_i \tau_R \qquad\qquad (4.8b)$$

$$\gamma_i \propto (\Delta A_i)^2 \tau_R \qquad\qquad (4.8c)$$

Since these terms are proportional to τ_R, they increase with decreasing temperature. There are several linewidth contributions, included in α_0, which do not depend on m_i. These include the spin-rotation interaction which increases with $1/\tau_R$ and thus with increasing temperature. These and other linewidth effects have been studied in some detail and are discussed elsewhere [17-19].

If the g- and hyperfine anisotropies are known from analysis of a solid-state spectrum, the linewidth parameters β_i and γ_i can be used to compute the rotational correlation time, τ_R, a useful measure of freedom of motion. Linewidths in ESR spectra of nitroxide spin labels, for example, have been used to probe the motional freedom of biological macromolecules [20]. Since τ_R is related to the molecular hydrodynamic volume, V_h, and the solution viscosity, η, by

$$\tau_R = \eta V_h / k_B T \qquad\qquad (4.9)$$

ESR linewidths can provide a measure of the effective size of a paramagnetic molecule or ion, useful information when there is a suspicion that a radical has polymerized. Thus, for example, vanadium(IV) shows an eight-line ESR spectrum in basic aqueous solution, suggesting a monomeric unit, $[VO(OH)_3(H_2O)_2]^-$ [21], although previous work on the system had indicated polymers such as $V_3O_7^{2-}$ or $V_4O_9^{2-}$. Comparison of values of τ_R from the basic solution linewidths with those obtained from spectra of acidic solutions containing $VO(H_2O)_5^{2+}$ showed that the hydrodynamic volume of the aquo cation is actually about twice that of the basic

solution species, effectively ruling out the presence of ESR-active polymers in solution [22].

Rates of Fluxionality from Linewidths. ESR linewidths are also sensitive to processes which modulate the *g*-value or hyperfine coupling constants or limit the lifetime of the electron spin state. The effects are closely analogous to those observed in NMR spectra of dynamical systems. However, since ESR linewidths are typically on the order of 0.1-10 G (0.3-30 MHz), rate processes which give observable increases in linewidths must be fast. Bimolecular processes which contribute to ESR linewidths have mostly been nearly diffusion-controlled, *e.g.*, intermolecular electron exchange between naphthalene and its anion radical [23] and reversible axial ligation of square planar copper(II) complexes [24].

The effect of rate processes on linewidths can be understood quantitatively in terms of the modified Bloch equations ([25], see also Appendix 3), or, more accurately, in terms of density matrix [26] or relaxation matrix [18,27] formalisms. If a rate process modulates a line position through an amplitude ΔB ($\Delta\omega$ in angular frequency units) by fluctuating between two states, each with lifetime τ, a single line is observed with an excess width proportional to $(\Delta\omega)^2\tau$ when $\tau^{-1} \gg \Delta\omega$—the fast exchange limit. As the lifetime increases, the line broadens to indetectability and then re-emerges as two broad lines. These shift apart and sharpen until, in the slow exchange limit ($\tau^{-1} \ll \Delta\omega$), two lines are observed with widths proportional to τ^{-1}.

ESR spectra of the radical anion of *bis*-(diphenylphosphino)maleic anhydride, (**3**) [28], are shown in Figure 4.6. These spectra provide a good example of dynamical linewidth effects. This radical shows a 1:2:1 triplet spectrum at higher temperatures, (a^P) = 3.52 G at 240 K, but the phosphorus coupling is strongly temperature dependent and extra lines appear at 200 K and below indicating a dynamical equilibrium between two isomeric forms of the radical, one having two equivalent P nuclei (1:2:1 triplet spectrum), the other two nonequivalent P nuclei (doublet of doublets spectrum). The lines broaden with increasing temperature and coalesce at about 220 K.

These data can be understood in terms of two rotational isomers of BMA$^-$:
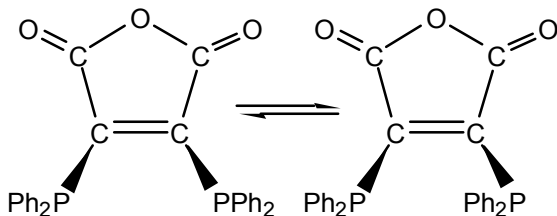
Detailed analysis led to the thermodynamic and kinetic parameters: $\Delta H° = 0.8 \pm 0.2$ kJ mol^{-1}, $\Delta S° = -4 \pm 1$ J mol^{-1}K^{-1} (K_{160} = 3.0); $\Delta H^\dagger = 18.2 \pm 0.4$ kJ mol^{-1}, $\Delta S^\dagger = -30 \pm 2$ J mol^{-1}K^{-1} ($k_{200} = 1.9 \infty 10^6$).

Figure 4.6. Isotropic ESR spectra of **3** in THF solution at various temperatures.

Casagrande, et al. [12], used linewidth effects to study the rate of fluxionality in (Ph$_2$C$_2$)Co(CO)[P(OMe)$_3$]$_2$, **4**. The experimental spectrum, shown in Figure 4.7a, can be described as a 1:2:1 triplet of octets; the spectrum is complicated by a large linewidth dependence on m_{Co}, but as demonstrated in Figures 4.7b and 4.7c, the central lines of the triplets are much broader than the outer lines. This radical has a distorted tetrahedral structure with the semi-occupied molecular orbital (SOMO) largely cobalt 3d$_{z^2}$ in character [29]. Thus the ligand sites can be described as axial or equatorial relative to the unique *z*-axis. Several isomers are possible, but the ^{31}P couplings distinguish between the isomer with an axial phosphite (ax,eq) and those with either CO or the acetylene axial and both phosphites equatorial (eq,eq). The rate of interconversion between eq,eq and ax,eq isomers was estimated from the relative widths of the $m_P = \pm 1$ and 0 lines, given the isotropic coupling constants for the various ^{31}P nuclei (which were determined from the frozen solution spectrum [29]). The average rate was found to be approximately $2 \infty 10^{10}$ s^{-1} ($E_a = 17$ kJ mol^{-1}) at 298 K.

Figure 3.7. ESR spectrum of $(Ph_2C_2)Co(CO)[P(OMe)_3]_2$. (a) Experimental spectrum of THF solution at 290 K; (b and c) Computer-simulated spectra including (b) the m_{Co} and m_P linewidth dependence, and (c) the m_{Co} linewidth dependence only.

5. Anisotropic ESR Spectra

The anisotropies which lead to line broadening in isotropic ESR spectra influence solid-state spectra more directly. Accordingly a more complex spin Hamiltonian is required to interpret such spectra

$$\hat{H}_s = \mu_B \vec{B} \cdot g \cdot \vec{S} + \sum_i \vec{I}_i A_i \vec{S}$$

(5.1)

In eq (5.1), g and A_i are $3\infty3$ matrices representing the anisotropic Zeeman and nuclear hyperfine interactions. In general, a coordinate system can be found—the g-matrix principal axes—in which g is diagonal. If g and A_i are diagonal in the same coordinate system, we say that their principal axes are coincident.

In species with two or more unpaired electrons, a fine structure term must be added to the spin Hamiltonian to represent electron spin-spin interactions. We will confine our attention here to radicals with one unpaired electron ($S = 1/2$) but will address the $S > 1/2$ problem in Section 6.

Nuclear quadrupole interactions introduce line shifts and forbidden transitions in spectra of radicals with nuclei having $I > 1/2$. In practice, quadrupolar effects are observable only in very well-resolved spectra or in spectra of radicals with nuclei having small magnetic moments and large quadrupole moments. The most extreme case of a small magnetic moment to quadrupole moment ratio is that of ^{191}Ir/^{193}Ir, and spectra of $[Ir(CN)_6]^{3-}$ [30], $[Ir(CN)_5Cl]^{4-}$ and $[Ir(CN)_4Cl_2]^{4-}$ [31], and $[Ir_2(CO)_2(PPh_3)_2(\mu\text{-RNNNR})_2]^+$, R = p-tolyl [32], show easily recognizable quadrupolar effects. Other nuclei for which quadrupolar effects might be expected include ^{151}Eu/^{153}Eu, ^{155}Gd/^{157}Gd, ^{175}Lu, ^{181}Ta, ^{189}Os, and ^{197}Au. When quadrupolar effects are important, it is usually necessary to take account of the nuclear Zeeman interaction as well. The nuclear quadrupole and nuclear Zeeman interactions add two more terms to the spin Hamiltonian. Since these terms considerably complicate an already complex situation, we will confine our attention here to nuclei for which quadrupolar effects can be neglected.

When a radical is oriented such that the magnetic field direction is located by the polar and azimuthal angles, θ and ϕ, relative to the g-matrix principal axes, the resonant field is given, to first order in perturbation theory, by [33]

$$B = B_0 - \sum_i \frac{A_i m_i}{g\mu_B}$$

(5.2)

where
$$B_0 = \frac{h\,\boldsymbol{n}}{g\mu_B}$$

(5.3)

$$g^2 = g_x{}^2 \sin^2\theta \cos^2\phi + g_y{}^2 \sin^2\theta \sin^2\phi + g_z{}^2\cos^2\theta$$

(5.4)

$$A_i{}^2 = A_{iz}{}^2 S_{ix}{}^2 + A_{iy}{}^2 S_{iy}{}^2 + A_{iz}{}^2 S_{iz}{}^2$$

(5.5)

$$S_{ik} = [g_x \sin\theta \cos\phi\, l_{ixk} + g_y \sin\theta \cos\phi\, l_{iyk} + g_z \cos\theta\, l_{izk}]/g$$

(5.6)

and the l_{ijk} are direction cosines indicating the orientation of the kth principal axis of the ith hyperfine matrix relative to the jth g-matrix principal axis. When the matrix principal axes are coincident, only one of the l_{ijk} of eq (4.6) will be nonzero. When the hyperfine matrix components are large, second-order terms [33] must be added to eq (5.2); these result in down-field shifts, proportional to $m_i{}^2$.

Solid-State ESR Spectra

So long as they are dilute (to avoid line broadening from intermolecular spin exchange), radicals can be studied in the solid state as solutes in single crystals,

powders, glasses or frozen solutions. Radicals can be produced *in situ* by UV- or γ-irradiation of a suitable precursor in a crystalline or glassy matrix. While many organometallic radicals have been studied in this way [34], it is often easier to obtain solid state ESR spectra by freezing the liquid solution in which the radical is formed. A variety of techniques then can be used to generate radicals, *e.g.*, chemical reactions, electrochemical reduction or oxidation, or photochemical methods. Furthermore, the radical is studied under conditions more closely approximating those in which its reaction chemistry is known.

Spectra of Dilute Single Crystals. Spectra of radicals in a dilute single crystal are obtained for a variety of orientations, usually with the field perpendicular to one of the crystal axes. Spectra usually can be analyzed as if they were isotropic to obtain an effective *g*-value and hyperfine coupling constants. Since the *g*- and hyperfine matrix principal axes are not necessarily the same as the crystal axes, the matrices, written in the crystal axis system usually will have off-diagonal elements. Thus, for example, if spectra are obtained for a variety of orientations in the crystal *xy*-plane, the effective *g*-value is

$$g_\phi^2 = (g_{xx} \cos \phi + g_{yx} \sin \phi)^2 + (g_{xy} \cos \phi + g_{yy} \sin \phi)^2 + (g_{xz} \cos \phi + g_{yz} \sin \phi)^2 \quad (5.7)$$

or
$$g_\phi^2 = K_1 + K_2 \cos 2\phi + K_3 \sin 2\phi \quad (5.8)$$

where
$$K_1 = (g_{xx}^2 + g_{yy}^2 + g_{xz}^2 + g_{yz}^2 + 2\,g_{xy}^2)/2 \quad (5.9a)$$

$$K_2 = (g_{xx}^2 - g_{yy}^2 + g_{xz}^2 - g_{yz}^2)/2 \quad (5.9b)$$

$$K_3 = g_{xy}(g_{xx} + g_{yy}) + g_{xz}g_{yz} \quad (5.9c)$$

A sinusoidal plot of g_ϕ^2 vs ϕ can be analyzed to determine K_1, K_2, and K_3. Exploration of another crystal plane gives another set of K's which depend on other combinations of the g_{ij}; eventually enough data are obtained to determine the six independent g_{ij} (**g** is a symmetric matrix so that $g_{ij} = g_{ji}$). The **g²**-matrix then is diagonalized to obtain the principal values and the transformation matrix, elements of which are the direction cosines of the *g*-matrix principal axes relative to the crystal axes. An analogous treatment of the effective hyperfine coupling constants leads to the principal values of the **A²**-matrix and the orientation of its principal axes in the crystal coordinate system.

Analysis of Powder Spectra. Since ESR spectra are normally recorded as the first derivative of absorption *vs*. field, observable features in the spectrum of a powder correspond to molecular orientations for which the derivative is large in magnitude or changes in sign. For any spin Hamiltonian, there will be minimum and maximum resonant fields at which the absorption changes rapidly from zero, leading to a large value of the derivative and features which resemble positive-going and negative-going absorption lines. Peaks in the absorption envelope correspond to derivative sign changes and lead to features resembling isotropic derivative lines. The interpretation of a powder spectrum thus depends on the connection of the positions of these features to the *g*- and hyperfine matrix components.

Early treatments of powder patterns attempted to deal with the spatial distribution of resonant fields by analytical mathematics [35]. This approach led to some valuable insights but the algebra is much too complex when nonaxial hyperfine matrices are involved. Consider the simplest case: a single resonance line without hyperfine structure. The resonant field is given by eq (5.3). Features in the first derivative spectrum correspond to discontinuities or turning points in the absorption spectrum which arise when $\partial B/\partial\theta$ or $\partial B/\partial\phi$ are zero,

$$\frac{\partial B}{\partial \theta} = \frac{h\nu}{\mu_B} \frac{g_z^2 - g_\perp^2}{g^3} \sin\theta\cos\theta = 0 \tag{5.10a}$$

$$\frac{\partial B}{\partial \phi} = \frac{h\nu}{\mu_B} \frac{g_x^2 - g_y^2}{g^3} \sin^2\theta \sin\phi\cos\phi = 0$$

or $\tag{5.10b}$

These equations have three solutions: (i) $\theta = 0$; (ii) $\theta = 90°$, $\phi = 0$; and (iii) $\theta = \phi = 90°$. Since θ and ϕ are in the g-matrix axis system, observable features are expected for those fields corresponding to orientations along the principal axes of the g-matrix. This being the case, the principal values of the g-matrix are obtained from a straightforward application of eq (5.3).

Powder spectra with hyperfine structure often can be interpreted similarly with spectral features identified with orientation of the magnetic field along one of the g- and hyperfine matrix principal axes. However, this simple situation often breaks down. Using a first-order theory and one hyperfine coupling, Ovchinnikov and Konstantinov [36] have shown that eqs (5.10) may have up to six solutions corresponding to observable spectral features. Three of these correspond to orientation of B along principal axes, but the "extra lines" correspond to less obvious orientations. Even more extra lines may creep in when the spin Hamiltonian is treated to second order or when there is more than one hyperfine coupling. The problem is illustrated by the resonant field $vs.$ cos θ and ϕ surface shown in Figure 5.1, corresponding to the $m_{Cu} = -3/2$ "line" in the spectrum of Cu(acac)$_2$ ($g = 2.0527$, 2.0570, 2.2514; $A^{Cu} = 27.0$, 19.5, 193.4 ∞ 10^{-4} cm^{-1}) [36]. The minimum resonant field, B = 3290.7 G, corresponds to B along the z-axis (cos $\theta = \pm 1$). With B along the x-axis (cos $\theta = 0$, $\phi = 0°$), the surface shows a saddle point at 3344.3 G, and with B along the y-axis (cos $\theta = 0$, $\phi = 90°$), there is a local minimum at 3325.5 G. In addition, another saddle point occurs in the yz-plane at $B = 3371.2$ G (cos $\theta = \pm 0.482$, $\phi = 90°$); the only maximum is in the xz-plane at $B = 3379.0$ G (cos $\theta = \pm 0.459$, , $\phi = 0°$). Thus five features are expected and indeed are shown in the computer-simulated spectrum of Cu(acac)$_2$ shown in Figure 5.2. The two high-field features correspond to off-axis field orientations and thus are "extra lines". The situation is more complex when the g- and hyperfine matrix principal axes are noncoincident (see below); in this case, none of the features need correspond to orientation of B along a principal axis direction.

Figure 5.1. Resonant field as a function of $\cos\theta$ and ϕ for the m_{Cu} = -3/2 "line" of the frozen solution spectrum of $Cu(acac)_2$; ESR parameters from reference 36.
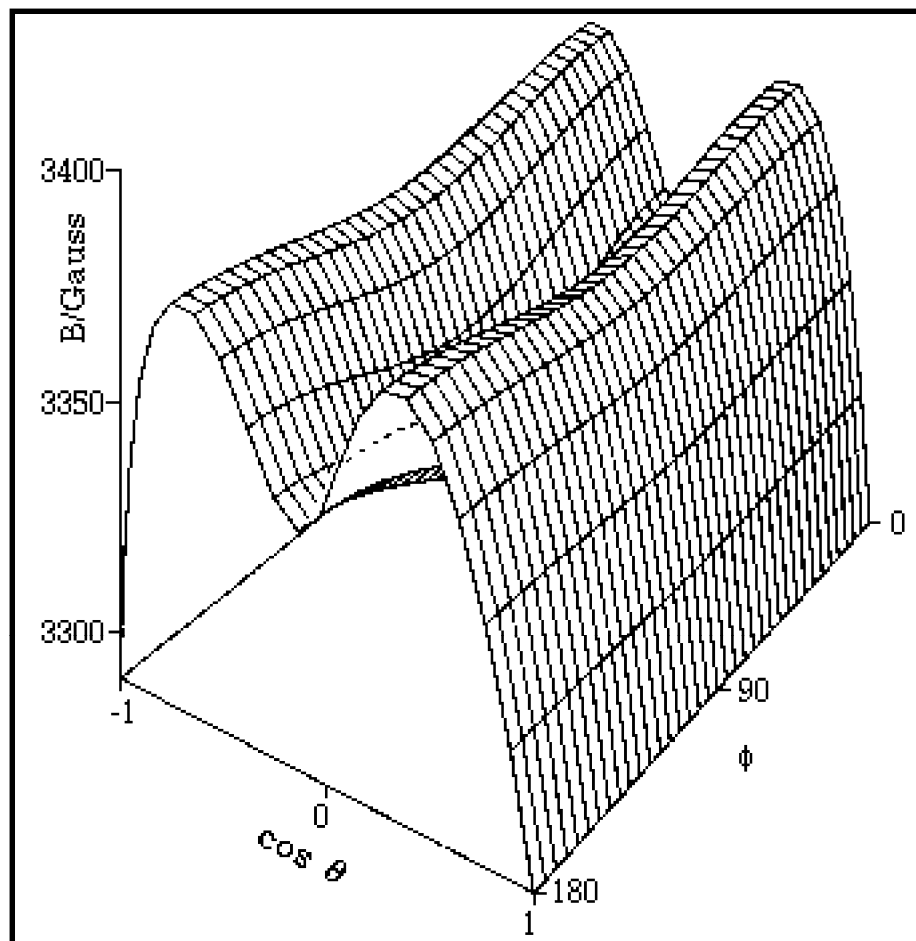
Since the analytical approach is so complicated, powder patterns have usually been analyzed by comparing the experimental spectrum with a spectrum, computer-simulated using estimates of the *g*- and hyperfine matrix components. Parameters are then adjusted and another simulation computed until the fit is satisfactory (or the experimentalist loses patience with the problem). The most straightforward computer simulation method [37] involves computation of the resonant magnetic field using eq (5.2) for *ca.* 10^5 values of $\cos\theta$ and ϕ for each set of nuclear spin quantum numbers. The field is then divided into equal increments and the number of times the resonant field falls between B_i and B_{i+1} is plotted *vs. B* to give an approximation to the unbroadened absorption spectrum. The absorption spectrum is then broadened by numerical convolution with a line shape function and differentiated to give the desired simulation. Although the "cut and try" approach to spectrum analysis works reasonably well when there are small numbers of parameters, analysis of a complex spectrum is exceedingly tedious.

DeGray and Rieger [38] have developed a computer algorithm to locate powder pattern features in spectra, given estimates of the spin Hamiltonian parameters. The method employs a search of the resonant field surface in $\cos\theta$, ϕ space for maxima, minima, and saddle points. Since the search procedure requires computation of *B* for ~100 orientation, the method is much faster than a complete
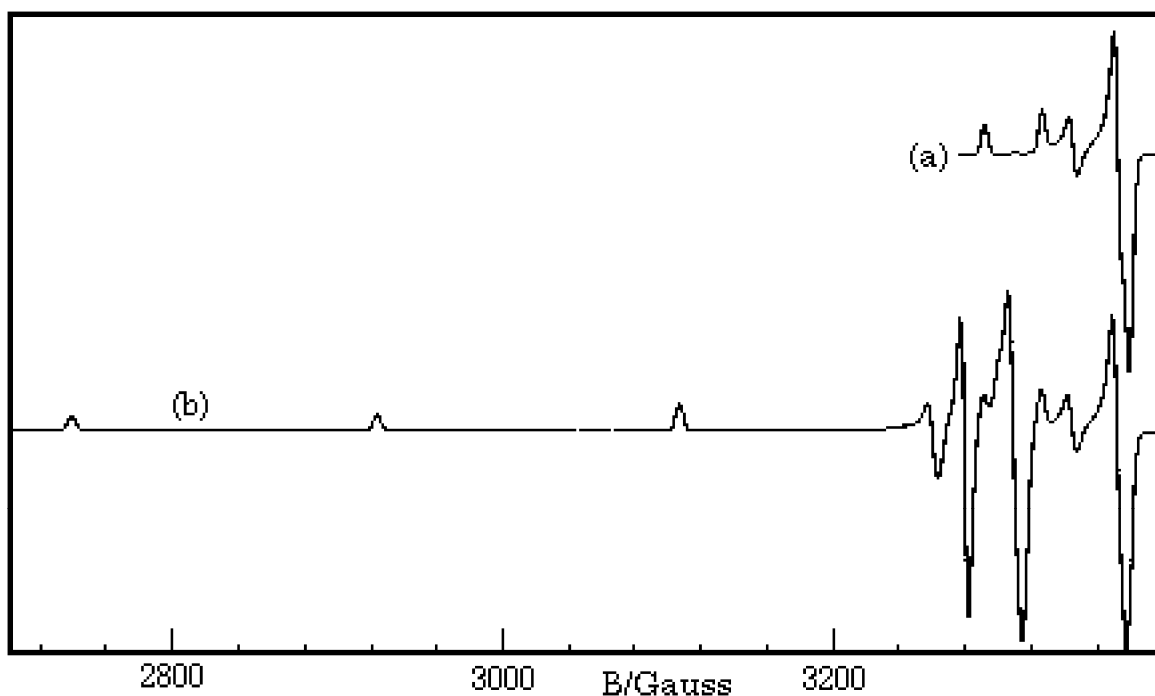
Figure 5.2. Computer-simulated first-derivative ESR powder spectrum of Cu(acac)$_2$. (a) Features corresponding to $m_{Cu} = -3/2$; (b) Complete spectrum.

simulation. The predicted locations of spectral features then are compared with the experimental values and the parameters refined using a nonlinear least-squares method. Using this method, relatively complex powder patterns can be analyzed, provided that the spectrum is sufficiently well resolved that enough features can be located and identified to determine the parameters. Even with least-squares fitting, however, comparison of the experimental spectrum with a computer simulation is required to check the assignments of spectral features.

Interpretation of the g-Matrix

The *g*-value of a free electron is a scalar, $g_e = 2.00232$. In a radical species, *g* becomes a matrix because of the admixture of orbital angular momentum into S through spin-orbit coupling. The components of the *g*-matrix thus differ from g_e to the extent that p-, d- or f-orbital character has been incorporated and differ from one another, depending on which p- , d- or f-orbitals are involved.

In general, the components of the *g*-matrix are given by

$$g_{ij} = g_e \delta_{ij} + 2 \sum_k \sum_{m \circ 0} \frac{\zeta_k \langle m | l_{ki} | 0 \rangle \langle 0 | l_{kj} | m \rangle}{E_0 - E_m}$$

(5.11)

where the indices *i* and *j* refer to molecular coordinate axes (*x, y, z*), *k* sums over atoms with unpaired electron density, and *m* sums over filled and empty molecular orbitals with energy E_m (E_0 is the energy of the SOMO); ζ_k is the spin-orbit coupling constant for atom *k*, and l_{ki} is the *i*-component orbital angular momentum operator for atom *k*. The integrals $\langle m | l_{ki} | n \rangle$ are easily computed if the MO's are

written as linear combination of real p or d atomic orbitals. The results of operation by l_i on these functions is shown in Table 5.1. Thus, for example, $\langle z|l_x|y\rangle = i$ and $\langle z|l_y|xz\rangle = -\sqrt{3}\,i$.

Notice that d_{z^2} is unique among the d-orbitals in that $\boldsymbol{l_z}$ does not couple it to any other orbital. Thus if the major metal contribution to the SOMO is d_{z^2}, g_z will be close to the free electron value. Accordingly, when one g-matrix component is found close to the free electron value, it is often taken as evidence for a d_{z^2}-based SOMO; such reasoning should be applied with caution, however, since cancellation of negative and positive terms in eq (5.11) could have the same effect.

Spin-orbit coupling to empty MO's ($E_0 - E_m < 0$) gives a negative contribution to g_{ij} whereas coupling to filled MO's has the opposite effect. Thus ESR spectra of d^1 vanadium(IV) complexes generally have g-values less than g_e (admixture of empty MO's) whereas d^9 copper(II) complexes have g-values greater than g_e (admixture of filled MO's).

Since the g-matrix has only three principal values and there are almost always many potentially interacting molecular orbitals, there is rarely sufficient information to interpret a g-matrix with complete confidence. When a well resolved and reliably assigned optical spectrum is available, the energy differences, $E_0 - E_m$, are known and can be used in eq (5.11). Extended Hückel MO calculations can be useful (but don't trust EHMO energies!), but one is most commonly reduced to arguments designed to show that the observed g-matrix is consistent with the interpretation placed on the hyperfine matrix.

Table 5.1. Angular momentum operations on the real p and d orbitals.

	l_x	l_y	l_z
$\lvert x\rangle$	0	$-i\lvert z\rangle$	$i\lvert y\rangle$
$\lvert y\rangle$	$i\lvert z\rangle$	0	$-i\lvert x\rangle$
$\lvert z\rangle$	$-i\lvert y\rangle$	$i\lvert x\rangle$	0
$\lvert x^2\text{-}y^2\rangle$	$-i\lvert yz\rangle$	$-i\lvert xz\rangle$	$2i\lvert xy\rangle$
$\lvert xy\rangle$	$i\lvert xz\rangle$	$-i\lvert yz\rangle$	$-2i\lvert x^2\text{-}y^2\rangle$
$\lvert yz\rangle$	$i\lvert x^2\text{-}y^2\rangle + \sqrt{3}\,i\lvert z^2\rangle$	$i\lvert xy\rangle$	$-i\lvert xz\rangle$
$\lvert xz\rangle$	$-i\lvert xy\rangle$	$i\lvert x^2\text{-}y^2\rangle - \sqrt{3}\,i\lvert z^2\rangle$	$i\lvert yz\rangle$
$\lvert z^2\rangle$	$-\sqrt{3}\,i\lvert yz\rangle$	$\sqrt{3}\,i\lvert xz\rangle$	0

Interpretation of the Hyperfine Matrix

Electron-nuclear hyperfine coupling arises mainly through two mechanisms: (i) The Fermi contact interaction between the nuclear spin and s-electron spin density; this contribution is isotropic and has been discussed above. (ii) The electron spin-nuclear spin magnetic dipolar interaction; this contribution is almost entirely

anisotropic, *i.e.*, neglecting spin-orbit coupling, the average dipolar contribution to the hyperfine coupling is zero.

The general form of the dipolar contribution to the hyperfine term of the Hamiltonian is

$$\hat{H}_{\text{dipolar}} = g_e g_N \mu_B \mu_N \left\langle \psi_{\text{SOMO}} \left| \frac{\vec{S} \cdot \vec{I}}{r^3} - \frac{3(\vec{S} \cdot \vec{r})(\vec{I} \cdot \vec{r})}{r^5} \right| \psi_{\text{SOMO}} \right\rangle$$

(5.12)

where g_e and g_N are the electron and nuclear g-values, μ_B and μ_N are the Bohr and nuclear magnetons, and the matrix element is evaluated by integration over the spatial coordinates, leaving the spins as operators. Equation (5.12) can then be written

$$\hat{H}_{\text{dipolar}} = \vec{I} \cdot \mathbf{A}_{\text{d}} \cdot \vec{S}$$

(5.13)

where $\mathbf{A}_{\text{d}}$ is the dipolar contribution to the hyperfine matrix,

$$\mathbf{A} = \bullet A \circledR \mathbf{E} + \mathbf{A}_{\text{d}}$$

(5.14)

($\mathbf{E}$ is the unit matrix). In evaluating the matrix element of eq (5.12), the integration over the angular variables is quite straightforward. The integral over r, however, requires a good atomic orbital wavefunction. Ordinarily, the integral is combined with the constants as a parameter

$$P = g_e g_N \mu_B \mu_N \left\langle r^{-3} \right\rangle$$

(5.15)

P has been computed using Hartree-Fock atomic orbital wavefunctions and can be found in several published tabulations [39-42]. Because of the $\left\langle r^{-3} \right\rangle$ dependence of P, dipolar coupling of a nuclear spin with electron spin density on another atom is usually negligible.

If an atom contributes p_x, p_y, and p_z atomic orbitals to the SOMO

$$c_x |x\rangle + c_y |y\rangle + c_z |z\rangle$$

(5.16)

the total p-orbital spin density is (in the Hückel approximation, i.e., neglecting overlap):

$$\rho^p = c_x{}^2 + c_y{}^2 + c_z{}^2$$

(5.17)

and the dipolar contribution to the hyperfine matrix can be written

$$(\mathbf{A}_{\text{d}})_{ij} = (2/5) P l_{ij}$$

(5.18)

where the l_{ij} are

$$l_{xx} = 2c_x{}^2 - c_y{}^2 - c_z{}^2$$

(5.19a)

$$l_{yy} = -c_x{}^2 + 2c_y{}^2 - c_z{}^2$$

(5.19b)

$$l_{zz} = -c_x{}^2 - c_y{}^2 + 2c_z{}^2$$

(5.19c)

$$l_{ij} = -3c_i c_j \quad (i \ ? \ j)$$

(5.19d)

The dipolar hyperfine matrix for p-orbitals can always be written

$$\mathbf{A_d} = (2/5)P\rho^{\mathrm{p}} \begin{pmatrix} 2 & 0 & 0 \\ 0 & -1 & 0 \\ 0 & 0 & -1 \end{pmatrix}$$

(5.20)

The p-orbital axis corresponds to the positive principal value of the matrix. When the p-orbitals are written as hybrids, the orbital shape is unchanged, but the principal axes of the hyperfine matrix, which reflect the spatial orientation of the hybrid p-orbital, differ from those in which the SOMO was formulated. Thus, for example, a p-hybrid with $c_x = c_z$ ($c_y = 0$) corresponds to a p-orbital with the major axis in the xz-plane and halfway between the x- and z-axes (Euler angle $\beta = 45°$).

Similarly, if an atom contributes d atomic orbitals to the SOMO,

$$c_{z^2}\left|z^2\right\rangle + c_{yz}\left|yz\right\rangle + c_{xz}\left|xz\right\rangle + c_{x^2-y^2}\left|x^2-y^2\right\rangle + c_{xy}\left|xy\right\rangle$$

(5.21)

the total d-orbital spin density is (in the Hückel approximation):

$$\rho^{\mathrm{d}} = \left(c_{z^2}\right)^2 + \left(c_{yz}\right)^2 + \left(c_{xz}\right)^2 + \left(c_{x^2-y^2}\right)^2 + \left(c_{xy}\right)^2$$

(5.22)

and the dipolar contribution to the hyperfine matrix is [43]

$$(\mathbf{A_d})_{ij} = (2/7)Pl_{ij}$$

(5.23)

where P is given by eq (5.15) and the l_{ij} are:

$$l_{xx} = -\left(c_{z^2}\right)^2 - 2\left(c_{yz}\right)^2 + \left(c_{xz}\right)^2 + \left(c_{x^2-y^2}\right)^2 + \left(c_{xy}\right)^2 - 2\sqrt{3}\left(c_{z^2}\right)\left(c_{x^2-y^2}\right)$$

(5.24a)

$$l_{yy} = -\left(c_{z^2}\right)^2 + \left(c_{yz}\right)^2 - 2\left(c_{xz}\right)^2 + \left(c_{x^2-y^2}\right)^2 + \left(c_{xy}\right)^2 + 2\sqrt{3}\left(c_{z^2}\right)\left(c_{x^2-y^2}\right)$$

(5.24b)

$$l_{zz} = 2(c_{z^2})^2 + (c_{yz})^2 + (c_{xz})^2 - 2(c_{x^2-y^2})^2 - 2(c_{xy})^2$$

(5.24c)

$$l_{xy} = -2\sqrt{3}\left(c_{z^2}\right)\left(c_{xy}\right) + 3\left(c_{yz}\right)\left(c_{xz}\right)$$

(5.24d)

$$l_{yz} = \sqrt{3}\left(c_{z^2}\right)\left(c_{yz}\right) + 3\left(c_{xz}\right)\left(c_{xy}\right) - 3\left(c_{yz}\right)\left(c_{x^2-y^2}\right)$$

(5.24e)

$$l_{xz} = \sqrt{3}\left(c_{z^2}\right)\left(c_{xz}\right) + 3\left(c_{yz}\right)\left(c_{xy}\right) + 3\left(c_{xz}\right)\left(c_{x^2-y^2}\right)$$

(5.24f)

The dipolar contribution to the hyperfine matrix for a pure d-orbital is

$$\mathbf{A_d} = (\pm 2/7)P\rho^{\mathrm{d}} \begin{pmatrix} 2 & 0 & 0 \\ 0 & -1 & 0 \\ 0 & 0 & -1 \end{pmatrix}$$

(5.25)

where the positive sign applies for d_{z^2} and the lower sign to the other four orbitals. Hybrid combinations of d_{yz}, d_{xz}, and d_{xy} or $d_{x^2-y^2}$ and d_{xy} give a d-orbital of the

same shape and the same dipolar matrix, though the principal axes in general are different from the axes in which the SOMO was formulated. Other hybrid orbitals are generally of different shape, reflected by different principal values of the dipolar matrix, usually with different principal axes.

Spin-orbit coupling perturbs these results, adding terms to the diagonal matrix components on the order of $P(g_i - g_e)$. These can be neglected only when the g-matrix anisotropy is small. Calculation of the spin-orbit coupling corrections is fairly straightforward for mononuclear complexes where the SOMO is composed mainly of d-orbitals from a single metal [6,44,45]. In radicals with two or more transition metals, the spin-orbit coupling calculation is seriously nontrivial. A major part of the problem is that the solution must be gauge-invariant, that is, it must not depend on the choice of coordinate system. This problem was addressed in the context of spin-orbit coupling corrections to the g-matrix [46], with eq (5.11) as the result, but it has received only cursory examination with regard to spin-orbit contributions to hyperfine matrices [47]. Fortunately, polynuclear radicals containing first-row transition metals generally have g-matrix components sufficiently close to g_e that the problem can be ignored. For organometallic radicals with second- and third-row transition metals, the problem is urgent; it is to be hoped that some theoretician will deem the problem worthy of attention.

The AO composition of the SOMO can often be deduced from the dipolar hyperfine matrix, particularly when the radical has enough symmetry to restrict possible hybridization. Thus an axial hyperfine matrix can usually be interpreted in terms of coupling to a single p- or d-orbital. A departure from axial symmetry may be due to spin-orbit coupling effects, if (for example) $A_\parallel = A_z$ and $A_x - A_y \approx P(g_x - g_y)$. If the departure from axial symmetry is larger, it is usually caused by d-orbital hybridization. The procedure is best illustrated by example.

Example—A low-spin Manganese(II) Complex

The spectrum of the low-spin manganese(II) complex, $[Mn(dppe)_2(CO)(CNBu)]^{2+}$, **5** (dppe = $Ph_2PCH_2CH_2PPh_2$) [48], in a CH_2Cl_2/THF glass is shown in Figure 5.3a. The spin Hamiltonian parameters, obtained from a least-squares fit of the field positions of the spectral features [49], are given in Table 2, and a computer simulation based on those parameters is shown in Figure 5.3b.

Table 2. ESR Parameters for $[Mn(dppe)_2(CO)(CNBu)]^{2+}$.

g	$A^{Mn}/10^{-4}$ cm^{-1}	$A^P/10^{-4}$ cm^{-1}
2.107	30.2	27.2
2.051	20.6	25.3
1.998	146.9	26.4

5 has approximate C_{2v} symmetry, although the actual symmetry is reduced to C_2 or C_s, depending on the conformation of the ethylene bridges of the dppe ligands. Since **5** has a nominal d^5 configuration, the SOMO is expected to be one of the "t_{2g}" orbitals of an idealized octahedral complex—d_{xz} (**b$_1$**), d_{yz} (**b$_2$**), or $d_{x^2-y^2}$ (**a$_1$**), where

the representations refer to C_{2v}. The energies of the d_{xz} and d_{yz} orbitals are expected to be lowered by back-donation into the p* orbitals of the CO and CNBu ligands so that the SOMO is most likely based on $d_{x^2-y^2}$, possibly with some symmetry-allowed d_{z^2} admixture,

Figure 5.3. (a) ESR spectrum of **5** in a CH_2Cl_2/THF glass (49); (b) Computer simulation using the parameters of Table 2.
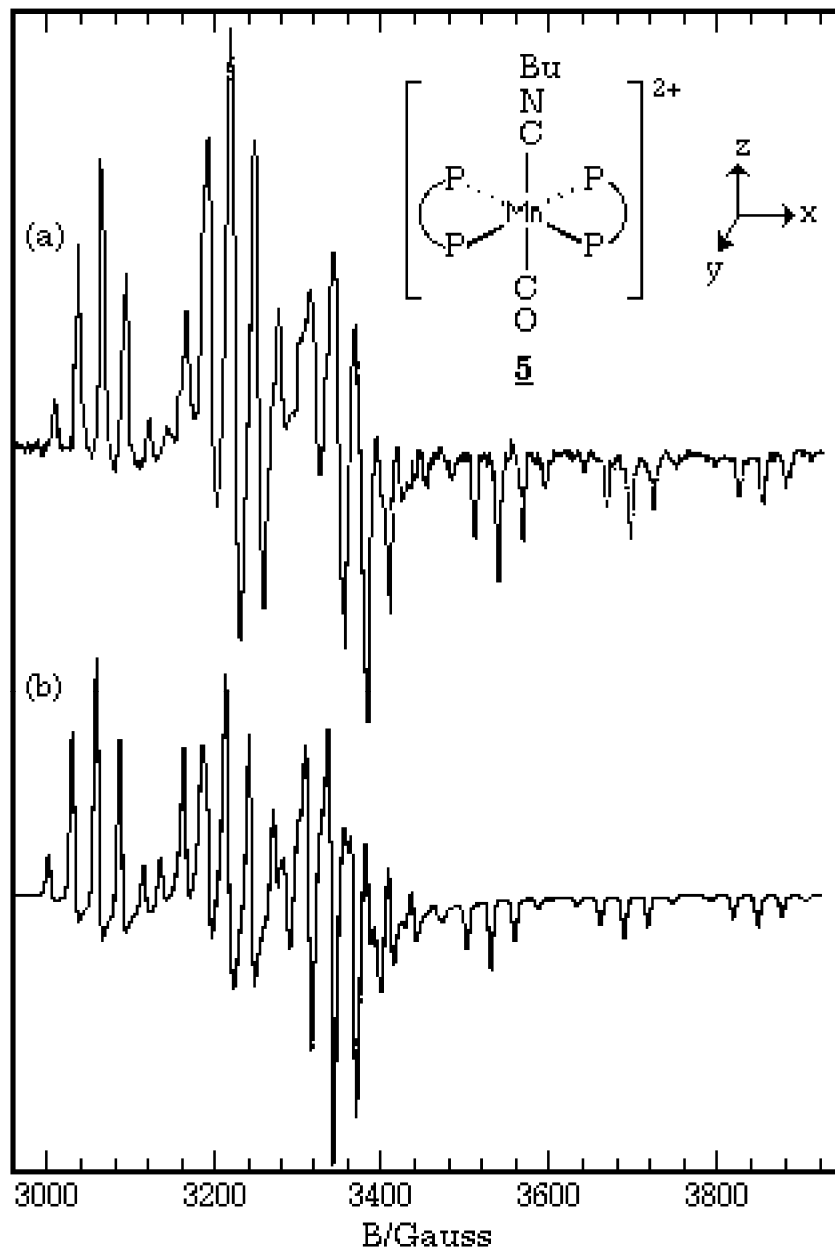
$$\left|\text{SOMO}\right\rangle = a\left|z^2\right\rangle + b\left|x^2-y^2\right\rangle + \cdots$$

(5.26)

Although the isotropic spectrum of **5** was not sufficiently resolved to unambiguously determine $\left(A^{Mn}\right)$, other closely related species give isotropic couplings on the order of 60-70 G [49]; if we assume an isotropic coupling in this range, all three matrix components must have the same sign.   If the isotropic

hyperfine coupling is negative, as expected if it arises mostly through polarization of inner-shell s orbitals, we have $\langle A \rangle = -65.9 \infty 10^{-4}$ cm^{-1}. Assuming that the SOMO is mostly d$_{x2-y2}$, ($b >> a$) and including the appropriate spin-orbit coupling corrections, we have [29,45]

$$A_z - \langle A \rangle = P\left[\frac{4}{7}\left(a^2 - b^2\right) - \frac{2}{3}\Delta g_z - \frac{5}{42}\left(\Delta g_x + \Delta g_y\right)\right]$$
(5.27)

With $\Delta g_z = -0.004$, $(\Delta g_x + \Delta g_y) = 0.154$, and $P = 207.6 \infty 10^{-4}$ cm^{-1} [40], we get $(a^2 - b^2) = -0.655$. The departure from axial symmetry is due to spin-orbit coupling and/or d$_{x2-y2}$/d$_{z2}$ hybridization,

$$A_x - A_y = P\left[-\frac{8\sqrt{3}}{7}ab + \frac{17}{14}\left(\Delta g_x - \Delta g_y\right)\right]$$
(5.28)

Substituting the parameters, we have $ab = \pm 0.058$. (The upper sign applies if the components are listed in the order x, y, z in Table 2, the lower sign if the order is y, x, z) Finally, we get $b^2 = 0.660$, $a^2 = 0.005$. The d$_{z2}$ component is not really significant, given the accuracy of the data and the theory, *i.e.*, most of the departure from axial symmetry can be explained by the spin-orbit coupling correction.

Using eq (5.11), the *g*-matrix components are found to be

$$\Delta g_{xx} = 2\zeta_{\text{Mn}} \sum_k \frac{b^2 c_{yz,k}^2}{E_0 - E_k}$$
(5.29a)

$$\Delta g_{yy} = 2\zeta_{\text{Mn}} \sum_k \frac{b^2 c_{xz,k}^2}{E_0 - E_k}$$
(5.29b)

$$\Delta g_{zz} = 2\zeta_{\text{Mn}} \sum_k \frac{4b^2 c_{xy,k}^2}{E_0 - E_k}$$
(5.29c)

If we assume coupling with single pure d$_{yz}$, d$_{xz}$, and d$_{xy}$ orbitals, we have $\Delta E_{yz} = 16\zeta$, $\Delta E_{xz} = 19\zeta$, $\Delta E_{xy} = -1100\zeta$, qualitatively consistent with the expected MO energy level scheme.

Example: Some Cobalt(0) Radical Anions

ESR spectra of [CpCo(1,3-COD)]$^-$, **6**, in frozen THF solution and [CpCo(1,5-COD)]$^-$, **7**, in frozen DMF were reported by Geiger and coworkers [50] and are reproduced in Figures 5.4a and 5.5a. These spectra have been reinterpreted to give the parameters shown in Table 3; computer-simulated spectra based on these parameters are shown in Figures 5.4b and 5.5b. Also shown in the table are the ESR parameters for [(C$_5$Ph$_5$)Co(CO)$_2$]$^-$, **8** [44].
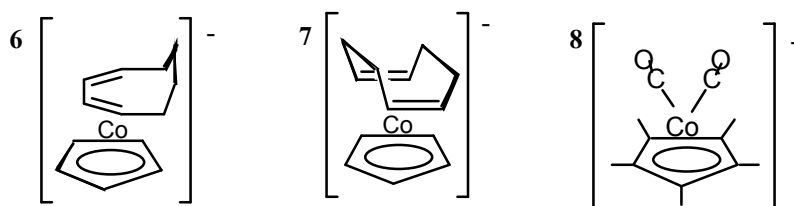
Table 3. ESR parameters for Cobalt(0) Radical Anions.

Radical Anion	g_x	g_y	g_z	$A_x{}^a$	$A_y{}^a$	$A_z{}^a$
[CpCo(1,5-COD)]$^-$	2.171	2.027	1.985	(–)158.6	(–)36.7	(–)45.8
[CpCo(1,3-COD)]$^-$	2.151	2.027	1.997	(–)139.2	(–)36.4	(–)38.2
[(C$_5$Ph$_5$)Co(CO)$_2$]$^{-b}$	2.018	2.041	1.995	(–)157.9	(–)16.8	(–)44.1

[a] Units of 10^{-4} cm^{-1}. [b] From reference 44.

The hyperfine matrix components must have identical signs in order that the average values match the observed isotropic couplings; we assume the signs are negative since the isotropic couplings almost certainly arise from polarization of inner shell s orbitals (see below).

The SOMO in these radicals is expected from extended Hückel MO calculations [50,51] to be primarily cobalt $3d_{yz}$ in character. In the **C_s** symmetry of the radicals, d_{yz} belongs to the **a"** representation and d-hybridization is possible only with d_{xy}. Assuming that such hybridization is negligible, the *g*-matrix components are given by [44]

$$\Delta g_{xx} = 2\zeta_{Co} \sum_k \frac{a^2\left(c_{x^2-y^2,k}\right)^2 + 3a^2\left(c_{z^2,k}\right)^2}{E_0 - E_k}$$

(5.30a)

$$\Delta g_{yy} = 2\zeta_{Co} \sum_k \frac{a^2\left(c_{xy,k}\right)^2}{E_0 - E_k}$$

(5.30b)

$$\Delta g_{zz} = 2\zeta_{Co} \sum_k \frac{a^2\left(c_{xz,k}\right)^2}{E_0 - E_k}$$

(5.30c)

Figure 5.4. ESR spectrum of $[CpCo(1,3\text{-}COD)]^-$; (a) experimental spectrum in frozen THF solution (from reference 50); (b) computer-simulation, based on the parameters of Table 3.

The dipolar contribution to the hyperfine matrix is given by eq (5.20), but spin-orbit coupling contributions are significant. These often can be expressed in terms of the *g*-matrix components (as in the Mn(II) example discussed above), but here spin-orbit coupling with the four other d-orbitals contributes somewhat differently to the *g*-matrix and to the hyperfine matrix. The simplest way of expressing the hyperfine matrix is in terms of the isotropic coupling, the *x*-component, and the departure from axial symmetry,

$$\langle A \rangle = A_s + \frac{1}{3} P\left(\Delta g_{xx} + \Delta g_{yy} + \Delta g_{zz}\right)$$

(5.31a)

$$A_x - \langle A \rangle = P\left[-\frac{4}{7}a^2 + \frac{2}{3}\Delta g_{xx} - \frac{5}{42}(\Delta g_{yy} + \Delta g_{zz})\right]$$
(5.31b)

$$A_y - A_z = \frac{17}{14}P\left(\Delta g_{yy} + \Delta g_{zz}\right)$$
$$+ \frac{6a^2\zeta P}{7}\left(\frac{1}{\Delta E_{x^2-y^2}} - \frac{1}{\Delta E_{z^2}}\right)$$
(5.31c)

With the assumed signs of the hyperfine components of Table 3, eq (5.31b) can be used unambiguously to compute $a^2 = \rho^d$ with the results shown in Table 4.

Since $3d_{yz}/4s$ admixture is symmetry-forbidden for these radicals, the Fermi contact contribution to the isotropic coupling must be entirely from spin polarization,

$$A_s = Q_d\rho^d$$
(5.32)

Thus we can obtain an independent estimate of the d-electron spin density from the values of A_s, taking $Q_d = -131 \propto 10^{-4}$ cm^{-1}, estimated from the isotropic cobalt coupling in [PhCCo$_3$(CO)$_9$]$^-$. The results are shown in the last column of Table 4. The spin densities estimated from the isotropic couplings are consistently about 10% higher than those from the dipolar coupling matrix, suggesting a systematic error in one of the parameters, but a reliable ordering of the spin densities.

Table 4. d-Electron spin densities in cobalt(0) radical anions.

Radical Anion	ρ^d	A_s[a]	A_s/Q_d
[CpCo(1,5-COD)]$^-$	0.681	-97.0	0.740
[CpCo(1,3-COD)]$^-$	0.591	-87.2	0.666
[(C$_5$Ph$_5$)Co(CO)$_2$]$^{-}$[b]	0.540	-77.4	0.591

[a] in units of 10^{-4} cm^{-1}.

The *g*-matrix presents an interesting problem in these cases. EHMO calculations [50,51] suggest that the SOMO is the highest-energy MO which is primarily cobalt 3d in character. At lower energy is an orbital with d_{xz} character and still lower, but grouped at about the same energy, are MO's with $d_{x^2-y^2}$, d_{xy}, and d_{z^2} contributions. Equations (5.30) then would suggest that $\Delta g_{xx}/4 \sim \Delta g_{yy} < \Delta g_{zz}$. With the assignments of Table 4, the first relationship is approximately correct for **6** and **7**, but very poor for **8**. The second relationship is not found for any of the anions. Reversing the *y* and *z* assignments makes the agreement worse. In discussing this problem for **8** [44], we postulated admixture of some cobalt $4p_y$ character in the SOMO,

$$\left|SOMO\right\rangle = a\left|yz\right\rangle + b\left|y\right\rangle + \cdots$$
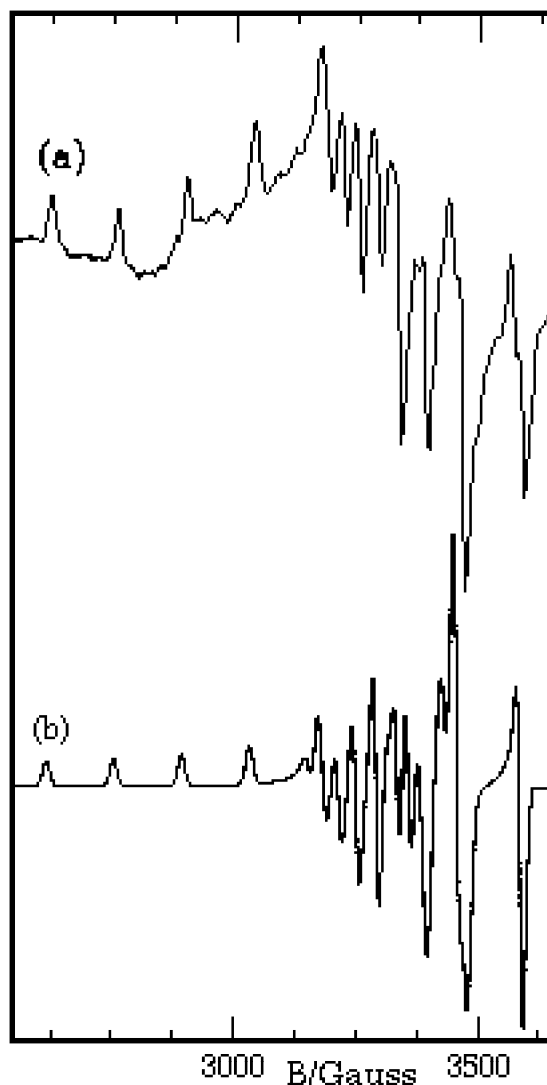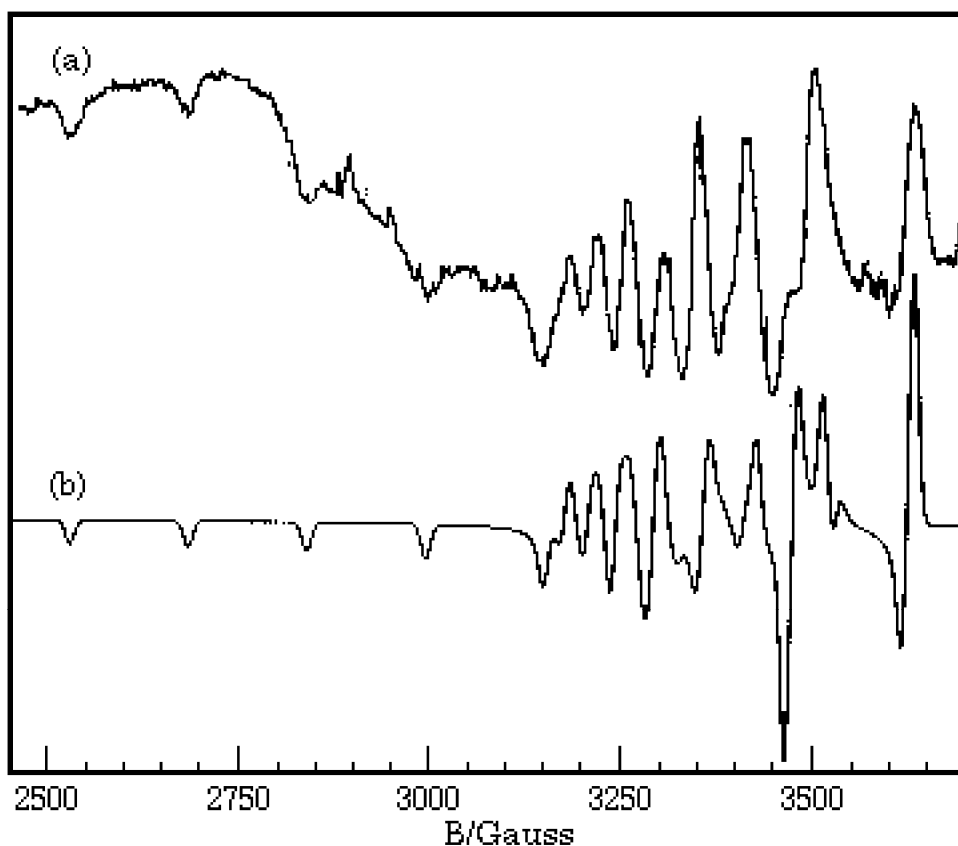(5.33)

Figure 5.5.   ESR spectrum of [CpCo(1,5-COD)]$^-$; (a) experimental spectrum in frozen DMF solution (from reference 50); (b) computer-simulation, based on the parameters of Table 3

which would result in additional contributions to g_{xx} and g_{zz},

$$g_{xx}(\text{p}) = 2\zeta_\text{p}b^2/\Delta E_z \quad \text{and} \quad g_{zz}(\text{p}) = 2\zeta_p b^2/\Delta E_x \qquad (5.34)$$

where ζ_p is the cobalt 4p spin-orbit coupling parameter ($\zeta_p \sim \zeta_d/3$). If MO's with significant p_z or p_x character lie just above the SOMO, then g_{xx} and g_{zz} would be less positive than expected from eqs (5.30), possibly even negative. g_{xx} is indeed smaller than expected for **8** and EHMO calculations do indeed suggest a MO with significant p_z character just above the SOMO in energy; this orbital is apparently substantially higher in energy in **6** and **7**. A MO with significant p_x character, at about the same energy for all three anions, is implied by these results but is unsubstantiated by the reported EHMO calculations.

Noncoincident Matrix Axes

In general, the *g*- and nuclear hyperfine coupling matrices, **g** and $\mathbf{A}_i$, can be written in diagonal form with three principal values—g_x, g_y, g_z and A_{ix}, A_{iy}, A_{iz}. In textbooks on ESR [2-7], it is usually assumed that the same set of principal axes diagonalizes all the relevant matrices. While this is sometimes true, there are many instances where the principal axes are noncoincident [52].

Symmetry Considerations. Kneubühl [53,54] has given a detailed group theoretical analysis of symmetry restrictions on the orientations of g- and hyperfine matrix principal axes. His results are summarized in Table 5. For a nucleus sharing all the molecular symmetry elements (*e.g.*, the metal nucleus in a mononuclear complex), the hyperfine matrix is subject to the same restrictions as the g-matrix. In orthorhombic or axial symmetry, such nuclear hyperfine matrices necessarily share principal axes with the g-matrix. In monoclinic symmetry, one hyperfine axis is also a g-matrix axis, but the other two may be different. In triclinic symmetry ($\mathbf{C_1}$ or $\mathbf{C_i}$), none of the three principal axes need be shared by the g-matrix and hyperfine matrix. The hyperfine matrix for a ligand atom (or for a metal in polynuclear complexes) is constrained only by the symmetry elements which the nucleus shares with the molecule.

Table 5. Symmetry restrictions on g-matrix components.

Symmetry	Point Groups	Restrictions on Diagonal Elements	Restrictions on Off-Diagonal Elements	Required Matrix Axes
Triclinic	$\mathbf{C_1, C_i}$	none	none	none
Monoclinic	$\mathbf{C_2, C_s, C_{2h}}$	none	$g_{xz} = g_{yz} = 0$	z
Orthorhombic	$\mathbf{C_{2v}, D_2, D_{2h}}$	none	$g_{xz} = g_{yz} = g_{xy} = 0$	x, y, z
Axial	$\mathbf{C_n, C_{nv}, C_{nh}},$ $\mathbf{D_n, D_{nd}, D_{nh}},$ n > 2	$g_{xx} = g_{yy}$	$g_{xz} = g_{yz} = g_{xy} = 0$	x, y, z

Although symmetry considerations often permit g- and hyperfine matrix principal axes to be noncoincident, there are relatively few cases of such noncoincidence reported in the literature. Most of the examples discussed by Pilbrow and Lowrey in their 1980 review [52] are cases of transition metal ions doped into a host lattice at sites of low symmetry. This is not to say that matrix axis noncoincidence is rare but that the effects have only rarely been recognized.

Experimental Determination of Matrix Axis Orientations. We have seen that spectra of dilute single crystals are analyzed in a way that gives the orientations of the g- and hyperfine matrix principal axes relative to the crystal axes. Historically, most of the information on noncoincident matrix axes is derived from such studies.

At first glance, it would appear that all orientation dependence should be lost in the spectrum of a randomly oriented sample and that location of the g- and hyperfine matrix principal axes would be impossible. While it is true that there is no way of obtaining matrix axes relative to molecular axes from a powder pattern, it is frequently possible to find the orientation of a set of matrix axes relative to those of another matrix.

The observable effects of matrix axis noncoincidence on powder patterns range from blatantly obvious to negligible. In general, the effects of axis noncoincidence will be more noticeable if two (or more) matrices have large anisotropies which are comparable in magnitude, *e.g.*, $\Delta g \mu_B B \sim \Delta A$. This follows from the fact that

minimum and maximum resonant fields are determined by a competition between extrema in the angle-dependent values of *g* and *A*. Consider the case of noncoincident *g*- and hyperfine matrix axes. For large values of $|m_I|$, the field extrema will be determined largely by the extrema in the effective hyperfine coupling and will occur at angles close to the hyperfine matrix axes, but for small $|m_I|$, the extrema will be determined by extrema in the effective *g*-value and will correspond to angles close to the *g*-matrix axes. The result of such a competition is that a series of features which would be equally spaced (to first order) acquires markedly uneven spacings.

There are two corollaries stemming from this generalization. Since spin 1/2 nuclei give only two hyperfine lines, there can be no variation in spacings. Thus powder spectra cannot be analyzed to extract the orientations of hyperfine matrix axes for such important nuclei as ^{1}H, ^{13}C, ^{19}F, ^{31}P, ^{57}Fe, and ^{103}Rh. Secondly, since the observable effects in powder spectra depend on the magnitude of the matrix anisotropies, the principal axes of the hyperfine matrix for a nucleus with small hyperfine coupling generally cannot be located from a powder spectrum, even though the relative anisotropy may be large.

Example—Chromium Nitrosyl Complex

A good example of the effect of *g*- and hyperfine matrix axis noncoincidence is the ESR spectrum of [CpCr(CO)$_2$NO]$^-$, **9**, studied by Geiger and coworkers [55] and

and shown in Figure 5.6. The *g*- and ^{14}N hyperfine matrices are approximately axial for this radical, but the $g_\parallel$ axis lies close to the perpendicular plane of the hyperfine matrix. If the $g_\parallel$ axis was exactly in the $A_\perp$ plane, the three negative-going $g_\parallel$ $A_\perp$ features, corresponding to resonant field maxima, would be evenly spaced. In fact, the spacings are very uneven, far more so than can be explained by second-order shifts. The effect can be understood, and the spectrum simulated virtually exactly, by assuming that the $g_\parallel$ axis is about 15° out of the $A_\perp$ plane.

Figure 5.6. Computer-simulated (a)absorption and (b) first-derivative spectra of **9**.
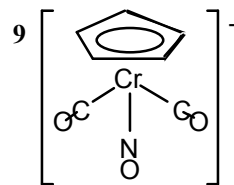
Example—Iron Pentacarbonyl Ions

Two particularly interesting organometallic examples were reported by Morton, Preston and coworkers [56,57]. Spectra of single crystals of Cr(CO)$_6$, doped with ^{13}C- or ^{57}Fe-enriched Fe(CO)$_5$ and γ-irradiated at 77 K, showed two different

radicals. One species, identified as $Fe(CO)_5^+$, showed coupling to [57]Fe and to a unique ^{13}C nucleus with axial hyperfine matrices sharing principal axes with the *g*-matrix [56]. Coupling was also observed to four other ^{13}C nuclei with identical coupling matrices but with the major axis approximately along the *g*-matrix *x*-axis for two nuclei and along the *g*-matrix *y*-axis for the other two. The parameters are listed in Table 6. If the radical is square pyramidal (**C4v**) $Fe(CO)_5^+$, **10**, the principal axes of the *g*-matrix must be the molecular axes (the **C4** axis and normals to the reflection planes). The iron atom and the carbon of the axial CO group have the full symmetry of the group and so these hyperfine matrices must share principal axes with the *g*-matrix. The four equatorial carbonyl carbons, on the other hand, lie in reflection planes, but not on the **C4**-axis and so are symmetry-required to share only one principal axis with the *g*-matrix. In fact, the major matrix axes for the equatorial carbons are tilted slightly in the *-z* direction from the ideal locations along the ±*x* and ±*y* axes. The *g*-matrix suggests that the metal contribution is d_{z^2} and the iron hyperfine matrix then can be used to estimate about 55% iron 3d and 34% axial carbon $2p_z$ spin density. The spin density on the equatorial carbons then is mostly negative and due to spin polarization.

Table 6. ESR Parameters for $Fe(CO)_5^+$ and $Fe(CO)_5^-$.[a]

$Fe(CO)_5^+$:	$g_\parallel = 2.001$	$A_\parallel^{Fe} = (+)9.4$	$A_\parallel^{C1} = (+)19.6$	$A_\parallel^{C2\text{-}C5} = (+)6.4$
	$g_\perp = 2.081$	$A_\perp^{Fe} = (-)6.2$	$A_\perp^{C1} = (-)17.6$	$A_\perp^{C2\text{-}C5} = (+)8.6$
$Fe(CO)_5^-$:	$g_1 = 1.989$	$A_1^{Fe} = (+)6.7$	$A_1^{C1} = (+)87.4$	
	$g_2 = 2.003$	$A_2^{Fe} = (-)4.5$	$A_2^{C1} = (+)70.7$	
	$g_3 = 2.010$	$A_3^{Fe} = (-)3.2$	$A_3^{C1} = (+)65.7$	

[a] Coupling constants in units of 10^{-4} cm^{-1}. Data from references 56 and 57.
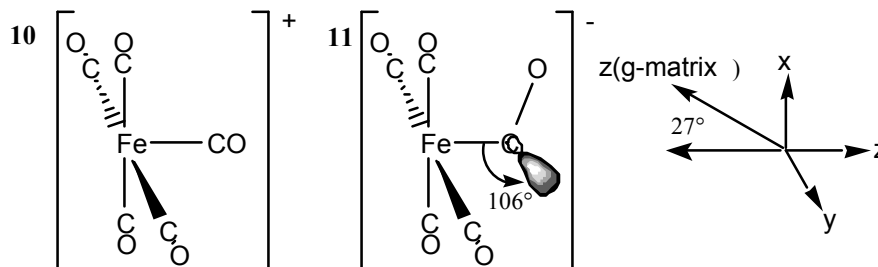
The other species observed in irradiated $Fe(CO)_5$-doped crystals of $Cr(CO)_6$ also showed coupling to [57]Fe, to a unique ^{13}C, and to four other carbons. However, in this case **g**, $\mathbf{A}^{Fe}$, and $\mathbf{A}^{C1}$ have only one matrix axis in common (that corresponding to the third component of each matrix listed in Table 6). The other [57]Fe hyperfine axes are rotated by about 27° and those of the ^{13}C hyperfine matrix by about 48° relative to the *g*-matrix axes. Insufficient data were accumulated to determine the complete hyperfine matrices for the other four carbons, but the components are considerably smaller (4 - 15 ∞ 10^{-4} cm^{-1}). The hyperfine matrices suggest about 38% iron $3d_{z^2}$, 18% carbon 2p, and 6% carbon 2s spin densities. Using detailed arguments regarding the orientation of the *g*-matrix axes relative to the crystal axes, the authors conclude that the carbon 2p axis is oriented at about 106° relative to the Fe-C bond axis and that the Fe-C-O bond angle is about 119°.

The most striking feature of these results is the orientation of the unique ^{13}C hyperfine matrix axes, relative to those of the ^{57}Fe hyperfine axes. This orientation led Fairhurst, *et al.*[57], to assign the spectrum to $Fe(CO)_5^-$, **11**, and to describe the species as a substituted acyl radical. However, these authors did not discuss the orientation of the *g*-matrix axes. The *y*-axis, normal to the reflection plane, is common to all three matrices. The *x*- and *z*- axes of the g-matrix, on the other hand are oriented about 27° away from the corresponding ^{57}Fe hyperfine matrix axes. Since the iron d-orbital contribution to the SOMO appears to be nearly pure d_{z^2}, the ^{57}Fe hyperfine matrix major axis must correspond to the local *z*-axis, assumed to be essentially the Fe-C bond. Thus we must ask: Why are the *g*-matrix axes different? The SOMO can be written

$$\left|\text{SOMO}\right\rangle = a\left|z^2,\text{Fe}\right\rangle + b_x\left|x,\text{C}\right\rangle + b_z\left|z,\text{C}\right\rangle \tag{5.35}$$

where $a = 0.62$, $b_x = -0.41$, and $b_z = 0.12$. Spin-orbit coupling will mix the SOMO with MO's having iron d_{yz} or d_{xz} character, but d_{yz} is involved in the π orbitals of the C=O group,

$$\left|\check{s}\right\rangle = c_{yz}\left|yz,\text{Fe}\right\rangle + c_y\left|y,\text{C}\right\rangle \tag{5.36}$$

Assuming that there is only one π orbital close enough in energy to couple significantly, eq (5.11) gives the *g*-matrix components:

$$\Delta g_{xx} = 2\,\zeta_{\text{Fe}}\,\frac{3a^2c_{yz}^2 + \sqrt{3}\,ab_zc_{yz}c_y}{\Delta E_{\check{s}}} \tag{5.37a}$$

$$\Delta g_{yy} = 2\,\zeta_{\text{Fe}}\,\frac{3a^2c_{xz}^2}{\Delta E_{xz}} \tag{5.37b}$$

$$\Delta g_{zz} = 0 \tag{5.37c}$$

$$g_{xz} = -2\,\zeta_{\text{Fe}}\,\frac{\sqrt{3}\,ab_xc_{yz}c_y}{\Delta E_{\check{s}}} \tag{5.37d}$$

The *g*-matrix can be diagonalized by rotation about the *y*-axis by the angle β,

$$\tan 2\beta = \frac{2\,g_{xz}}{g_{xx} - g_{zz}} = \frac{-2\sqrt{3}\,ab_x}{3\,a^2\left(c_{yz}/c_y\right) + \sqrt{3}\,ab_z} \tag{5.38}$$

With $\beta = 27°$, this expression gives $c_{yz}/c_y \sim 0.5$, a reasonable result.

This may be a rather general effect; if the unpaired electron in a radical is delocalized asymmetrically, and other MO's are similarly delocalized, the *g*-matrix will have off-diagonal elements which may be large enough to shift the principal axes away from the molecular coordinate system.

Example—Another low-spin Manganese(II) Complex

The low-spin manganese(II) complex, [Mn(dppe)$_2$(CO)(CNBu)]$^{2+}$, **5**, gave us a textbook example of a well-behaved ESR spectrum characterized by coincident *g*- and hyperfine matrix principal axes. The nearly identical complex, [Mn(dppm)$_2$(CO)(CN)]$^+$, **12$^+$**, provides us with a good example of non-coincident principal axes. T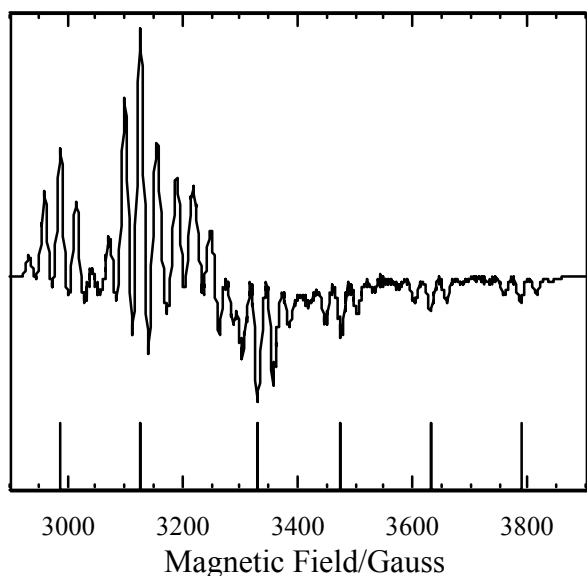he frozen solution spectrum, shown in Figure 5.7, shows that the "parallel" features are not evenly spaced. The spectrum can be understood if the *z*-axes of the *g*- and *A*-matrices are displaced by β = 19.6°. This, of course, tells us that the molecule does not have C_{2v} symmetry, and that, unlike the dppe analog, $d_{x^2-y^2}$ is not the only Mn contribution to the SOMO. One way of interpreting the results is that the Mn contribution to the SOMO incorporates a small amount of d_{xz} character. The consequence of this hybridization would be to tilt the "*x*" lobes of $d_{x^2-y^2}$ up and down, i.e., rotation about the *y*-axis. The reason for this hybridization is not difficult to discover. If the CH$_2$ groups of the dppm ligands were coplanar with Mn, the "*x*" lobes of the $d_{x^2-y^2}$ SOMO would be directed toward the carbon atoms and an anti-bonding

Figure 5.7. ESR spectrum of **12$^+$** in CH$_2$Cl$_2$/C$_2$H$_4$Cl$_2$ at 90 K; from reference (49).

interaction would result. In order to avoid this interaction, two things happen: (1) incorporation of d_{xz} character tilts the lobes up and down, away from the C atoms. At the same time, the x-ray structure of the Mn(II) cation shows (Figure 5.8) that the CH$_2$ groups tilt down and up, further decreasing the anti-bonding interaction. With only one electron in the SOMO, the anti-bonding interaction is strong enough to produce this distortion. With two electrons, the neutral parent Mn(I) complex would be expected to be even more distorted, and an x-ray structure shows that the up and down displacements of the CH$_2$ groups is approximately doubled.
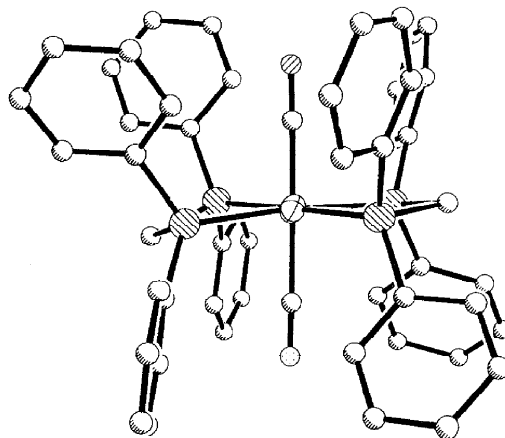

Figure 5.8. X-ray structure of **12$^+$**, showing methylene groups tilted up and down to avoid anti-bonding interaction with $d_{x^2-y^2}$ SOMO.

Example—Chromium(I) Piano-Stool Complex

Ordinarily, there is no way of extracting the orientation of the principal axes of the *g*-matrix from a powder or frozen solution ESR spectrum. However, there are exceptional circumstances in which nature is kind to the experimentalist!

Spectra of the low-spin d^5 Cr(I) complex, $[(C_5Ph_5)Cr(CO)_2PMe_3]$ **13** (58), are shown at 125 and 200 K in Figure 5.9 The low-temperature spectrum shows three sets of doublets, corresponding to the three *g*-components (2.104, 2.013, 1.994), each a doublet due to hyperfine coupling to ^{31}P. At 200 K, above the freezing point of toluene, the spectrum still appears as a "powder pattern", but the "perpendicular" features are nearly averaged and the "parallel" features have shifted upfield ($g_{\parallel}$ = 2.090, $g_{\perp}$ = 2.012). The exceptionally bulky C_5Ph_5 ligand apparently moves very slowly at 200 K but on the ESR time scale the $Cr(CO)_2PMe_3$ moiety rotates quickly, producing a spectrum averaged about the Cr-C_5 axis. With this interpretation, we can assign this axis as the principal axis for $g_{\parallel}$ measured at 200 K and, assuming that the $g_{\parallel}$ axis differs from the g_z axis by
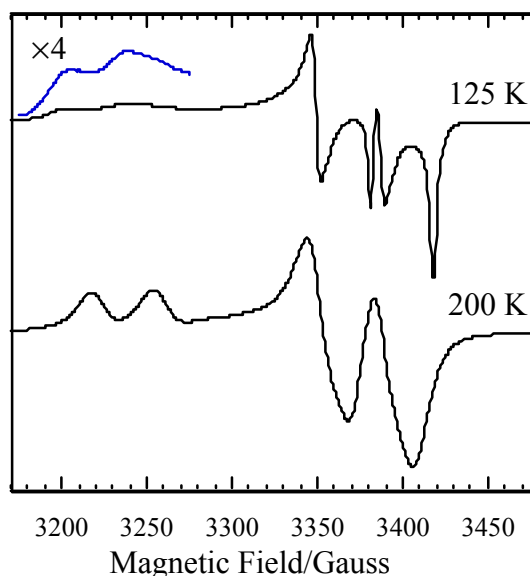
Figure 5.9. Spectra of **13** in toluene at 125 and 200 K; from reference (58).

the angle β and that g_z and g_x are averaged according to

$$2g_{\parallel}^2 = g_z^2 + g_x^2 + (g_z^2 + g_x^2)\cos^2 2\beta$$

Substitution of the *g*-components gives β = 15°

The symmetry of the complex is at most C_s, requiring one of the *g*-matrix principal axes to be normal to the plane of symmetry, assumed to be *xz*. p-back-bonding to the CO ligands is expected to lead to a hybrid SOMO. If, as suggested by extended Hückel MO calculations, the SOMO and first HOMO are of *a'* symmetry, and the second HOMO of *a"* symmetry:

$$\left|\text{SOMO}\right\rangle = a_1\left|x^2 - y^2\right\rangle + a_2\left|z^2\right\rangle + a_3\left|xz\right\rangle$$

$$\left|\text{HOMO}_1\right\rangle = b_1\left|x^2 - y^2\right\rangle + b_2\left|z^2\right\rangle + b_3\left|xz\right\rangle \quad \left|\text{HOMO}_2\right\rangle = c_1\left|xy\right\rangle + c_2\left|yz\right\rangle$$

the *g*-matrix components can be computed:

$$g_{xx} = g_e + \frac{\mathbf{z}_{Cr}\left(a_1c_2 + \sqrt{3}\,a_2c_2 + a_3c_1\right)^2}{E_0 - E_2} \qquad g_{zz} = g_e + \frac{\mathbf{z}_{Cr}\left(2a_1c_1 + a_3c_2\right)^2}{E_0 - E_2}$$

$$g_{yy} = g_e + \frac{\mathbf{z}_{Cr}\left[a_1b_3 - a_3b_1 + \sqrt{3}\left(a_3b_2 - a_2b_3\right)\right]^2}{E_0 - E_1}$$

$$g_{xz} = -\frac{\mathbf{z}_{Cr}\left(2a_1c_1 + a_3c_2\right)\left(a_1c_2 + \sqrt{3}\,a_2c_2 + a_3c_1\right)}{E_0 - E_2}$$

Rotation about the y-axis by β diagonalizes the matrix, and we find

$$\tan 2\beta = -\frac{2g_{xz}}{g_{zz} - g_{xx}}$$

The single experimental observable, β, is hardly enough to evaluate the LCAO coefficients for the SOMO and second HOMO, but we can compare the results of an extended Hückel MO calculation. (Since ζ_{Co} and $E_0 - E_2$ cancel in the calculation of $\tan 2\beta$, the EHMO calculation could come close). The results are: $a_1 = 0.538$, $a_2 = 0.216$, $a_3 = -0.194$, $c_1 = 0.582$, $c_2 = -0.061$, $\beta = 14.8°$. If we were to substitute these LCAO coefficients, together with the EHMO energy difference, into the expressions for g_{xx}, g_{yy}, g_{zz}, and g_{xz}, the results would be in very poor agreement with experiment; the moral here is that EHMO calculations, lacking charge self-consistency, usually have large errors in the energies, but the MO wavefunctions are often fairly accurate.

Example—[(RCCR')Co$_2$(CO)$_6$]$^-$ and [SFeCo$_2$(CO)$_9$]$^-$

Noncoincident matrix axis effects are seen in the frozen solution spectra of [(RCCR')Co$_2$(CO)$_6$]$^-$, **14** [59], and [SFeCo$_2$(CO)$_9$]$^-$, **15** [60], but the effects are rather more subtle than those discussed above.
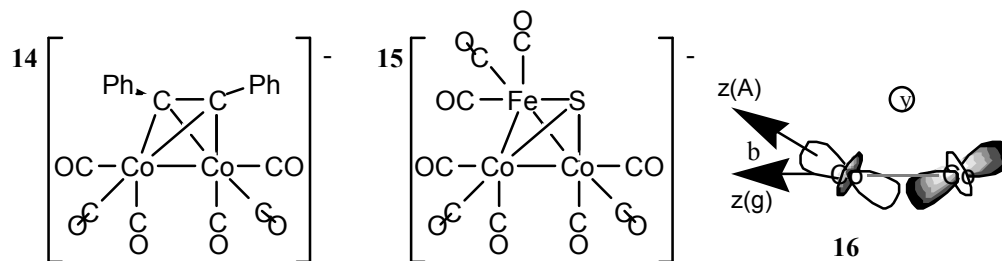
In these cases, the g-matrix is nearly isotropic, but the principal axes of the two ^{59}Co hyperfine matrices are noncoincident. The largest hyperfine matrix component ($a_y = 66.0$ G in the case of **15**) results in 15 features, evenly spaced (apart from small second-order shifts). Another series of features, less widely spaced, shows some variation in spacing and, in a few cases, resolution into components. This behavior can be understood as follows: Suppose that the

hyperfine matrix y-axes are coincident and consider molecular orientations with the magnetic field in the xz-plane. To first order, the resonant field then is

$$B = B_0 - m_1 a_+ - m_2 a_-$$ (5.39)

where $B_0 = h\nu/g\mu_B$ and

$$a_\pm^2 = a_z^2 \cos^2(\theta \pm \beta) + a_x^2 \sin^2(\theta \pm \beta)$$ (5.40)

where β describes the orientation of the hyperfine matrix z-axes relative to the g-matrix z-axis. Since **g** is nearly isotropic, the extrema in B are determined mostly by the hyperfine term. When $m_1 = m_2$, a_+ and a_- are equally weighted and the extrema occur at $\theta = 0$ or 90°, but when $m_1 \neq m_2$, the extrema correspond to other angles. Consider, for example, the five components of the $m_1 + m_2 = +3$ feature. With $|a_z| = 53.6$ G, $|a_x| = 15.5$ G, $\beta = 18°$, the hyperfine contributions to the field extrema and the corresponding values of θ are given in Table 7. In the experimental spectrum of **15**, two resolved field maximum features were seen, corresponding to the first two and the last three of the above components. Since the resolution is sensitive to the noncoincidence, it was possible to fit the experimental spectrum to obtain β quite accurately.

Table 7. Splitting of $M = 3$ features in $[SFeCo_2(CO)_9]^-$ Spectrum.

(m_1, m_2)	θ_{min}	$(B-B_0)_{min}/G$	θ_{max}	$(B-B_0)_{max}/G$
+7/2,-1/2	-20°	37.0	+67°	166.1
-1/2,+7/2	+20°	37.0	-67°	166.1
+5/2,+1/2	-15°	55.3	+78°	156.9
+1/2,+5/2	+15°	55.3	-78°	156.9
+3/2,+3/2	0°	66.5	90°	153.6

It is relatively easy to understand the significance of the noncoincident matrix axes in these cases. For **14**, the **C$_{2v}$** molecular symmetry permits a specific prediction of the possible matrix axis orientations. The g-matrix principal axes must be coincident with the molecular symmetry axes. The two cobalt nuclei are located in a reflection plane (which we label xz) so that symmetry requires the y-axis to be a principal axis for all three matrices. The other two axes may be rotated, relative to the molecular x- and z-axes, by $\pm\beta$. (Since the two nuclei are symmetrically equivalent, the rotations must be equal and opposite.)

Since the magnitudes and probable signs of the cobalt hyperfine matrices suggest a SOMO predominantly d_{z^2} in character, the major axes of the hyperfine matrices approximate the local z-axes at the cobalt atoms and the angular displacement indicates a bent Co-Co anti-bonding interaction, as shown in structure 16, where the C-C or Fe-S bond axis (the molecular y-axis) is perpendicular to the plane of the page. Comparison with the crystal structure of neutral $(Ph_2C_2)Co_2(CO)_6$ [61] shows that these local axes are roughly in the direction of the axial carbonyl ligands (the Co-CO bond is tilted 28° away from the Co-Co vector). Thus it seems reasonable to say that the local axes on a metal are determined primarily

by the more strongly interacting ligands and that bonds to other atoms can be described as bent.

Example—(o-xylylene)-Mn(dmpe)$_2$

As part of a study of Mn(II) dialkyls, Wilkinson, Hursthouse, and coworkers [62] reported the ESR spectrum of the approximately octahedral (o-xylylene)Mn(dmpe)$_2$, **17**, Figure 5.10a (dmpe = Me$_2$PCH$_2$CH$_2$PMe$_2$). The spectrum was interpreted assuming coincident g- and hyperfine matrix axes, but a simulation based on the reported parameters gave a very poor fit to the published spectrum. On closer examination, it was realized that this is a rather
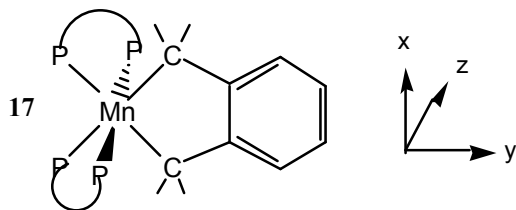
extreme example of a spectrum influenced by noncoincident g- and hyperfine matrix principal axes. The clue evident in the spectrum is the large gap between the $m_{Mn} = -1/2$ and +1/2 "parallel" features, suggesting one or more extra features. Figure 5.11 shows a set of simulated spectra for a hypothetical low-spin Mn(II) species; all seven spectra correspond to the same g- and hyperfine matrices, but the angle β, between the g- and hyperfine matrix z-axes, varies from 0 to 90°. As shown in Figure 5.11, it is possible to obtain spectra with more than six resolved "parallel" features. Indeed, the spectrum is sufficiently sensitive to the angle that β can be evaluated quite precisely. The final parameters for **17**, based on least-squares fitting of the positions of the resolved features and the isotropic parameters [53], are given in Table 8; a computer simulation using these parameters is shown in Figure 5.10b.
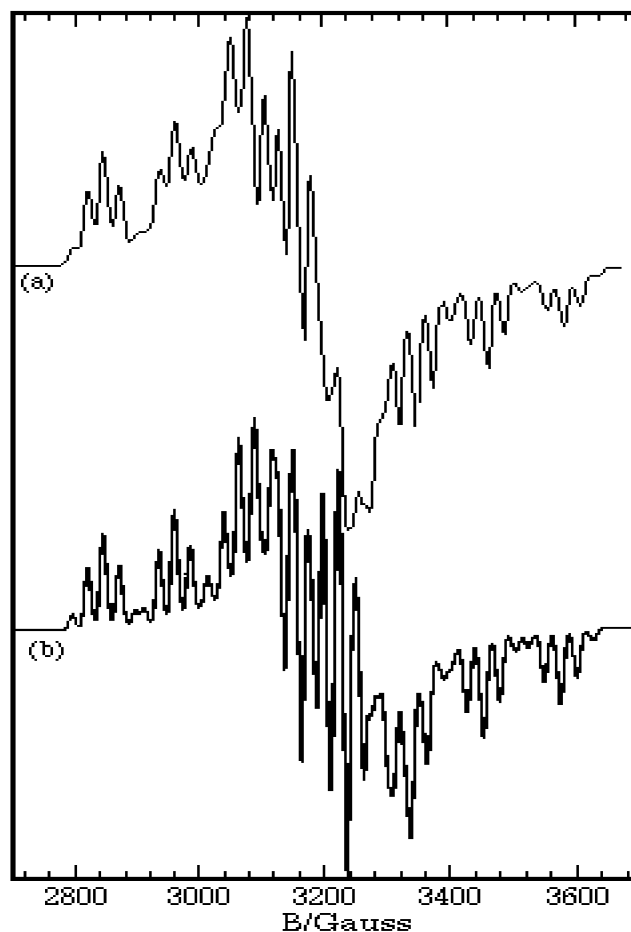
Figure 5.10. (a) ESR spectrum of (o-xylylene)Mn(dmpe)$_2$ in frozen toluene solution (from reference 53); (b) Computer simulation of spectrum using parameters of Table 8.

Table 8. ESR Parameters for (o-xylylene)Mn(dmpe)$_2$, **17**.[a]

g	A^{Mn}	A^P
2.110	27	24.5
2.035	27	24.5
2.000	125	24.5

[a] Hyperfine matrix components in units of 10^{-4} cm^{-1}; $\beta = 41°$.

Figure 5.11. Computer-simulated ESR spectra for a hypothetical low-spin Mn(II) radical with **g** = (2.100, 2.050, 2.000), A^{Mn} = (150, 25, 25) ∞ 10^{-4} cm^{-1}, for various values of β, the Euler angle between the g-matrix and hyperfine matrix z-axes.
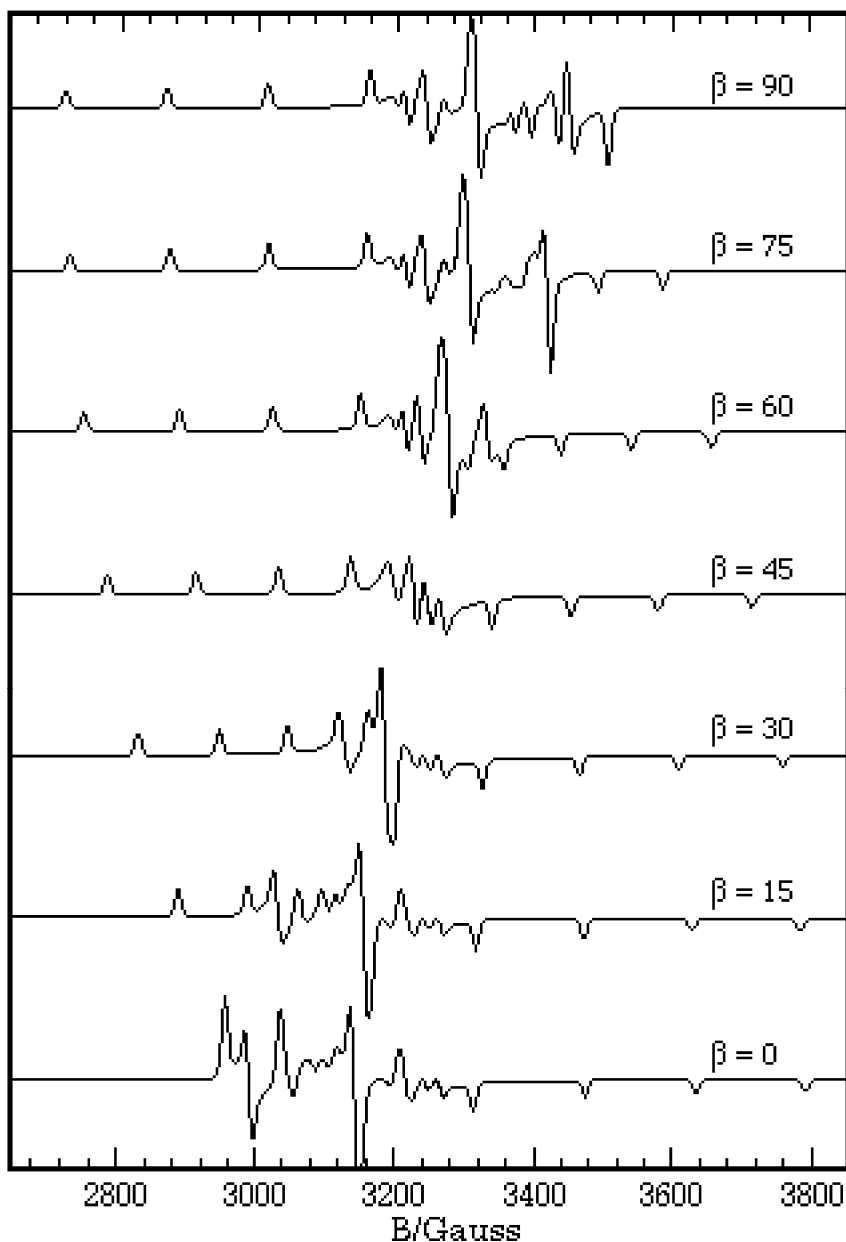
17 has approximate **C$_{2v}$** symmetry, but the ethylene bridges of the dmpe ligands destroy the reflection planes; the x-ray structure [53] shows a small fold at the

methylene groups of the o-xylylene ligand which destroys the $\mathbf{C_2}$ axis. Thus the molecule can be regarded, with increasing accuracy, as $\mathbf{C_{2v}}$, $\mathbf{C_s}$, $\mathbf{C_2}$, or $\mathbf{C_1}$. In order to explain the matrix axis noncoincidence, the metal contribution to the SOMO must be a d-hybrid. Since **17** is a d^5 low-spin Mn(II) species, the SOMO is expected to be dominated by one of the orbitals of the octahedral t_{2g} set—d_{xz}, d_{yz}, or $d_{x^2-y^2}$. This is consistent with a clue contained in the ESR parameters. The four ^{31}P couplings are apparently equivalent, and all are relatively small. Thus no lobe of the SOMO can be directed toward a phosphorus atom, and major d_{xy} or d_{z^2} contributions to the SOMO can be ruled out. Consider the twelve binary hybrids based on these orbitals which are listed in Table 9. Since we know that the

Table 9. SOMO Candidates: Binary d-Hybrids.

Number	Representation		Major d-AO	Minor d-AO	Approx. Major HF Axis	Common Axis
	$\mathbf{C_s}$	$\mathbf{C_2}$				
1	**a'**	**a**	$d_{x^2-y^2}$	d_{z^2}	z	x,y,z
2	**a'**	-	$d_{x^2-y^2}$	d_{yz}	z	x
3	**a'**	-	d_{yz}	$d_{x^2-y^2}$	x	x
4	**a'**	-	d_{yz}	d_{z^2}	x	x
5	**a"**	-	d_{xz}	d_{xy}	y	x
6	-	**a**	$d_{x^2-y^2}$	d_{xz}	z	y
7	-	**a**	d_{xz}	$d_{x^2-y^2}$	y	y
8	-	**a**	d_{xz}	d_{z^2}	y	y
9	-	**b**	d_{yz}	d_{xy}	x	y
10	-	-	$d_{x^2-y^2}$	d_{xy}	z	z
11	-	-	d_{xz}	d_{yz}	y	z
12	-	-	d_{yz}	d_{xz}	x	z

hyperfine matrix major axis is not a g-matrix principal axis, we can immediately reject hybrids 1, 3, 4, 7, 8, and 10 for which the major axis is a common axis. Hybrids 2 and 6, 5 and 9, and 11 and 12 differ only in the x- and y-labels and are essentially indistinguishable, so that there are only three cases to consider in detail.

Hybrid 6 can be written

$$\left|\text{SOMO}\right\rangle = a\left|x^2{-}y^2\right\rangle + b\left|xz\right\rangle \tag{5.41}$$

Straightforward application of eqs (5.24) yields a hyperfine matrix which can be diagonalized by rotation about the y-axis by the angle β,

$$\tan 2\beta = -2b/a \tag{5.42}$$

The *g*-matrix can be written in relatively simple form if we assume that the only MO's close enough in energy to contribute significantly are the filled MO's, primarily d_{xz} and d_{yz} in character. With this assumption, we obtain a matrix which can be diagonalized by rotation about the *y*-axis by β',

$$\tan 2\beta' = -\frac{2b/a}{1 - (b/a)^2} \tag{5.43}$$

For reasonable values of the hybridization ratio, b/a up to about 0.5, β and β' can differ by only a few degrees and this kind of hybrid cannot explain the matrix axis noncoincidence. Following the same reasoning with *x* and *y* interchanged, exactly the same conclusions can be reached for hybrid 2.

Hybrids 11 and 12 are

$$\left|\text{SOMO}\right\rangle = a\left|xz\right\rangle + b\left|yz\right\rangle \tag{5.44}$$

In this case, the hyperfine matrix remains axial, independent of the hybridization ratio, although the principal axes are rotated in the *xy*-plane by an angle α equal to angle β of eq (5.43). Assuming that only MO's with predominantly d_{xz}, d_{yz}, or $d_{x^2-y^2}$ character contribute, a *g*-matrix is found which can be diagonalized by rotation in the *xy*-plane by the angle α', also given by eq (5.43). Thus this hybrid gives identical *g*- and hyperfine matrix principal axes for all hybridization ratios.

Finally, hybrid 9,

$$\left|\text{SOMO}\right\rangle = a\left|yz\right\rangle + b\left|xy\right\rangle \tag{5.45}$$

gives an axial hyperfine matrix with principal axes rotated in the *xz*-plane by an angle β, given by eq (5.43). The *g*-matrix is somewhat more complicated,

$$\Delta\mathbf{g} = 2\zeta \begin{pmatrix} \dfrac{(ac_{x^2-y^2})^2}{\Delta E_{x^2-y^2}} + \dfrac{(bc_{xz})^2}{\Delta E_{xz}} & 0 & -\dfrac{2ab(c_{x^2-y^2})^2}{\Delta E_{x^2-y^2}} - \dfrac{ab(c_{xz})^2}{\Delta E_{xz}} \\[3ex] 0 & \dfrac{(bc_{yz})^2}{\Delta E_{yz}} & 0 \\[3ex] -\dfrac{2ab(c_{x^2-y^2})^2}{\Delta E_{x^2-y^2}} - \dfrac{ab(c_{xz})^2}{\Delta E_{xz}} & 0 & \dfrac{(2bc_{x^2-y^2})^2}{\Delta E_{x^2-y^2}} + \dfrac{(ac_{xz})^2}{\Delta E_{xz}} \end{pmatrix} \tag{5.46}$$

Diagonalization requires rotation about the *y*-axis by the angle β',

$$\tan 2\beta' = -\frac{2b}{a}\left[\frac{2Q+1}{Q-1-(b/a)^2(4Q-1)}\right]$$

(5.47)

where

$$Q = \frac{(c_{x^2-y^2})^2}{\Delta E_{x^2-y^2}} \bigg/ \frac{(c_{xz})^2}{\Delta E_{xz}}$$

(5.48)

Since the energy differences, $\Delta E_{x^2-y^2}$ and ΔE_{xz} are expected to be comparable, the parameter Q is probably not far from unity. For $Q = 1$, eq (5.47) has a particularly simple form, $\tan 2\beta' = +2a/b$ so that, for small b/a, we expect $\beta \sim 0$ and $\beta' \sim 45°$, entirely consistent with experiment. The axial hyperfine matrix is in agreement with experiment, and the principal values of the *g*-matrix can also be rationalized with reasonable values of Q and b/a. A small rotation of d_{yz} about the *y*-axis might reflect the small displacements of the phosphorus atoms from the idealized octahedral positions.

An extended Hückel MO calculation on **15** supports the assumptions made in the above analysis in that the three "t_{2g}" orbitals are indeed close together in energy and remain nearly nonbonding metal-based d-orbitals. The detailed agreement is less satisfactory: the SOMO is predicted to be primarily $d_{x^2-y^2}$ with a small d_{xz} admixture (hybrid 6 of Table 9), a result which can be ruled out from our analysis of the ESR results. The EHMO overlap matrix based on the x-ray structure suggests that the molecule is much closer to **C₂** symmetry than to **Cₛ**. If we accept that conclusion, then d_{xz}/d_{xy} hybridization is less likely than d_{yz}/d_{xy}, as we tacitly assumed above.

We considered several alternative explanations for the matrix axis noncoincidence in **15**. In particular, it seemed possible that delocalization of spin density into the o-xylylene ligand, either through the σ-bonds or into the π-system, might lead to significant contributions to the off-diagonal terms of the *g*-matrix. While the EHMO calculations suggest that the MO's containing $d_{x^2-y^2}$ and d_{yz} do have contributions from the carbon atoms of the o-xylylene group, the amount is far too small to rationalize rotation of the *g*-matrix axes by 41°; indeed, to explain the effect in this way would require each of several carbon atoms to contribute 5% or more to the MO's with $d_{x^2-y^2}$ or d_{yz} character, unreasonably large considering the poor overlap of these metal d-orbitals with the relevant carbon orbitals.

6. Molecules with More than One Unpaired Electron

Molecules with two or more unpaired electrons may be divided into two classes: By far the most common examples are molecules where the unpaired electrons are contained in a set of degenerate atomic or molecular orbitals with qualitatively similar spatial distributions, e.g., an octahedral Cr(III) ($^4\mathbf{A_{2g}}$) or Ni(II) ($^3\mathbf{A_{2g}}$) complex, or a triplet state molecule like O_2, or the excited triplet states of naphthalene or benzophenone.

A second class of molecules with two unpaired electrons has the two electrons localized, to a first approximation, in different parts of the molecule. We refer to such molecules as **biradicals**. Examples are the dinitroxides, and certain binuclear vanadium(IV) and copper(II) complexes.
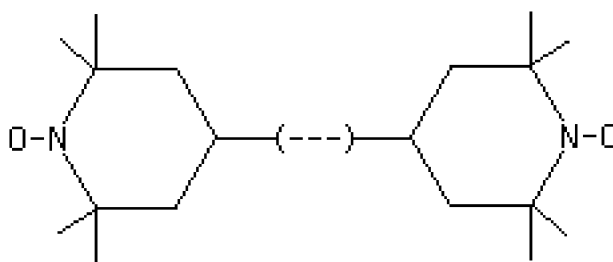
From the point of view of ESR spectroscopy, the distinction between molecules with one unpaired electron and those with more than one lies in the fact that electrons interact with one another; these interactions lead to additional terms in the spin Hamiltonian and additional features in the ESR spectrum. The most important electron-electron interaction is coulombic repulsion; with two unpaired electrons, repulsion leads to the singlet-triplet splitting. As we will see, this effect can be modelled by adding a term, $J\mathbf{S}_1 \cdot \mathbf{S}_2$, to the spin Hamiltonian, where J is called the **exchange coupling constant** and turns out to be equal to the singlet-triplet splitting.

In many cases, the singlet-triplet splitting is large compared with any other term in the spin Hamiltonian and we can safely ignore the singlet state, focusing entirely on the triplet. The simplification of being able to ignore the singlet state is more than compensated for by the introduction of a **fine structure term** into the spin Hamiltonian. This term, which has the form

$$D\left[S_z^2 - \tfrac{1}{3}S(S+1) + E\left(S_x^2 - S_y^2\right)\right]$$

(6.1)

introduces considerable complication into the shape and interpretation of ESR spectra. Further complicating the situation is the fact that the same term can arise from two quite different physical effects: **electron-electron dipolar interaction** and **spin-orbit coupling**.

The distinction between a biradical and an ordinary triplet state molecule is often somewhat fuzzy. For our purposes, we will consider a molecule a biradical if the exchange interaction between the two electrons is relatively weak, comparable in energy to the electron-nuclear hyperfine interaction. When the exchange interaction is weak, the singlet-triplet splitting is small and (as we will see) singlet-triplet mixing has an effect of the ESR spectrum. J falls off with electron-electron distance as $1/r$, whereas the dipolar coupling constant D falls off as $1/r^3$. Thus when J is small, D is negligible (though spin-orbit effects may contribute).

Biradicals and Exchange Coupling

In this section, we will consider the spin Hamiltonian appropriate to a biradical and see how ESR spectra of such species should appear. Obviously, it is possible to find triradicals, tetraradicals, etc.; treatment of such species is similar, though of course somewhat more complicated.

The spin Hamiltonian for a biradical consists of terms representing the electron Zeeman interaction, the exchange coupling of the two electron spins, and hyperfine interaction of each electron with the nuclear spins. We assume that there are two equivalent nuclei, each strongly coupled to one electron and essentially uncoupled to the other. The spin Hamiltonian is:

$$H_s = g\mu_B B\,(S_{1z} + S_{2z}) + A\,(\vec{S_1}\cdot\vec{I_1} + \vec{S_2}\cdot\vec{I_2}) + J\,\vec{S_1}\cdot\vec{S_2}$$

(6.2)

where J is the exchange coupling constant. Notice that we have also assumed that the g-values for the two electrons are the same. To simplify matters, we will assume that $|A| \ll g\mu_B B$ so that a first-order treatment of the hyperfine term will suffice. We choose as basis functions the singlet and triplet electron spin functions:

$$|S_0\rangle = \tfrac{1}{\sqrt{2}}\left(\left|\tfrac{1}{2}, -\tfrac{1}{2}\right\rangle - \left|-\tfrac{1}{2}, \tfrac{1}{2}\right\rangle\right)$$

(6.3a)

$$|T_0\rangle = \tfrac{1}{\sqrt{2}}\left(\left|\tfrac{1}{2}, -\tfrac{1}{2}\right\rangle + \left|-\tfrac{1}{2}, \tfrac{1}{2}\right\rangle\right)$$

(6.3b)

$$\left|\mathrm{T}_1\right\rangle = \left|\frac{1}{2}, \frac{1}{2}\right\rangle$$

(6.3c)

$$\left|\mathrm{T}_{-1}\right\rangle = \left|-\frac{1}{2}, -\frac{1}{2}\right\rangle$$

(6.3d)

The singlet function corresponds to zero total electron spin angular momentum, $S = 0$; the triplet functions correspond to $S = 1$. Operating on these functions with the spin Hamiltonian, we get

$$\hat{\mathbf{H}}_s \left|\mathrm{T}_1\right\rangle = \left[g\mu_B B + \frac{1}{4} J + \frac{1}{2} A \left(m_1 + m_2\right)\right] \left|\mathrm{T}_1\right\rangle$$

$$\hat{\mathbf{H}}_s \left|\mathrm{T}_{-1}\right\rangle = \left[-g\mu_B B + \frac{1}{4} J - \frac{1}{2} A \left(m_1 + m_2\right)\right] \left|\mathrm{T}_{-1}\right\rangle$$

$$\hat{\mathbf{H}}_s \left|\mathrm{T}_0\right\rangle = \frac{1}{4} J \left|\mathrm{T}_0\right\rangle + \frac{1}{2} A \left(m_1 - m_2\right) \left|\mathrm{S}_0\right\rangle$$

$$\hat{\mathbf{H}}_s \left|\mathrm{S}_0\right\rangle = -\frac{3}{4} J \left|\mathrm{S}_0\right\rangle + \frac{1}{2} A \left(m_1 - m_2\right) \left|\mathrm{T}_0\right\rangle$$

Thus $\left|\mathrm{T}_1\right\rangle$ and $\left|\mathrm{T}_{-1}\right\rangle$ and eigenfunctions of $\hat{\mathbf{H}}_s$, but $\left|\mathrm{T}_0\right\rangle$ and $\left|\mathrm{S}_0\right\rangle$ are mixed. (Notice, however, that if there were no hyperfine coupling, $A = 0$, then $\left|\mathrm{T}_0\right\rangle$ and $\left|\mathrm{S}_0\right\rangle$ would be eigenfunctions as well. In the absence of a hyperfine interaction, the triplet energy is $J/4$ and the singlet energy is $-3J/4$; J is normally negative so that the triplet lies lower in energy.)

To get the eigenvalues resulting from the admixture of $\left|\mathrm{T}_0\right\rangle$ and $\left|\mathrm{S}_0\right\rangle$, we solve the secular equation:

$$\begin{vmatrix} \frac{J}{4} - E & \frac{A}{2}\left(m_1 - m_2\right) \\ \frac{A}{2}\left(m_1 - m_2\right) & -\frac{3J}{4} - E \end{vmatrix} = E^2 + \frac{1}{2} JE - \frac{3}{16} J^2 - \frac{1}{4} A^2\left(m_1 - m_2\right)^2 = 0$$

The roots are:

$$E = -\frac{1}{4} J \pm \frac{1}{2} \sqrt{J^2 + A^2\left(m_1 - m_2\right)^2}$$

or, defining

$$R = \sqrt{J^2 + A^2\left(m_1 - m_2\right)^2}$$

we have

$$E = -\frac{1}{4} J \pm \frac{1}{2} R$$

The eigenfunctions corresponding to these energies may be found by inserting a value of E into one of the linear equations which led to the secular equation,

$$\left(\frac{1}{4}J - E\right)c_T + \frac{1}{2}A(m_1 - m_2)c_S = 0$$

$$\frac{1}{2}A(m_1 - m_2)c_T + \left(-\frac{3}{4}J - E\right)c_S = 0$$

where c_T and c_S are the coefficients of $|T_0\rangle$ and $|S_0\rangle$ in the eigenfunction corresponding to E ($c_T^2 + c_S^2 = 1$). The resulting eigenfunctions and energies are:

$$E_1 = g\mu_B B + \frac{J}{4} + \frac{A}{2}(m_1 + m_2) \qquad\qquad |1\rangle = |T_1\rangle$$

$$E_2 = -\frac{J}{4} + \frac{R}{2} \qquad\qquad |2\rangle = \sqrt{\frac{R+J}{2R}}\,|T_0\rangle + \sqrt{\frac{R-J}{2R}}\,|S_0\rangle$$

$$E_3 = -\frac{J}{4} - \frac{R}{2} \qquad\qquad |3\rangle = \sqrt{\frac{R-J}{2R}}\,|T_0\rangle - \sqrt{\frac{R+J}{2R}}\,|S_0\rangle$$

$$E_4 = g\mu_B B + \frac{J}{4} - \frac{A}{2}(m_1 + m_2) \qquad\qquad |4\rangle = |T_{-1}\rangle$$

Remembering that each of these is further split by the hyperfine interaction, there are obviously a number of possible transitions among these four energy levels. To find out which are important, we must evaluate the transition dipole moment matrix elements, $\langle i|\hat{S}_x|j\rangle$, since the absorption intensity is proportional to the square of these matrix elements. The operator S_x can be written

$$\hat{S}_x = \hat{S}_{1x} + \hat{S}_{2x} = \frac{1}{2}\left(\hat{S}_{1+} + \hat{S}_{1-} + \hat{S}_{2+} + \hat{S}_{2-}\right)$$

Applying S_x to $|1\rangle$ and $|4\rangle$, we have

$$\hat{S}_x|1\rangle = \frac{1}{2}\left(\hat{S}_{1+} + \hat{S}_{1-} + \hat{S}_{2+} + \hat{S}_{2-}\right)|1/2, 1/2\rangle = \frac{1}{2}\left(|-1/2, 1/2\rangle + |1/2, -1/2\rangle\right) = \sqrt{2}\,|T_0\rangle$$

$$\hat{S}_x|4\rangle = \frac{1}{2}\left(\hat{S}_{1+} + \hat{S}_{1-} + \hat{S}_{2+} + \hat{S}_{2-}\right)|-1/2, -1/2\rangle = \frac{1}{2}\left(|1/2, -1/2\rangle + |-1/2, 1/2\rangle\right) = \sqrt{2}\,|T_0\rangle$$

Thus the matrix elements are

$$\langle 1|\hat{S}_x|1\rangle = \langle 4|\hat{S}_x|4\rangle = \langle 1|\hat{S}_x|4\rangle = \langle 4|\hat{S}_x|1\rangle = 0$$

$$\langle 2|\hat{S}_x|1\rangle = \langle 2|\hat{S}_x|4\rangle = \langle 1|\hat{S}_x|2\rangle = \langle 4|\hat{S}_x|2\rangle = \sqrt{\frac{R+J}{R}}$$

$$\langle 3|\hat{S}_x|1\rangle = \langle 3|\hat{S}_x|4\rangle = \langle 1|\hat{S}_x|3\rangle = \langle 4|\hat{S}_x|3\rangle = \sqrt{\frac{R-J}{R}}$$

Since the relative intensity of a transition is proportional to the square of the corresponding matrix element of $\hat{S}_x$, we see that there are four allowed transitions:

$$\Delta E_{42} = g\mu_B B + \frac{1}{2}(R - J) + \frac{1}{2}A(m_1 + m_2) \qquad \text{Relative Intensity} = \frac{R + J}{R}$$

$$\Delta E_{43} = g\mu_B B - \frac{1}{2}(R + J) + \frac{1}{2}A(m_1 + m_2) \qquad \text{Relative Intensity} = \frac{R - J}{R}$$

$$\Delta E_{31} = g\mu_B B + \frac{1}{2}(R + J) + \frac{1}{2}A(m_1 + m_2) \qquad \text{Relative Intensity} = \frac{R - J}{R}$$

$$\Delta E_{21} = g\mu_B B - \frac{1}{2}(R - J) + \frac{1}{2}A(m_1 + m_2) \qquad \text{Relative Intensity} = \frac{R + J}{R}$$

Consider now the limiting case of strong exchange coupling. When $|J| \gg |A|$, $R \approx J$, and the 43 and 31 transitions are forbidden. The 42 and 21 transitions are at equal energy and so we have only

$$\Delta E = g\mu_B B + \frac{1}{2}A(m_1 + m_2) \tag{6.4}$$

Thus in the limit of strong exchange interaction, the resulting spectrum is identical to that which would be observed if one electron interacted with two equivalent nuclei with coupling constant, $A/2$.

In the limiting case of weak coupling, $|J| \ll |A|$, $R \approx A(m_1 - m_2)$, and all four transitions have equal relative intensities; the transition energies then are

$$\Delta E_{42} = \Delta E_{31} = g\mu_B B + \frac{A}{2}(m_1 - m_2) + \frac{A}{2}(m_1 + m_2) = g\mu_B B + Am_1 \tag{6.5a}$$

$$\Delta E_{43} = \Delta E_{21} = g\mu_B B - \frac{A}{2}(m_1 - m_2) + \frac{A}{2}(m_1 + m_2) = g\mu_B B + Am_2 \tag{6.5b}$$

Thus in the limit of negligible exchange interaction, we expect a spectrum identical to that observed for two independent radicals.

Now consider a concrete example. Suppose we have a nitroxide biradical with a^N = 13 G. In the strong exchange limit, we expect a five-line spectrum with a spacing of 6.5 G and the usual 1:2:3:2:1; intensity ratios for two equivalent spin 1 nuclei. In the weak exchange limit, we expect a three-line spectrum with a spacing of 13 G and intensity ratios 1:1:1. In intermediate cases, up to 15 lines are expected, as shown in Figure 6.1.

Organic Triplet State Molecules and the Dipolar Interaction

The Hamiltonian term for the electron-electron dipolar interaction is

$$\hat{\mathbf{H}}_d = g^2\mu_B^2 \left[\frac{\vec{\mathbf{s}}_1 \cdot \vec{\mathbf{s}}_2}{r^3} - \frac{(\vec{\mathbf{s}}_1 \cdot \vec{r})(\vec{\mathbf{s}}_2 \cdot \vec{r})}{r^5} \right] \tag{6.6}$$

where r is the vector pointing from electron 1 to electron 2. We have used a lower-case s for the one-electron spin operators, reserving upper-case S for the total electron spin operators. The dot products can be expanded to give
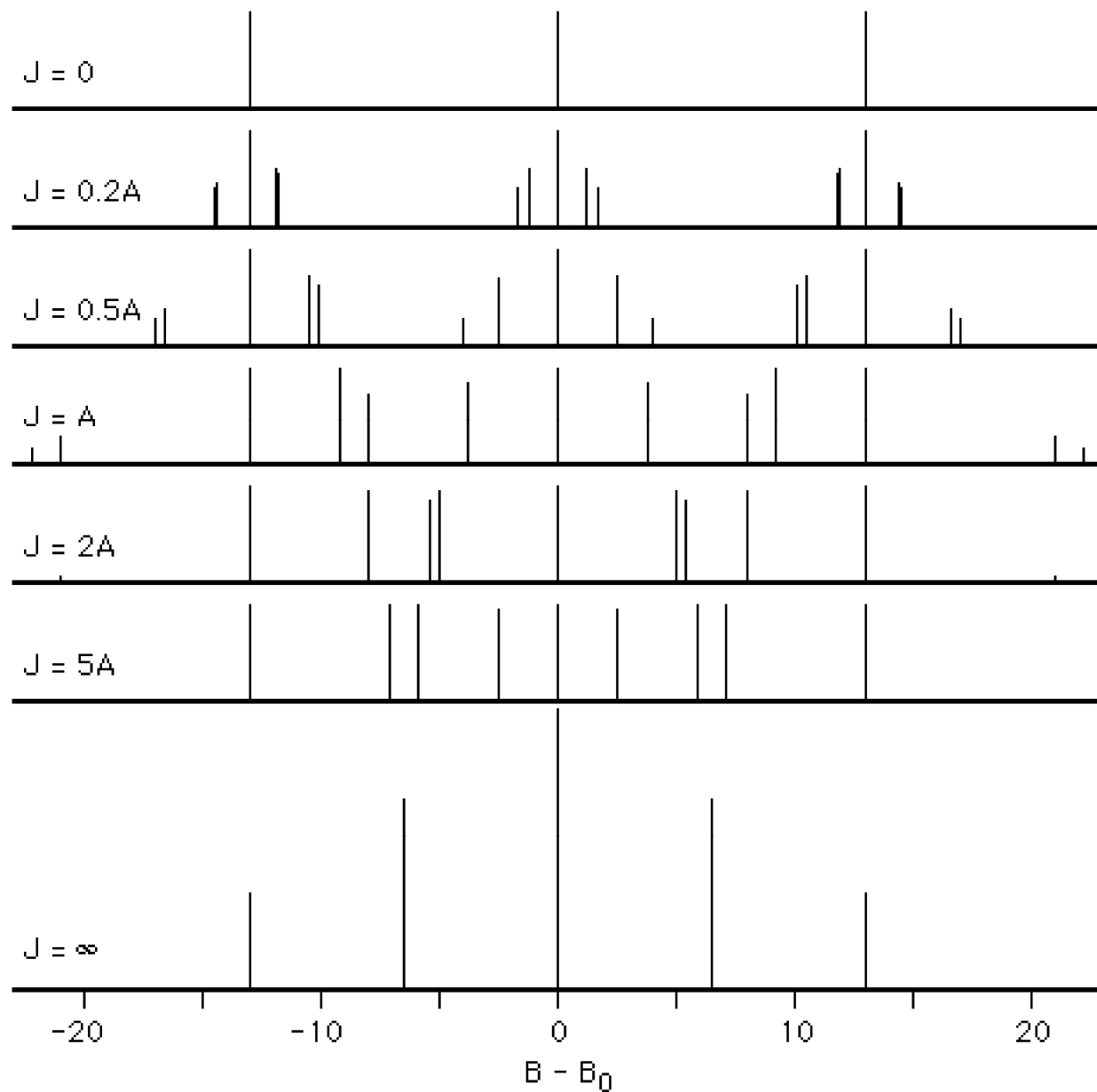

Figure 6.1. Stick spectra for a dinitroxide biradical with $a = 13$ G for various values of the exchange coupling constant J. (Several very small, widely spaced resonances have been omitted for $J = 2A$ and $J = 5A$).

$$\hat{\mathbf{H}}_d = g^2\mu_B^2\left[\frac{\left(r^2-3x^2\right)}{r^5}\hat{s}_{1x}\hat{s}_{2x}+\frac{\left(r^2-3y^2\right)}{r^5}\hat{s}_{1y}\hat{s}_{2y}+\frac{\left(r^2-3z^2\right)}{r^5}\hat{s}_{1z}\hat{s}_{2z}\right.$$

$$\left.-\frac{3xy}{r^5}\left(\hat{s}_{1x}\hat{s}_{2y}+\hat{s}_{2y}\hat{s}_{1x}\right)-\frac{3yz}{r^5}\left(\hat{s}_{1y}\hat{s}_{2z}+\hat{s}_{1z}\hat{s}_{2y}\right)-\frac{3zx}{r^5}\left(\hat{s}_{1z}\hat{s}_{2x}+\hat{s}_{1x}\hat{s}_{2z}\right)\right]$$

Our next goal is to transform this expression into one based on the total electron spin operator, $\mathbf{S} = \mathbf{s}_1 + \mathbf{s}_2$. The first three terms can be simplified by making use of the identity (derived using raising and lowering operators),

$$2s_{1i}s_{2i} = S_i^2 - \frac{1}{2} \qquad (i=x,y,z)$$

When these are substituted in the above expression, the terms arising from $-1/2$ cancel since $x^2 + y^2 + z^2 = r^2$. Transformation of the last three terms makes use of the identities,

$$2(s_{1i}s_{2j} + s_{1j}s_{2i}) = S_iS_j + S_jS_i$$

The transformed Hamiltonian then is

$$\hat{\mathbf{H}}_d = \frac{1}{2}g^2\mu_B^2\left[\frac{r^2-3x^2}{r^5}\hat{S}_x^2+\frac{r^2-3y^2}{r^5}\hat{S}_z^2+\frac{r^2-3z^2}{r^5}\hat{S}_z^2\right.$$

$$\left.-\frac{3xy}{r^5}\left(\hat{S}_x\hat{S}_y+\hat{S}_y\hat{S}_x\right)-\frac{3xyz}{r^5}\left(\hat{S}_y\hat{S}_z+\hat{S}_z\hat{S}_y\right)-\frac{3zx}{r^5}\left(\hat{S}_z\hat{S}_x+\hat{S}_x\hat{S}_z\right)\right]$$

The coefficients of the spin operators must be evaluated using the electron wave function, an operation which not usually possible in practice. However, we can parameterize the problem, defining the matrix **D** with elements

$$D_{ij} = \frac{1}{2}g^2\mu_B^2\left\langle\frac{r^2\delta_{ij}-3ij}{r^5}\right\rangle$$

$$(6.7)$$

where the angle brackets indicate averaging over the spatial coordinates of the wave function.

It is possible to choose an axis system in which the **D**-matrix is diagonal—the principal axes. In many cases, these axes will also be the principal axes of the **g**-matrix and we will so assume in the following.

Since the trace of **D** ($D_{xx} + D_{yy} + D_{zz}$) is zero, there are really only two independent parameters. The conventional choice of these parameters is

$$D = \tfrac{3}{2} D_{zz} \qquad\qquad E = \tfrac{1}{2}\left(D_{xx} - D_{yy}\right)$$

$$D_{zz} = \tfrac{2}{3} D \qquad\qquad D_{xx} = -\tfrac{1}{3}D + E \qquad\qquad D_{yy} = -\tfrac{1}{3}D - E$$

or

The Hamiltonian then becomes

$$\hat{\mathbf{H}}_d = D_{xx}\hat{\mathbf{S}}_x^{\,2} + D_{yy}\hat{\mathbf{S}}_y^{\,2} + D_{zz}\hat{\mathbf{S}}_z^{\,2} \tag{6.8a}$$

$$\hat{\mathbf{H}}_d = D\left[\hat{\mathbf{S}}_z^{\,2} - \tfrac{1}{3}\left(\hat{\mathbf{S}}_x^{\,2} + \hat{\mathbf{S}}_y^{\,2} + \hat{\mathbf{S}}_z^{\,2}\right)\right] + \tfrac{1}{2}E\left(\hat{\mathbf{S}}_x^{\,2} - \hat{\mathbf{S}}_y^{\,2}\right)$$

or $\tag{6.8b}$

We can somewhat simplify the Hamiltonian by noting that $S_x^2 + S_y^2 + S_z^2 = S^2$ and the eigenvalue of S^2 is $S(S + 1)$, and that S_x and S_y can be written in terms of the raising and lowering operators:

$$\hat{\mathbf{H}}_d = D\left[\hat{\mathbf{S}}_z^{\,2} - \tfrac{1}{3}S(S + 1)\right] + E\left(\hat{\mathbf{S}}_+^{\,2} + \hat{\mathbf{S}}_-^{\,2}\right) \tag{6,9}$$

We will see that a Hamiltonian term identical in form also arises from spin-orbit coupling, but first we will pause to see the effect of this Hamiltonian on the energy levels and ESR spectrum of a triplet-state molecule. The spin triplet wave functions can be written in the notation $|S,m_s\rangle$

$$\hat{\mathbf{H}}_d\,|1,1\rangle = D\left(1 - \tfrac{2}{3}\right)|1,1\rangle + E\,|1,-1\rangle$$

$$\hat{\mathbf{H}}_d\,|1,0\rangle = D\left(0 - \tfrac{2}{3}\right)|1,0\rangle$$

$$\hat{\mathbf{H}}_d\,|1,-1\rangle = D\left(1 - \tfrac{2}{3}\right)|1,-1\rangle + E\,|1,1\rangle$$

The Hamiltonian matrix then is

$$\begin{pmatrix} D/3 & 0 & E \\ 0 & -2D/3 & 0 \\ E & 0 & D/3 \end{pmatrix}$$

Solution of the corresponding secular equation leads to energy levels, $-2D/3$ and $D/3 \pm E$. The splitting pattern is shown in Figure 6.2.

Notice that if the molecule has axial symmetry, $D_{xx} = D_{yy}$ so that $E = 0$. If the molecule has octahedral symmetry, $D_{xx} = D_{yy} = D_{zz}$ so that $D = E = 0$. Thus the

appearance of a zero-field splitting into two or three levels tells the spectroscopist something about the symmetry of the molecule. It is possible, of course, to do spectroscopy on these energy levels at zero magnetic field. Our concern here is the effect of zero-field splitting on the ESR spectrum where a magnetic field is applied.

When we include the Zeeman interaction term, $g\mu_B\mathbf{B}{\cdot}\mathbf{S}$, in the spin Hamiltonian, a complication arises. We have been accustomed to evaluating the dot product by simply taking the direction of the magnetic field to define
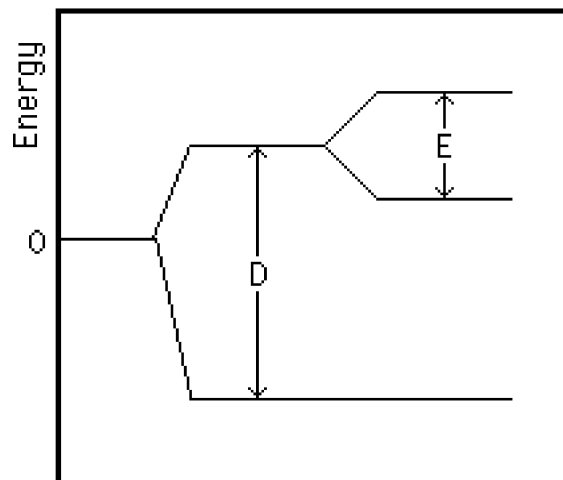

Figure 6.2. Zero-field splitting of a triplet state.

the z-axis (the axis of quantization). When we have a strong dipolar interaction, the molecule defines a quantization axis for itself. Thus in general the $\mathbf{B}{\cdot}\mathbf{S}$ term has three components. It is possible to deal with the general case, but the algebra is very messy and not very enlightening. Instead we will assume that the triplet molecule is in a dilute single crystal and that we can orient the crystal in the field with $\mathbf{B}$ along one of the internal coordinate axes.

Suppose that we orient the crystal with $\mathbf{B}$ in the z-direction. The spin Hamiltonian then is

$$\hat{\mathbf{H}}_s = g\mu_B B \hat{\mathbf{S}}_z + D\left[\hat{\mathbf{S}}_z^{\,2} - \tfrac{1}{3}S(S+1)\right] + \tfrac{1}{2}E\left(\hat{\mathbf{S}}_+^{\,2} + \hat{\mathbf{S}}_-^{\,2}\right)$$

Operating on the triplet wave functions as before, we get the Hamiltonian matrix

$$\begin{pmatrix} g\mu_B B + \tfrac{1}{3}D & 0 & E \\ 0 & -\tfrac{2}{3}D & 0 \\ E & 0 & -g\mu_B B + \tfrac{1}{3}D \end{pmatrix}$$

Solution of the secular equation leads to the energies:

$$-\tfrac{2}{3}D,\ \tfrac{1}{3}D \pm \sqrt{g^2\mu_B^2 B^2 + E^2}$$

These are plotted vs. magnetic field in Figure 6.3, using $D = 0.1003$ cm^{-1}, $E = -0.0137$ cm^{-1}, parameters appropriate to the excited triplet of naphthalene. The energies of the allowed transitions are

$$\Delta E = \sqrt{g^2 \mu_B^2 B^2 + E^2} \pm D$$

At constant frequency, $\nu_0 = \Delta E / h$, the resonant fields are:

$$B = \frac{1}{g\mu_B} \sqrt{\left(h\nu_0 \pm D\right)^2 - E^2}$$

With the magnetic field oriented along the x-axis, the Hamiltonian is

$$\hat{\mathbf{H}}_s = g\mu_B B \hat{\mathbf{S}}_x + D \left[\hat{\mathbf{S}}_z^2 - \tfrac{1}{3} S(S+1)\right] + \tfrac{1}{2} E \left(\hat{\mathbf{S}}_+^2 + \hat{\mathbf{S}}_-^2\right)$$

The Hamiltonian matrix is

$$\begin{pmatrix} \frac{1}{3} D & \frac{1}{\sqrt{2}} g\mu_B B & E \\ \frac{1}{\sqrt{2}} g\mu_B B & -\frac{2}{3} D & \frac{1}{\sqrt{2}} g\mu_B B \\ E & \frac{1}{\sqrt{2}} g\mu_B B & \frac{1}{3} D \end{pmatrix}$$

The cubic secular equation factors; the resulting energies are

$$\frac{D}{3} - E, \quad -\frac{D - 3E}{6} \pm \sqrt{g^2 \mu_B^2 B^2 + \tfrac{1}{4}\left(D + E\right)^2}$$

These energies are also plotted in Figure 6.3; energies of the allowed transitions are

$$\Delta E = \sqrt{g^2 \mu_B^2 B^2 + \tfrac{1}{4}\left(D + E\right)^2} \pm \tfrac{1}{2}\left(D - 3E\right)$$

The resonant fields then are

$$B = \frac{1}{g\mu_B} \sqrt{\left(h\nu_0 \pm \tfrac{1}{2}\left(D - 3E\right)\right)^2 - \tfrac{1}{4}\left(D + E\right)^2}$$

Organic Triplet-State Molecules. The phosphorescent triplet state of naphthalene is produced by irradiation of naphthalene doped into a single crystal of durene. The triplet state is long-lived at 77 K. The energy-level diagram, shown in Figure 6.3, predicts two transitions: at 2315 and 4465 G when the field is oriented along the z-axis, at 2595 and 4125 G for orientation along the x-axis ($\nu_0 = 9.50$ GHz).

The experimental determination of D and E for a dilute single crystal is not trivial, even when the crystal axes are known. Durene, for example, has two molecules per unit cell with different orientations of the molecular plane. Thus for any orientation there are four resonances, two from each type of site. Sorting out the data is a challenging exercise.
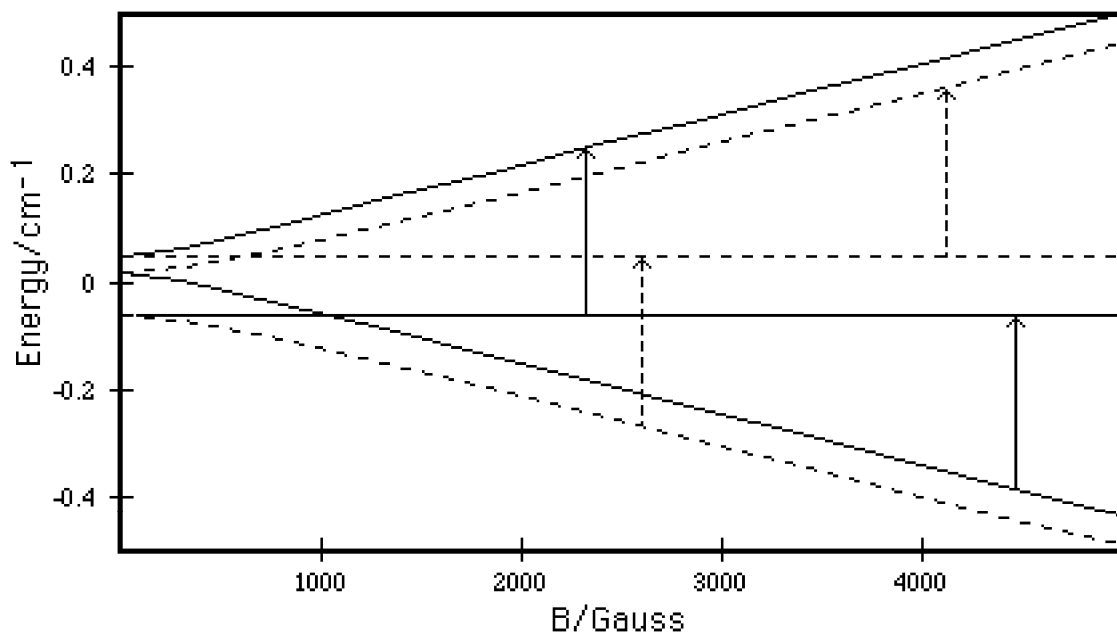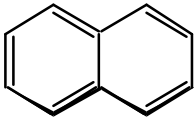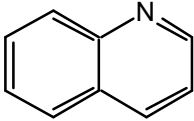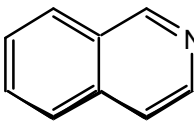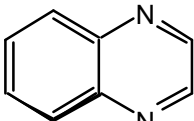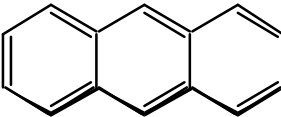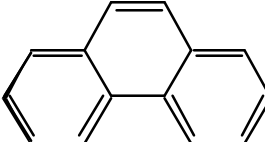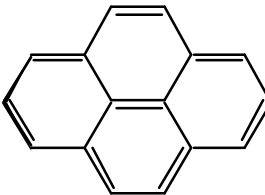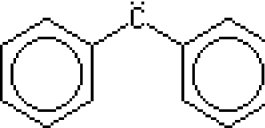
Figure 6.3. Energy level diagram for the triplet state of naphthalene (D = 0.1003 cm^{-1}, E = –0.0137 cm^{-1}, g = 2.003). Solid lines correspond to orientation of the magnetic field along the z-axis, dashed lines for orientation along the x-axis. Arrows show the allowed transitions for 9.50 GHz microwave radiation..

Triplet state powder spectra (or frozen solution glasses) are generally easier to interpret and much easier to get experimentally than dilute single crystal spectra. The features of the derivative spectrum correspond to orientations along the principal axis directions. Thus six features can be found in the spectrum of naphthalene in glassy THF solution at 77 K (after irradiation). The problem, as is usual with powder spectra, is that there is no way to assign the features to molecular axes; recourse must be made to theoretical considerations or to analogy with a related system studied in a dilute single crystal.

Table 8. ESR Data for some Organic Triplet-State Molecules.

Molecule	Structure	D/cm^{-1}	E/cm^{-1}
Naphthalene		0.1003	–0.0137
Quinoline		0.1030	–0.0162
Isoquinoline		0.1004	–0.0117
Quinoxaline		0.1007	–0.0182
Anthracene		0.0716	–0.0084
Phenanthrene		0.1004	–0.0466
Pyrene		0.0678	–0.0314
Diphenylmethylene		0.3964	–0.0152

Since the resonances are spread over a large range of field and are very orientation dependent, there is little hope of detecting the resonance of a triplet state molecule in liquid solution, even if the triplet state lifetime could be made long enough.

What do we make of the parameters D and E once we have extracted them from a spectrum? Eight examples are given in Table 8. There are some qualitative trends which make some sense. Since D is a measure of the dipolar interaction of the two unpaired electrons, we might expect that D would be large when both

electrons are forced to be close together and diphenylmethylene does indeed give the largest value of D. When the p-system remains about the same size but heteroatoms are substituted, we might expect that D would not change by much and we see that naphthalene and related nitrogen heterocyclics do indeed have nearly the same values of D. When the p-system gets bigger, we might expect D to decrease and anthracene and pyrene fulfill this expectation, but phenanthrene seems anomalous. To go beyond a qualitative explanation of D or to explain E at all requires rather sophisticated valence theory calculations. Indeed electron dipolar interaction parameters provide one of the more challenging test of a valence theory method.

Spin-Orbit Coupling and Transition Metal Complexes

We now will show that spin-orbit coupling can give a spin Hamiltonian term identical to that which we obtained from the electron dipolar interaction. Consider the spin Hamiltonian including orbital angular momentum and the usual spin-orbit coupling term:

$$\hat{\mathbf{H}}_s = \mu_B \vec{B} \cdot \left(\vec{\mathbf{L}} + g_e \vec{\mathbf{S}} \right) + l\vec{\mathbf{L}} \times \vec{\mathbf{S}} \tag{6.10}$$

where λ is the spin-orbit coupling constant. The zero-order ground state wave function will be characterized by the quantum numbers, L, m_L, S, m_S, and we assume that the wave function is orbitally nondegenerate, *i.e.*, $m_L = 0$. Thus we write the ground state wave function as $|m_L, m_S\rangle = |0, m_S\rangle$. With **B** defining the z-axis, the energy is easily found to first order in perturbation theory

$$E^{(1)} = g\mu_B B \, m_S \tag{6.11}$$

since $\mathbf{L_z}|0, m_S\rangle = 0$. The second-order energy is not so simple since the excited states in general have nonzero m_L. Thus we get second-order contributions from matrix elements connecting $|0, m_S\rangle$ with excited state functions:

$$E^{(2)} = - \sum_i \frac{\left| \left\langle 0, m_{S,0} \right| \left(\mu_B \vec{B} + \lambda \vec{\mathbf{S}} \right) \cdot \vec{L} + g_e \mu_B \vec{B} \cdot \vec{\mathbf{S}} \left| m_{L,i}, m_{S,i} \right\rangle \right|^2}{E_i^{(1)} - E_0^{(1)}} \tag{6.12}$$

The matrix element can be expanded and written as

$$\left\langle m_{S,0} \right| \left(\mu_B \vec{B} + \lambda \vec{\mathbf{S}} \right) \left| m_{S,i} \right\rangle \left\langle 0 \left| \vec{\mathbf{L}} \right| m_{L,i} \right\rangle + g_e \mu_B \vec{B} \cdot \left\langle m_{S,0} \left| \vec{\mathbf{S}} \right| m_{S,i} \right\rangle \left\langle 0 \left| m_{L,i} \right\rangle \right.$$

Since the orbital functions , $\langle 0|$ and $|m_{L,i}\rangle$, are orthogonal, the second term vanishes. The absolute value square of the matrix element of a Hermitean operator can be written as

$$\left| \left\langle i \left| \mathbf{Op} \right| j \right\rangle \right|^2 = \left\langle i \left| \mathbf{Op} \right| j \right\rangle \left\langle j \left| \mathbf{Op} \right| i \right\rangle$$

Thus we can write $E^{(2)}$ as

$$E^{(2)} = \sum_{m_S'} \left\langle m_{S,0} \middle| \mu_B \vec{B} + \lambda \vec{S} \middle| m_S' \right\rangle \cdot \left(\sum_i \frac{\left\langle 0 \middle| \vec{L} \middle| m_L \right\rangle \left\langle m_L \middle| \vec{L} \middle| 0 \right\rangle}{E_i^{(1)} - E_0^{(1)}} \right) \cdot \left\langle m_S' \middle| \mu_B \vec{B} + \lambda \vec{S} \middle| m_{S,0} \right\rangle$$

Defining
$$\overset{\leftrightarrow}{\Lambda} = \sum_i \frac{\left\langle 0 \middle| \vec{L} \middle| m \right\rangle \left\langle m \middle| \vec{L} \middle| 0 \right\rangle}{E_i^{(1)} - E_0^{(1)}} \tag{6.13}$$

we can write $E^{(2)}$ as

$$E^{(2)} = \sum_{m_S'} \left\{ \mu_B^2 \left\langle m_S \middle| \vec{B} \cdot \overset{\leftrightarrow}{\Lambda} \cdot \vec{B} \middle| m_S' \right\rangle + \lambda^2 \left\langle m_S \middle| \vec{S} \cdot \overset{\leftrightarrow}{\Lambda} \cdot \vec{S} \middle| m_S' \right\rangle + 2\lambda\mu_B \left\langle m_S \middle| \vec{B} \cdot \overset{\leftrightarrow}{\Lambda} \cdot \vec{S} \middle| m_S' \right\rangle \right\} \tag{6.14}$$

We now notice that we could write a Hamiltonian operator which would give the same matrix elements we have here, but as a first-order result. Including the electron Zeeman interaction term, we have the resulting spin Hamiltonian

$$\hat{H}_S = g_e \mu_B \vec{B} \cdot \vec{S} + \mu_B^2 \vec{B} \cdot \overset{\leftrightarrow}{\Lambda} \cdot \vec{B} + 2\lambda\mu_B \vec{B} \cdot \overset{\leftrightarrow}{\Lambda} \cdot \vec{S} + \lambda^2 \vec{S} \cdot \overset{\leftrightarrow}{\Lambda} \cdot \vec{S} \tag{6.15}$$

The term $\mu_B^2 \vec{B} \cdot \overset{\leftrightarrow}{\Lambda} \cdot \vec{B}$ is independent of spin state and so changes all levels by the same amount. Although the term would be important to the thermodynamic properties of the system, it is uninteresting to the spectroscopist and we will ignore it. The first and third terms can be combined to obtain the *g*-matrix:

$$\mathbf{g} = g_e \mathbf{E} + 2\lambda \overset{\leftrightarrow}{\Lambda} \tag{6.16}$$

where $\mathbf{E}$ is the unit matrix. For $S = 1/2$, eq (6.16) reduces to eq (5.11). We also define the fine structure matrix $\mathbf{D}$ as

$$\mathbf{D} = \lambda^2 \overset{\leftrightarrow}{\Lambda} \tag{6.17}$$

so that the spin Hamiltonian reduces to

$$\hat{H}_S = \mu_B \vec{B} \cdot \mathbf{g} \cdot \vec{S} + \vec{S} \cdot \mathbf{D} \cdot \vec{S} \tag{6.18}$$

Notice that the fine structure term found here has the same form (and the matrix is given the same symbol) as that obtained from the electron dipolar interaction. Unlike the dipolar **D**-matrix, however, the spin-orbit coupling **D**-matrix in general does not have zero trace. Nonetheless, we introduce analogous parameters:

$$D = D_{zz} - \tfrac{1}{2}\left(D_{xx} + D_{yy}\right)$$

$$E = \tfrac{1}{2}\left(D_{xx} - D_{yy}\right)$$

In the coordinate system which diagonalizes **g**, the related **D**-matrix is also diagonal. Expanding the fine structure term in the principal axis system, we h

$$\vec{\mathbf{S}} \cdot \mathbf{D} \cdot \vec{\mathbf{S}} = D_{xx}\hat{\mathbf{S}}_x^2 + D_{yy}\hat{\mathbf{S}}_y^2 + D_{zz}\hat{\mathbf{S}}_z^2$$

$$\vec{\mathbf{S}} \cdot \mathbf{D} \cdot \vec{\mathbf{S}} = D\left[\hat{\mathbf{S}}_z^2 - \tfrac{1}{3}\left(\hat{\mathbf{S}}_x^2 + \hat{\mathbf{S}}_y^2 + \hat{\mathbf{S}}_z^2\right)\right] + E\left(\hat{\mathbf{S}}_x^2 - \hat{\mathbf{S}}_y^2\right) + \tfrac{1}{3}\left(D_{xx} + D_{yy} + D_{zz}\right)\left(\hat{\mathbf{S}}_x^2 + \hat{\mathbf{S}}_y^2 + \hat{\mathbf{S}}_z^2\right)$$

Since $S^2 = S_x^2 + S_y^2 + S_z^2$, and the eigenvalue of S^2 is $S(S + 1)$, we have

$$\vec{\mathbf{S}} \cdot \mathbf{D} \cdot \vec{\mathbf{S}} = D\left[\hat{\mathbf{S}}_z^2 - \tfrac{1}{3}S(S + 1)\right] + E\left(\hat{\mathbf{S}}_x^2 - \hat{\mathbf{S}}_y^2\right) + \tfrac{1}{3}\left(D_{xx} + D_{yy} + D_{zz}\right)S(S + 1)$$

The last term (which would be zero if **D** came from the dipolar interaction and thus had zero trace) raises all levels equally and so has no effect on spectroscopy and can be dropped. Thus again only two parameters, D and E, are needed to completely specify the fine structure interaction.

Although it is unfortunate that spin-orbit coupling and the electron dipolar interaction give fine structure terms of the same form, it is possible to separate the effects. Since the spin-orbit contribution to **D** is related to the g-matrix

$$\mathbf{D}_{so} = \tfrac{\lambda}{2}\left(\mathbf{g} - g_e\mathbf{E}\right)$$

the parameters D_{so} and E_{so} can be computed

$$D_{so} = \tfrac{\lambda}{2}\left[g_{zz} - \tfrac{1}{2}\left(g_{xx} + g_{yy}\right)\right] \qquad\qquad E_{so} = \tfrac{\lambda}{4}\left(g_{xx} - g_{yy}\right)$$

The difference between the fine structure parameters computed from the experimental g-matrix and those measured from the spectrum are presumed to be the electron dipolar contributions.

In the above derivation, we have made no explicit assumption about the total electron spin quantum number S so that the results should be correct for $S = 1/2$ as well as higher values. However, the fine structure term is not usually included in spin Hamiltonians for $S = 1/2$ systems. The fine structure term can be ignored since the results of operating on a spin 1/2 wave function is always zero:

$$\left\{D\left[\hat{\mathbf{S}}_z^2 - \tfrac{1}{3}S(S + 1)\right] + \tfrac{1}{2}E\left(\hat{\mathbf{S}}_+^2 + \hat{\mathbf{S}}_-^2\right)\right\}\left|1/2,\pm1/2\right\rangle = D\left[\tfrac{1}{4} - \tfrac{1}{3}\times\tfrac{1}{2}\times\tfrac{3}{2}\right]\left|1/2,\pm1/2\right\rangle + \tfrac{1}{2}E\times0 = 0$$

High-Spin Transition Metal Ions. For axially symmetric complexes, the parameter E is zero, and the spin functions $\left|S,m_S\right\rangle$ are eigenfunctions of the spin Hamiltonian

$$\hat{\mathbf{H}}_s = \mu_B\vec{B} \cdot \mathbf{g} \cdot \vec{\mathbf{S}} + D\left[\hat{\mathbf{S}}_z^2 - \tfrac{1}{3}S(S + 1)\right]$$

Consider a d^3 Cr(III) complex in an axial ligand field with $g_{||} = 1.98$, $D = 0.0455$ cm^{-1}, $E = 0$. For the magnetic field along the molecular z-axis, the energies are

$$E(\pm \tfrac{3}{2}) = \pm \tfrac{3}{2} g_{||} \, \mu_B B + D$$

$$E(\pm \tfrac{1}{2}) = \pm \tfrac{1}{2} g_{||} \, \mu_B B - D$$

These energies are plotted *vs.* magnetic field in Figure 6.4.

Transitions among these levels have intensities proportional to the square of the matrix element of S_x. These are easily found to be

$$\left\langle \tfrac{3}{2}, \pm \tfrac{3}{2} \middle| \hat{S}_x \middle| \tfrac{3}{2}, \pm \tfrac{1}{2} \right\rangle = \frac{\sqrt{3}}{2}$$

$$\left\langle \tfrac{3}{2}, +\tfrac{1}{2} \middle| \hat{S}_x \middle| \tfrac{3}{2}, -\tfrac{1}{2} \right\rangle = 1$$
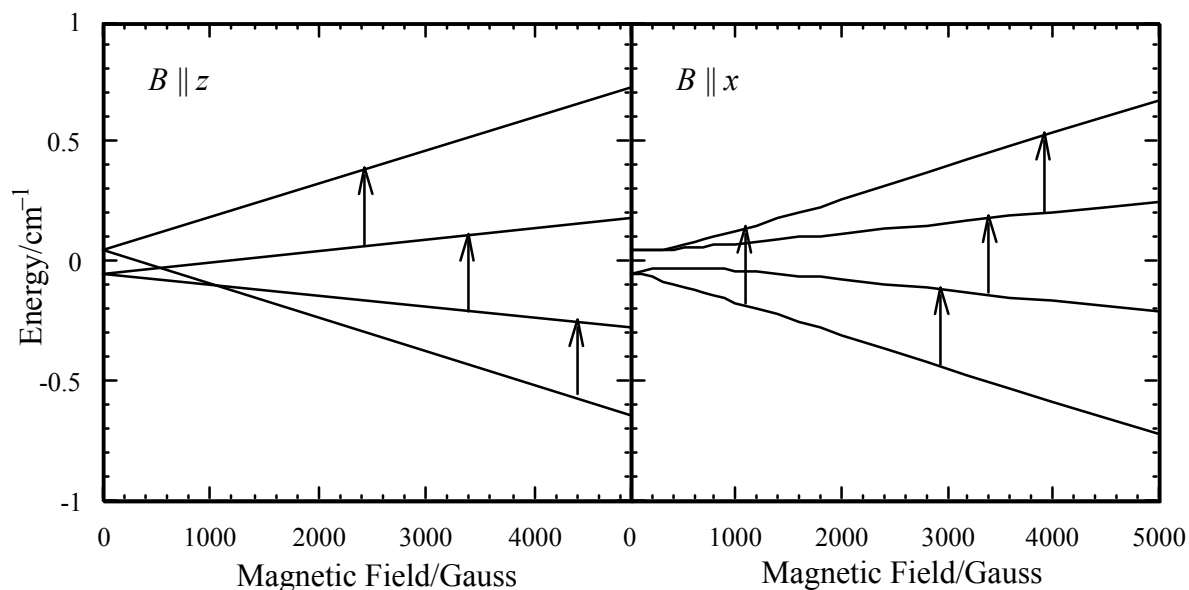
Figure 6.4. Energy levels and allowed transitions for a Cr(III) complex with $g = 1.98$, $D = 0.0455$ cm^{-1} for the magnetic field along the x- and z-axes.

Thus the $-3/2 \varnothing -1/2$ and $1/2 \varnothing 3/2$ transitions, at $B = h\nu_0(1 \pm 2D)/g\mu_B$, have relative intensities of 3/4 the intensity of the $-1/2 \varnothing 1/2$ transition, at $B = h\nu_0/g\mu_B$.

With the magnetic field oriented along the x-axis, the Hamiltonian matrix is:

$$
\begin{pmatrix}
D & \frac{\sqrt{3}}{2}g_\perp\mu_B B & 0 & 0 \\
\frac{\sqrt{3}}{2}g_\perp\mu_B B & -D & g_\perp\mu_B B & 0 \\
0 & g_\perp\mu_B B & -D & \frac{\sqrt{3}}{2}g_\perp\mu_B B \\
0 & 0 & \frac{\sqrt{3}}{2}g_\perp\mu_B B & D
\end{pmatrix}
$$

Unfortunately, the secular equation doesn't factor and the energies must be computed numerically. A plot of the computed energies is shown in Figure 6.4 as a function of field.

As we might expect from the nondiagonal Hamiltonian matrix, the spin functions are thoroughly mixed when the field is in the x-direction. The immediate consequence of this mixing is that the selection rules are complicated, and the transition from the lowest level to the highest level becomes allowed. (For the field along the z-axis, this would be a forbidden two-quantum transition.) When $B = 1000$ G, corresponding to the lowest-to-highest transition, the wave functions are:

$$E = -0.179 \text{ cm}^{-1}, \quad |1\rangle = -0.255\left(|3/2\rangle - |-3/2\rangle\right) + 0.660\left(|1/2\rangle - |-1/2\rangle\right)$$

$$E = -0.037 \text{ cm}^{-1}, \quad |2\rangle = -0.513\left(|3/2\rangle + |-3/2\rangle\right) + 0.487\left(|1/2\rangle + |-1/2\rangle\right)$$

$$E = +0.079 \text{ cm}^{-1}, \quad |3\rangle = 0.660\left(|3/2\rangle - |-3/2\rangle\right) + 0.255\left(|1/2\rangle - |-1/2\rangle\right)$$

$$E = +0.137 \text{ cm}^{-1}, \quad |4\rangle = 0.487\left(|3/2\rangle + |-3/2\rangle\right) + 0.513\left(|1/2\rangle + |-1/2\rangle\right)$$

When the field is along the x-axis, transition intensities are proportional to the square of the S_z^2 matrix element. The S_z^2-matrix for $B = 1000$ G is:

$$
\begin{pmatrix}
0 & 1.197 & 0 & 0.0011 \\
1.197 & 0 & 0.794 & 0 \\
0 & 0.794 & 0 & 0.508 \\
0.0011 & 0 & 0.508 & 0
\end{pmatrix}
$$

The 1 Ø 4 transition is only weakly allowed compared with the 1 Ø 2, 2 Ø 3, and 3 Ø 4 transitions; however it is often observed, particularly in powder spectra, because it tends to be considerably sharper than the other transitions. Notice that the 1 Ø 3 and 2 Ø 4 transitions are still forbidden. Since the wave functions are field-dependent, the S_z matrix elements also depend on the field. Thus the relative intensities of the observed 1 Ø 2, 2 Ø 3, and 3 Ø 4 transitions would be different than predicted from the S_z^2-matrix at 1000 G.

In the case of Cr(III) complexes, D is relatively small (less than the microwave quantum, ca 0.317 cm^{-1}) and all three fine structure lines are observable. This is not always the case. Consider high-spin Fe(III) in an axial ligand field with $D \gg h\nu_0$, $E = 0$. With the same Hamiltonian as above and the magnetic field along the z-axis, the energies are

$$E(\pm 5/2) = \pm \frac{5}{2} g_\parallel \mu_B B + \frac{10}{3} D$$

$$E(\pm 3/2) = \pm \frac{3}{2} g_\parallel \mu_B B - \frac{2}{3} D$$

$$E(\pm 1/2) = \pm \frac{1}{2} g_\parallel \mu_B B - \frac{8}{3} D$$

These are plotted *vs. B* in Figure 6.5.

The transition energies are

$E(5/2) - E(3/2) = g_\parallel \mu_B B + 4 D$

$E(3/2) - E(1/2) = g_\parallel \mu_B B + 2 D$

$E(1/2) - E(-1/2) = g_\parallel \mu_B B$

$E(-1/2) - E(-3/2) = g_\parallel \mu_B B - 2 D$

$E(-3/2) - E(-5/2) = g_\parallel \mu_B B - 4 D$

However, if $D > h\nu_0$, only the $-1/2 \oslash 1/2$ transition will be observable. The first two transitions are always higher in energy than $h\nu_0$ and the it is usually not possible to make B large enough to bring the last two transitions into resonance.

Now consider what happens when the field is applied perpendicular to the symmetry axis. The large value of D ensures that z will continue to be the quantization axis. The Hamiltonian matrix is
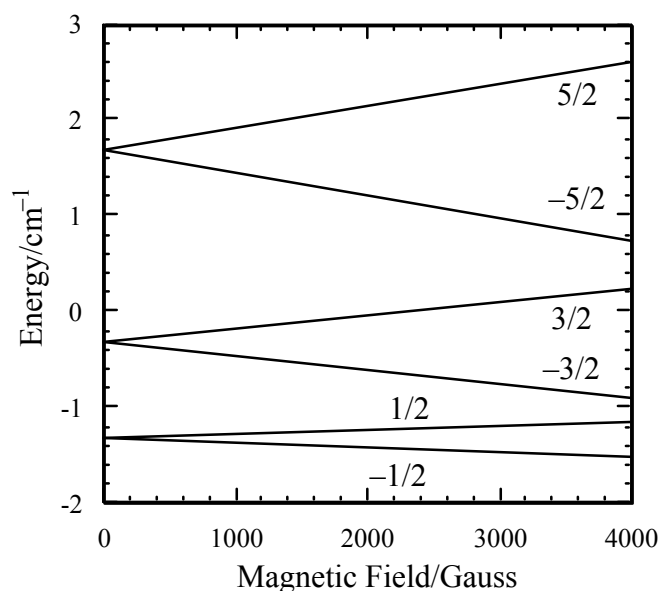
Figure 6.5. Energies of an $S = 5/2$ spin system with $D = 0.5$ cm^{-1} for B along the z-axis.

$$
\begin{pmatrix}
\frac{10}{3}D & \sqrt{5}\,g_{\perp}\mu_B B & 0 & 0 & 0 & 0 \\
\sqrt{5}\,g_{\perp}\mu_B B & -\frac{2}{3}D & \sqrt{2}\,g_{\perp}\mu_B B & 0 & 0 & 0 \\
0 & \sqrt{2}\,g_{\perp}\mu_B B & -\frac{8}{3}D & \frac{3}{2}g_{\perp}\mu_B B & 0 & 0 \\
0 & 0 & \frac{3}{2}g_{\perp}\mu_B B & -\frac{8}{3}D & \sqrt{2}\,g_{\perp}\mu_B B & 0 \\
0 & 0 & 0 & \sqrt{2}\,g_{\perp}\mu_B B & -\frac{2}{3}D & \sqrt{5}\,g_{\perp}\mu_B B \\
0 & 0 & 0 & 0 & \sqrt{5}\,g_{\perp}\mu_B B & \frac{10}{3}D
\end{pmatrix}
$$

We ought to solve a 6∞6 secular equation, but we can get a reasonable approximation more easily. Since D is big, the ±5/2 and ±3/2 levels are well separated from the ±1/2 levels before application of the magnetic field. Thus mixing of $|3/2\rangle$ with $|1/2\rangle$ will be much less important than mixing of $|1/2\rangle$ with $|-1/2\rangle$. Thus we can solve just the middle 2∞2 block for the energies of the $m_S = \pm 1/2$ levels. The expanded block gives:

$$
\left(-\frac{8}{3}D - E\right)^2 - \left(\frac{3}{2}g_{\perp}\mu_B B\right)^2 = 0
$$

so that the energies are

$$
E = -\frac{8}{3}D \pm \frac{3}{2}\,g_{\perp}\mu_B B
$$

and the energy difference is

$$
E(1/2) - E(-1/2) = 3\,g_{\perp}\mu_B B
$$

The apparent g-value for the transition is $3g_{\perp}$, $g_{\text{eff}} = 6$ if $g_{\perp} = 2$.

Thus high-spin d^5 Fe(III) in an axial ligand field should show a resonance around $g = 2$ when B is along the symmetry axis and a resonance near $g = 6$ when B is perpendicular to the symmetry axis. In solution, where the complex tumbles rapidly and averages the g-values, the resonance is expected to be so broad as to be undetectable.

References

1. A. Hudson, Electron Spin Resonance, 1988,11A , 55-76.

2. P. B. Ayscough, Electron Spin Resonance in Chemistry, Methuen, London, 1967.

3. P. W. Atkins and M. C. R. Symons, The Structure of Inorganic Radicals, Elsevier, Amsterdam, 1967.

4. A. Abragam and B. Bleaney, Electron Paramagnetic Resonance of Transition Ions, Clarendon Press, Oxford, 1970.

5. J. E. Wertz and J. E. Bolton, Electron Spin Resonance, McGraw-Hill, New York, 1972.

6. N. M. Atherton, Electron Spin Resonance, Ellis Horwood, Chicester, 1973.

7. W. Gordy, Theory and Applications of Electron Spin Resonance, Wiley, New York, 1980.

8. J. R. Pilbrow, Transition Ion Electron Paramagnetic Resonance, Clarendon Press, Oxfor, 1990.

9. F. E. Mabbs and D. Collison, Electron Paramagnetic Resonance of d Transition Metal Compounds, Elsevier, Amsterdam, 1992.

10. G. Breit and I. I. Rabi, Phys. Rev. 1931, 38, 2082-2083.

11. S. I. Weissman, J. Townsend, G. E. Paul, and G. E. Pake, J. Chem. Phys. 1953, 21, 2227.

12. L. V. Casagrande, T. Chen, P. H. Rieger, B. H. Robinson, J. Simpson, and S. J. Visco, Inorg. Chem. 1985, 23, 2019-2025.

13. B. M. Peake, P. H. Rieger, B. H. Robinson, and J. Simpson, Inorg. Chem. 1979,18, 1000-1005.

14. A. R. Boate, J. R. Morton, and K. F. Preston, J. Mag. Reson. 1976, 24, 259-268.

15. R. W. Fessenden and R. H. Schuler, J. Chem. Phys. 1963, 39, 2147.

16. M. Karplus and G. K. Fraenkel, J. Chem. Phys. 1961, 35, 1312.

17. R. Wilson and D. Kivelson, J. Chem. Phys. 1966, 44, 154; P. W. Atkins and D. Kivelson, J. Chem. Phys. 1966, 44, 169.

18. G. K. Fraenkel, J. Phys. Chem. 1967, 71, 139-171.

19. W. B. Lewis and L. O. Morgan, in R. L. Carlin (Ed.), Transition Met. Chem., Vol. 4, Marcel Dekker, New York, 1968, pp. 33-112.

20. B. H. Robinson and A. H. Beth, Electron Spin Resonance 1983,8, 346-377.

21. M. M. Iannuzzi and P. H. Rieger, Inorg. Chem. 1975,14, 2895-2899.

22. M. M. Iannuzzi, C. P. Kubiak, and P. H. Rieger, J. Phys. Chem. 1976,80, 541-545.

23. R. L. Ward and S. I. Weissman, J. Am. Chem. Soc. 1957,79, 2086-2090.

24. B. J. Corden and P. H. Rieger, Inorg. Chem. 1971,10, 263-272.

25. H. S. Gutowsky, D. W. McCall, and C. P. Slichter, J. Chem. Phys. 1953, 21, 279-292. See also reference 6, pp 309-313.

26. J. I. Kaplan, J. Chem. Phys. 1958, 28, 278-282; 1958, 29, 462; S. Alexander, ibid. 1962, 37, 967-974, 974-980. See also reference 6, pp 313-323.

27. See also reference 6, pp 323-327.

28. N. W. Duffy, R. R. Nelson, M. G. Richmond, A. L. Rieger, P. H. Rieger, B. H. Robinson, D. R. Tyler, J. C. Wang and K. Yang, *Inorg. Chem.* **1998**, *37*, 4849.

29. J. A. DeGray, Q. Meng, and P. H. Rieger, J. Chem. Soc. Faraday I 1987, 83, 3565-3573.

30. N. V. Vugman, A. O. Caride, and J. Danon, J. Chem. Phys. 1973, 59, 4418-4422.

31. N. V. Vugman and N. M. Pinhal, Mol. Phys. 1983,49, 1315-1319.

32. J. A. DeGray, P. H. Rieger, N. G. Connelly and G. Garcia, J. Magn. Reson., 1990, 88, 376.

33. P. H. Rieger, *J. Magn. Reson.* **1982**, *50*, 485-489.

34. M. C. R. Symons, J. R. Morton, and K. F. Preston, in K. S. Suslick (Ed.), *High-Energy Processes in Organometallic Chemistry*, American Chemical Society, Washington, DC, 1987, pp. 169-190.

35. P. C. Taylor, J. F. Baugher, and H. M. Kriz, *Chem. Rev.* **1975**, *75*, 203-240.

36. I. V. Ovchinnikov and V. N. Konstantinov, *J. Magn. Reson.* **1978**, *32,* 179-190.

37. P. C. Taylor and P. J. Bray, *J. Magn. Reson.* **1970**, *2*, 305-331.

38. J. A. DeGray and P. H. Rieger, *Bull. Magn. Reson.* **1987**, *8*, 95-101.

39. B. A. Goodman and J. B. Raynor, *Adv. Inorg. Chem. Radiochem.* **1971**, *13*, 136-362.

40. J. R. Morton and K .F. Preston, *J. Mag. Reson.* **1978**, *30*, 577-582.

41. A. K. Koh and D. J. Miller, *Atom. Data Nucl. Data Tab.* **1985**, *33*, 235-253.

42. P. H. Rieger, *J. Mag. Reson.* **1997**, *124*, 140.

43. B. M. Peake, P. H. Rieger, B. H. Robinson, and J. Simpson, *J. Am. Chem. Soc.* **1980**, *102*, 156-163.

44. N. G. Connelly, W. E. Geiger, G. A. Lane, S. J. Raven, and P. H. Rieger, J. Am. Chem. Soc. 1986,108, 6219-6224.

45. B. R. McGarvey, in T. F. Yen (Ed.), *Electron Spin Resonance of Metal Complexes*, Plenum Press, New York, 1969, pp. 1-11.

46. A. F. Stone, *Proc. Roy. Soc. (London)* **1963**, *A271*, 424-434.

47. T. Kawamura, K. Fukamachi, T. Sowa, S. Hayashide, and T. Yonezawa, *J. Am. Chem. Soc.* **1981**, *103*, 364-369.

48. G. A. Carriedo, V. Riera, N. G. Connelly, and S. J. Raven, *J. Chem. Soc., Dalton Trans.* **1987**, 1769-1773.

49. G. A. Carriedo, N. G. Connelly, E. Perez-Carreno, A. G. Orpen, A. L. Rieger, P. H. Rieger, V. Riera, and G. M. Rosair, *J. Chem. Soc., Dalton Trans.*, **1993**, 3103.

50. T. A. Albright, W. E. Geiger, J. Moraczweski, and B. Tulyathan, *J. Am. Chem. Soc.* **1981**, *103*, 4787-4794.

51. T. A. Albright and R. Hoffmann, *Chem. Ber.* **1978**, *111,* 1578-1590.

52. J. R. Pilbrow and M. R. Lowrey, *Rep. Prog. Phys.* **1980**, *43*, 433-495.

53. F. K. Kneubühl, *Phys. Kondens. Mat.* **1963**, *1*, 410-447; **1965**, *4*, 50-62.

54.   For a summary of Kneubühl's methods, see reference 52.

55. W. E. Geiger, P. H. Rieger, B. Tulyathan, and M. C. Rausch, *J. Am. Chem. Soc.* **1984**, *106*, 7000-7006.

56. T. Lionel, J. R. Morton, and K. F. Preston, *J. Chem. Phys.* **1982**, *76*, 234-239.

57. S. A. Fairhurst, J. R. Morton, and K. F. Preston, *J. Chem. Phys.* **1982**, *77*, 5872-5875.

58. D. J. Hammack, M. M. Dillard, M. P. Castellani, A. L. Rheingold, A. L. Rieger and P. H. Rieger,*Organometallics*, **1996**, *15*, 4791.

59. B. M. Peake, P. H. Rieger, B. H. Robinson, and J. Simpson, *J. Am. Chem. Soc.* **1980**, *102*, 156.

60. B. M. Peake, P. H. Rieger, B. H. Robinson, and J. Simpson, *Inorg. Chem.* **1981**, *20*, 2540.

61. F. A. Cotton, J. D. Jamerson, and B. R. Stults, *J. Am. Chem. Soc.* **1976**, *98*, 1774-1779.

62.   C. G. Howard, G. S. Girolami, G. Wilkinson, M. Thornton-Pett, and M. B. Hursthouse, *J. Chem. Soc., Dalton Trans.* **1983**, 2631-2637.

Problems

1.   The tetramethylammonium salt of the 1,1,2,3,3-pentacyanopropenyl anion, $[(NC)_2C\text{-}C(CN)=C(CN)_2]^-$, was reduced electrochemically at room temperature in N,N-dimethylformamide solution containing tetramethylammonium perchlorate as a supporting electrolyte. When the reduction was at the potential of the first polarographic wave, ESR spectrum (a), shown below, was observed. When the potential was changed to that of the second reduction wave, however, spectrum (b) was observed.
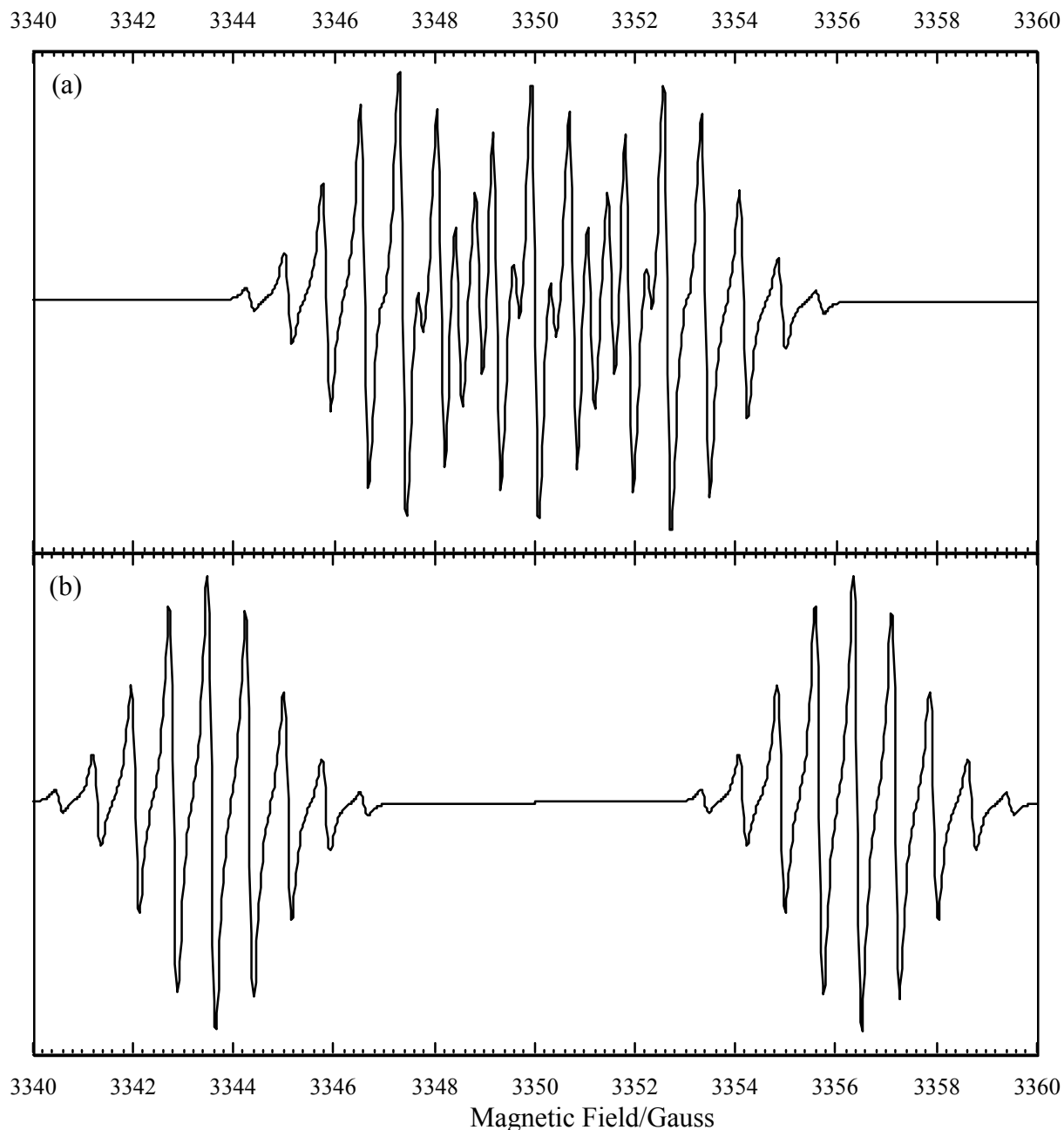
(a) Determine the number, spin and coupling constants of nuclei interacting with the unpaired electron. What can you guess about the chemistry of this system given your interpretation of the ESR spectra (*i.e.*, what are the two radicals and how did they arise?)

(b) Consider the allyl anion, $[H_2C–CH=CH_2]^-$, as a model for the electronic structure of the cyanocarbon anions. Simple Hückel MO theory predicts three p energy levels:

$$E_1 = \alpha + \sqrt{2}\beta \quad \Psi_1 = \frac{1}{2}\left(\phi_1 + \phi_3 + \sqrt{2}\,\phi_2\right)$$

$$E_2 = \alpha \quad \Psi_2 = \frac{1}{\sqrt{2}}\left(\phi_1 - \phi_3\right)$$

$$E_3 = \alpha - \sqrt{2}\beta \quad \Psi_3 = \frac{1}{2}\left(\phi_1 + \phi_3 - \sqrt{2}\,\phi_2\right)$$

Is this simple theoretical prediction consistent with the ESR results? Explain.

2. The PO_3^{2-} radical, produced by γ-irradiation of $Na_2HPO_3.5H_2O$ crystals, gives an axially symmetric ESR spectrum with $g_{||} = 1.999$, $g_\perp = 2.001$ and a ^{31}P coupling matrix with $a_{||} = 699$ G, $a_\perp = 540$ G. For an electron in a phosphorus 3s orbital, one expects a coupling constant of 3664 G; for an electron in a phosphorus 3p orbital, the dipolar coupling parameter is $P = 251.8$ G.

(**a**) The signs of the experimental couplings are indeterminate. What combination of signs makes physical sense?

(**b**) Compute the phosphorus 3p contribution and the minimum and maximum 3s contribution to the MO containing the odd electron. What is the minimum and maximum spin density on each oxygen?

3. The radical anion $[PhCCo_3(CO)_9]^-$, obtained by reduction of the neutral cluster in THF solution, gives a 22-line isotropic spectrum (see Figure 4.3) with $\langle g \rangle = 2.013$, $\langle A^{Co} \rangle = 33.6 \times 10^{-4}$ cm^{-1}. From analysis of the line shapes, it is clear that the three cobalt nuclei are magnetically equivalent (cobalt is 100% ^{59}Co, $I = 7/2$). The frozen solution gives a spectrum which shows well-resolved parallel features, $g_{||} = 1.996$, $A_{||} = 73.6 \times 10^{-4}$ cm^{-1}. The perpendicular features of the spectrum are not resolved; the linewidths could hide a perpendicular coupling of as much as 20×10^{-4} cm^{-1}.

(**a**) The signs of $\langle A \rangle$ and $A_{||}$ are experimentally indeterminate. However, the small magnitude of $A_\perp$ and the relationship, $\langle A \rangle = (A_{||} + 2A_\perp)/3$, imposes some limitations. What signed values for $\langle A \rangle$, $A_{||}$, and $A_\perp$ are consistent with the experimental data?

(**b**) Assuming that the molecular symmetry is $\mathbf{C_{3v}}$, use the symmetry restrictions summarized in Table 5 and the accompanying discussion to determine the orientation of the principal axes of the g-matrix. What restrictions are imposed by symmetry on the orientations of the hyperfine matrix principal axes? (Strictly speaking, the phenyl group reduces the symmetry to $\mathbf{C_s}$ or less; however, virtually identical spectra are obtained when -Ph is replaced by -CH_3 so it seems safe to ignore the substituent.)

(**c**) The parallel features of the frozen solution spectrum are equally spaced within experimental error. This suggests that the three cobalt nuclear hyperfine matrixs have the corresponding axis in common. What must be the orientation of this common axis?

(**d**) Consider the following local axes for the three cobalt atoms: let the x-axes be normal to the reflection planes, the z-axes be directed toward the center of the tricobalt plane, and the y-axes be parallel to the three-fold molecular axis. Now

consider the five 3d and one 4s orbitals of the three cobalt atoms. Which irreducible representations are spanned by these 18 atomic orbitals? Write the symmetry-adapted combinations for the one-dimensional representations.

(**e**) The unpaired electron in the tricobalt carbon radical anion most likely occupies a nondegenerate molecular orbital. A Jahn-Teller distortion would be expected if the odd electron were in an orbital of **e** symmetry, leading to instantaneously nonequivalent cobalt nuclei. Which of the SALC's found in part (**d**) is consistent with the experimental results? HINT: Which of the atomic orbitals is expected to give an electron-nuclear dipolar coupling with the major axis oriented as found in part (**c**)?

(**f**) Given that the dipolar coupling parameter for ^{59}Co is $P = 282 \infty 10^{-4}$ cm^{-1}, compute the 3d-electron spin density for each cobalt atom. What is the origin of the isotropic coupling? Is it due to 4s spin density or to polarization of inner-shell s orbitals by spin density in the 3d shell?

4. The ESR spectrum of Xe$_2^+$ was reported by Stein, Norris, Downs, and Minihan (*J. Chem. Soc., Chem. Commun.* **1978**, 502). The ground state of Xe$_2^+$ is thought to be $^2\Sigma_u^+$. The isoelectronic I$_2^-$ has been detected in x-irradiated single crystals of PH$_4$I [Marquardt, *J. Chem. Phys.* **1968**, *48* , 994] and the corresponding F$_2^-$, Cl$_2^-$, and Br$_2^-$ have been known for some time as the so-called V$_k$ color centers in alkali halide crystals. The ESR spectra of these have been recorded and the g- and hyperfine matrix parameters are listed below along with those for Xe$_2^+$.

Species	$g_{\parallel}$	$g_{\perp}$	$A_{\parallel}$/cm^{-1}	$A_{\perp}$/cm^{-1}
F$_2^-$	2.0020	2.0218	0.0849	0.0026
Cl$_2^-$	2.0012	2.0426	0.0095	0.0012
Br$_2^-$	1.9833	2.169	0.0417	0.0080
I$_2^-$	1.901	2.28	0.0323	0.0078
Xe$_2^+$	1.885	2.304	0.0528	0.0237

Spin-orbit coupling results in admixture of some p$_u$ character into the σ_u MO. By including this effect to second-order in perturbation theory, Inue, *et al.*, showed that the g-matrix components are approximately

$$g_{\parallel} = g_e - (\lambda/\Delta)^2$$

$$g_{\perp} = g_e - 2\lambda/\Delta - 2(\lambda/\Delta)^2$$

where λ is the spin-orbit coupling parameter and Δ is the first-order energy separation between the σ_u and p$_u$ MO's. Extending this calculation, Schoemaker found that the hyperfine components could be written as

$$A_{\parallel} = A_0 + (4/5)P\rho_p$$

$$A_{\perp} = A_0 - (2/5)P\rho_p + P(g_{\perp} - g_e)$$

The first term in the expressions corresponds to the Fermi contact contribution, the second to electron-nuclear dipolar coupling, and the third results from an indirect

contribution of spin-orbit coupling. In these equations, ρ_p is the np_z spin density on one of the atoms and

$$P = g_e g_N \mu_B \mu_N \langle r^{-3} \rangle$$

includes the relevant constants and a measure of the size of the p-orbital. The Fermi contact term, A_0, has two components, a spin polarization part proportional to the p-spin density—the proportionality constants Q_x are unknown but are probably negative—and a direct contribution due to s-orbital character in the σ_u MO:

$$A_0 = Q_x \rho_p + A_s \rho_s$$

The parameters P and A_s, (averages over the naturally occuring isotopes for Cl and Br), together with the spin-orbit coupling parameter ζ, are given in the following table:

	F	Cl	Br	I	Xe
P/cm^{-1}	0.1468	0.0140	0.0708	0.0677	0.1117
A_s/cm^{-1}	1.76	0.183	1.11	1.39	2.26
ζ/cm^{-1}	269	587	2456	5068	

(a) Use the g-matrix components to estimate λ/Δ for F_2^-, Cl_2^-, Br_2^-, I_2^-, and Xe_2^+. The equations are correct only to second-order in perturbation theory and are expected to break down as λ/Δ increases, so don't expect an exact fit. Discuss the sign of λ/Δ and the trend in λ/Δ for the series, including the difference between the values found for the isoelectronic I_2^- and Xe_2^+.

(b) Use the hyperfine matrix components (assume all values are positive) and the values of P to estimate the np_z contributions to the semi-occupied molecular orbitals in F_2^- – Xe_2^+. Discuss the results; are they consistent with your expectations from simple MO theory? Note that P is computed from approximate atomic orbitals and thus is at best a rough estimate in a molecular context; thus don't worry about small differences in ρ_p (less than ca. 10%).

(c) Assuming that the polarization contributions to the Fermi contact interaction can be neglected, use the values of A_s to estimate the ns contribution to the SOMO. If the Q_x were significant and negative, would your estimates of ρ_s be too big or too small? Are the results consistent with your qualitative expectations from simple MO theory?

5. The ESR spectrum of *trans*-[Cr(CO)$_2$(dppm)$_2$]$^+$, dppm = Ph$_2$PCH$_2$PPh$_2$, in CH$_2$Cl$_2$/C$_2$H$_4$Cl$_2$ at 120 K is shown below. The microwave frequency was 9.4509 GHz. Note that the spectrum is only approximately axial.

(a) Determine the ESR parameters, g_1, g_2, g_3, A_1, A_2, and A_3 (hyperfine coupling to ^{31}P).

(b) The isotropic spectrum of *trans*-[Cr(CO)$_2$(dppm)$_2$]$^+$ in the same solvent is a simple 1:4:6:4:1 quintet with •g® = 2.004, •A^P® = 25.8 ∞ 10^{-4} cm^{-1}. What can you conclude about the relataive signs of the components of the hyperfine matrix? How large and well established are the dipolar hyperfine matrix components? Given the

value of P for ^{31}P (Appendix 1 below), what can you conclude about the extent of delocalization of the unpaired electron into phosphorus p-orbitals?
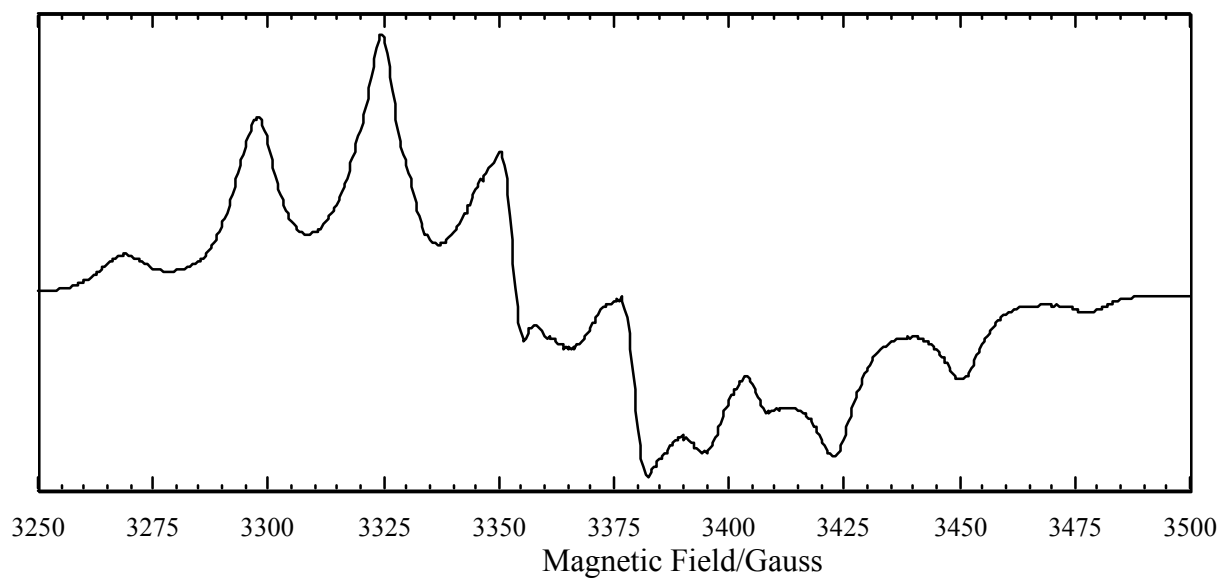
Appendix 1. Some Properties of Magnetic Nuclei*

Nucleus	Spin	% Abund.	A_s	P	μ	Q
^{1}H	1/2	99.985	473.8		2.7928	0
^{2}H	1	0.015	72.5		0.8574	0.00286
^{6}Li	1	7.5	30.7		0.8220	−0.0008
^{7}Li	3/2	92.5	121.7		3.2564	−0.041
^{9}Be	3/2	100.0	−150.6		−1.1776	0.053
^{10}B	3	19.9	569.	35.5	1.8006	0.085
^{11}B	3/2	80.1	850.	53.1	2.6886	0.041
^{13}C	1/2	1.11	1260	89.6	0.7024	0
^{14}N	1	99.63	604	46.3	0.40387	0.020
^{15}N	1/2	0.37	−424	−32.5	−0.2832	0
^{17}O	5/2	0.038	−1756	−140.4	−1.8938	−0.026
^{19}F	1/2	100.0	17635	1468	2.6289	0
^{23}Na	3/2	100.0	309.2		2.2175	0.101
^{25}Mg	5/2	10.0	−162.1		−0.8554	0.199
^{27}Al	5/2	100.0	1304	69.3	3.6415	0.15
^{29}Si	1/2	4.67	−1532	−95.2	−0.5553	0
^{31}P	1/2	100.0	4438	305.9	1.1316	0
^{33}S	3/2	0.75	1155	83.8	0.6438	−0.07
^{35}Cl	3/2	75.77	1909	146.4	0.8219	−0.08
^{37}Cl	3/2	24.23	1589	121.8	1.2855	−0.018
^{39}K	3/2	93.26	76.2		0.3915	0.049
^{41}K	3/2	6.73	41.8		0.2149	0.060
^{43}Ca	7/2	0.135	−213.7		−1.3173	−0.05
^{45}Sc	7/2	100.0	942.	80.2	4.7565	−0.22
^{47}Ti	5/2	7.44	−261	−24.56	−0.7885	0.30
^{49}Ti	7/2	5.41	−365	−34.39	−1.1042	0.24
^{51}V	7/2	99.75	1389	146.0	5.1487	−0.04
^{53}Cr	3/2	9.50	−249.5	−34.36	0.4745	−0.15
^{55}Mn	5/2	100.0	1680.	207.5	3.4687	0.32
^{57}Fe	1/2	2.12	249.2	32.6	0.0906	0

* A_s and P in units of 10^{-4} cm^{-1}; μ in units of nm, Q in units of 10^{-28} m^2

Nucleus	Spin	% Abund.	A_s	P	μ	Q
^{59}Co	7/2	100.0	1984	282.0	4.63	0.41
^{61}Ni	3/2	1.14	−0.08336	−0.01253	−0.7500	0.16
^{63}Cu	3/2	69.17	2000.	399.	2.2233	−0.211
^{65}Cu	3/2	30.83	2142.	428.	2.3817	−0.195
^{67}Zn	5/2	4.1	696.	117.3	0.8755	0.15
^{69}Ga	3/2	60.11	4073.	170.0	2.0166	0.17
^{71}Ga	3/2	39.89	5175.	216.0	2.5623	0.11
^{73}Ge	9/2	7.73	−788.	−40.1	0.8795	−0.17
^{75}As	3/2	100.0	4890.	278.2	1.4395	0.31
^{77}Se	1/2	7.63	6711.	410.	0.5351	0
^{79}Br	3/2	50.69	10697.	682.	2.1064	0.331
^{81}Br	3/2	49.31	11531.	734.	2.2706	0.276
^{85}Rb	5/2	72.16	346		1.353	0.23
^{87}Rb	3/2	27.83	703		2.7512	—
^{87}Sr	9/2	7.00	−584.7		1.0936	0.34
^{89}Y	1/2	100.0	−417	−20.76	−0.1374	0
^{91}Zr	5/2	11.22	−918	−51.9	−1.3036	−0.21
^{93}Nb	9/2	100.0	2198	152.5	6.1705	−0.32
^{95}Mo	5/2	15.92	−662	−50.3	−0.9141	−0.02
^{97}Mo	5/2	9.55	−676	−51.3	0.9335	0.26
^{99}Ru	12.7	5/2	−525	−47.5	−0.6413	0.079
^{101}Ru	17.0	5/2	−588	−53.3	−0.7188	0.46
^{103}Rh	100.0	1/2	−410.	−40.4	−0.0884	0
^{105}Pd	22.33	5/2		−62.7	−0.642	0.66
^{107}Ag	51.84	1/2	−611.	−68.3	−0.1136	0
^{109}Ag	48.16	1/2	−702.	−78.6	−0.1306	0
^{111}Cd	12.80	1/2	−4553.	−430.	−0.5949	0
^{113}Cd	12.22	1/2	−4763	−450	−0.6223	0
^{113}In	4.29	9/2	6731	237.1	5.529	0.80
^{115}In	95.71	9/2	6746	237.6	5.521	0.81

Nucleus	Spin	% Abund.	A_s	P	μ	Q
^{117}Sn	7.68	1/2	−14002.	−584.	−1.0010	0
^{119}Sn	8.58	1/2	−14650.	−611.	1.0473	0
^{121}Sb	57.21	5/2	11708.	524.	3.363	−0.4
^{123}Sb	42.79	7/2	8878.	398.	2.550	−0.5
^{125}Te	7.14	1/2	−18542.	−875.	−0.8885	0
^{127}I	100.0	5/2	13876.	677.	2.8133	−0.79
^{133}Cs	100.0	7/2	823.		2.582	−0.0037
^{135}Ba	6.59	3/2	1220.		0.838	0.16
^{137}Ba	11.23	3/2	1324.		0.9374	0.245
^{139}La	99.91	7/2	2004.	79.1	—	—
^{177}Hf	18.61	7/2	1471.	41.4	0.7935	0.337
^{179}Hf	13.63	9/2	−1188.	−33.4	−0.6409	3.79
^{181}Ta	99.99	7/2	5010.	148.6	2.370	3.3
^{183}W	14.31	1/2	1927.	60.9	0.1178	0
^{185}Re	37.40	5/2	11959.	390.	3.1871	2.18
^{187}Re	62.60	5/2	11838.	386.	3.2197	2.07
^{187}Os	1.6	1/2	431.	14.7	0.0646	0
^{189}Os	16.1	3/2	4403.	150.4	0.6599	0.86
^{191}Ir	37.3	3/2	1072.	37.7	0.151	0.82
^{183}Ir	62.7	3/2	1165.	41.0	0.164	0.75
^{195}Pt	33.8	1/2	11478.	492.	0.6095	0
^{197}Au	100.0	3/2	959.	44.0	0.1458	0.55
^{199}Hg	16.9	1/2	13969.	537.	0.5059	0
^{201}Hg	13.2	3/2	−15469.	−595.	−0.5602	0.39
^{203}Tl	29.52	1/2	60712.	1040.	1.6223	0
^{205}Tl	70.48	1/2	61308.	1051.	1.6382	0
^{207}Pb	22.1	1/2	27188.	542.	0.5926	0
^{209}Bi	100.0	9/2	56860.	553.	4.111	−0.37

Appendix 2. The Bloch Equations

The phenomenological equations proposed by Felix Bloch in 1946 have had a profound effect on the development of magnetic resonance, both ESR and NMR, on the ways in which the experiments are described (particularly in NMR), and on the analysis of linewidths and saturation behavior. In this appendix, we will describe the phenomenological model, derive the Bloch equations and solve them for steady-state conditions. We will also show how the Bloch equations can be extended to treat inter- and intramolecular exchange phenomena.

The Phenomenological Model

When a magnetic field is applied to an electron or nuclear spin, the spin quantization axis is defined by the field direction. Spins aligned with the field are only slightly lower in energy than those aligned opposed to the field. If we consider an ensemble of spins, the vector sum of all the spin magnetic moments will be a non-zero net magnetic moment or macroscopic magnetization:

$$\vec{\mathbf{M}} = \sum_i \vec{\mu}_i$$

(A2.1)

At equilibrium, $\vec{\mathbf{M}}$ is in the direction of the field $\vec{\mathbf{B}}$. If somehow $\vec{\mathbf{M}}$ is tilted away from $\mathbf{B}$, there will be a torque which causes $\mathbf{M}$ to precess about $\mathbf{B}$ with the equation of motion

$$\frac{d\vec{\mathbf{M}}}{dt} = \gamma\vec{\mathbf{B}} \times \vec{\mathbf{M}}$$

(A2.2)

where $\gamma = 2\pi g\mu_B/h$ (or $2\pi g_N\mu_N/h$). In addition to the precessional motion, there are two relaxation effects.

If M_0 is the equilibrium magnetization along $\vec{\mathbf{B}}$ and M_z is the z-component under nonequilibrium conditions, then we assume that M_z approaches M_0 with first-order kinetics:

$$\frac{dM_z}{dt} = \frac{M_0 - M_z}{T_1}$$

(A2.3)

where T_1 is the characteristic time for approach to equilibrium (the reciprocal of the rate constant). Since this process involves transfer of energy from the spin system to the surroundings (conventionally called the "lattice"), T_1 is called the ***spin-lattice relaxation time***. Since electrons are much more closely coupled to molecular interactions than are nuclei (which are buried in a sea of inner-shell electrons), it is not surprising that T_1 for electrons is usually much shorter (on the order of microseconds) than are nuclear T_1's (on the order of seconds).

There is a second kind of relaxation process which is at least as important for magnetic resonance as the T_1 process. Suppose that $\vec{\mathbf{M}}$ is somehow tilted down

from the z-axis toward the x-axis and the precessional motion is started. Each individual magnetic moment undergoes this precessional motion, but the individual spins may precess at slightly different rates. Local shielding may cause small variations in B or the effective g-factor may vary slightly through the sample. Thus an ensemble of spins which all start out in phase will gradually lose phase coherence—the individual spins will get out of step. We assume that there is a characteristic time for this process, called the ***transverse relaxation time***, T_2, and that the transverse magnetization components decay accordingly:

$$\frac{dM_x}{dt} = -\frac{M_x}{T_2} \qquad \frac{dM_y}{dt} = -\frac{M_y}{T_2} \qquad \text{(A3.4)}$$

Notice that dephasing of the transverse magnetization does not effect M_z; a T_2 process involves no energy transfer but does involve an increase in the entropy of the spin system.

You may have noticed that a T_1 process, in which M_z approaches M_0, necessarily causes M_x and M_y to approach zero. Thus, strictly speaking, the T_2 of eq (A2.4) must include the effects of spin-lattice relaxation as well as the dephasing of the transverse magnetization. Transverse relaxation is often faster than spin-lattice relaxation and T_2 is then determined mostly by spin dephasing. In general, however, we should write

$$\frac{1}{T_2} = \frac{1}{T_1} + \frac{1}{T_2'} \qquad \text{(A2.5)}$$

where T_2' is the spin dephasing relaxation time, and T_2 is the effective transverse relaxation time.

In ESR, it is also customary to classify relaxation effects by their effects on electron and nuclear spins. A process which involves an electron spin flip necessarily involves energy transfer to or from the lattice and is therefore a contribution to T_1; we call such a process ***nonsecular***. A process which involves no spin flips, but which results in loss of phase coherence is termed ***secular***. Processes which involve nuclear spin flips but not electron spin flips are strictly nonsecular, but because the energy transferred is so small (compared with electron spin flips), these processes are termed ***pseudosecular***.

Derivation of the Bloch Equations

Combining eqs (A2.2), (A2.3) and (A2.4), we have

$$\frac{d\vec{M}}{dt} = \gamma\vec{B}\times\vec{M} - \hat{i}\frac{M_x}{T_2} - \hat{j}\frac{M_y}{T_2} + \hat{k}\frac{M_0 - M_z}{T_1} \qquad \text{(A2.6)}$$

In a magnetic resonance experiment, we apply not only a static field B_0 in the z-direction but an oscillating radiation field B_1 in the xy-plane, so that the total field is

$$\vec{B} = \hat{i}B_1\cos\omega t + \hat{j}B_1\sin\omega t + \hat{k}B_0 \qquad \text{(A2.7)}$$

The vector product of eq (A2.6) then becomes:

$$\vec{\mathbf{B}} \times \vec{\mathbf{M}} = -\hat{\boldsymbol{i}}\left[B_0 M_y - B_1 M_z \sin \omega t\right] + \hat{\boldsymbol{j}}\left[B_0 M_x - B_1 M_z \cos \omega t\right]$$
$$+ \hat{\boldsymbol{k}} B_1\left[M_y \cos \omega t - M_x \sin \omega t\right]$$

Inserting this expression in eq (A2.6) and separating it into components, we get

$$\frac{dM_x}{dt} = -\gamma B_0 M_y + \gamma B_1 M_z \sin \omega t - \frac{M_x}{T_2} \quad \text{(A2.8a)}$$

$$\frac{dM_y}{dt} = \gamma B_0 M_x - \gamma B_1 M_z \cos \omega t - \frac{M_y}{T_2} \quad \text{(A2.8b)}$$

$$\frac{dM_z}{dt} = \gamma B_1\left[M_y \cos \omega t - M_x \sin \omega t\right] + \frac{M_0 - M_z}{T_1}$$

$$\text{(A2.8c)}$$

It is convenient to write M_x and M_y as

$$M_x = u \cos \omega t + v \sin \omega t \qquad \text{(A2.9a)}$$

$$M_y = u \sin \omega t - v \cos \omega t \qquad \text{(A2.9b)}$$

or $\quad u = M_x \cos \omega t + M_y \sin \omega t \qquad \text{(A2.10a)}$

$$v = M_x \sin \omega t - M_y \cos \omega t \qquad \text{(A2.10b)}$$

This is equivalent to transformation to a coordinate system which rotates with the oscillating field; u is that part of M_x which is in-phase with B_1 and v is the part which is 90° out of phase. Differentiating eq (A2.10a) and substituting eqs (A2.8a) and (A2.8b), we get

$$\frac{du}{dt} = \frac{dM_x}{dt} \cos \omega t - M_x \omega \sin \omega t + \frac{dM_y}{dt} \sin \omega t + M_y \omega \cos \omega t$$

$$\frac{du}{dt} = \left[\gamma B_0 - \omega\right]\left[M_x \sin \omega t - M_y \cos \omega t\right] - \frac{M_x \cos \omega t + M_y \sin \omega t}{T_2}$$

$$\frac{du}{dt} = -\left[\omega - \gamma B_0\right] v - \frac{u}{T_2} \qquad \text{(A2.11a)}$$

Similarly, we obtain

$$\frac{dv}{dt} = \left[\omega - \gamma B_0\right] u - \frac{v}{T_2} + \gamma B_1 M_z \qquad \text{(A2.11b)}$$

$$\frac{dM_z}{dt} = -\gamma B_1 v + \frac{M_0 - M_z}{T_1}$$

(A2.11c)

Equations (A2.11) are the Bloch equations in the rotating coordinate frame.

Steady-State Solution

In a continuous wave (CW) magnetic resonance experiment, the radiation field B_1 is continuous and B_0 is changed only slowly (so-called ***slow passage*** conditions). Thus a steady-state solution to eqs (A2.11) is appropriate. Setting the derivatives to zero and solving the three simultaneous equations, we get:

$$u = \frac{\gamma B_1 M_0 (\omega_0 - \omega) T_2^2}{1 + T_2^2 (\omega_0 - \omega)^2 + \gamma^2 B_1^2 T_1 T_2}$$

(A2.12a)

$$v = \frac{\gamma B_1 M_0 T_2}{1 + T_2^2 (\omega_0 - \omega)^2 + \gamma^2 B_1^2 T_1 T_2}$$

(A2.12b)

$$M_z = \frac{M_0 \left[1 + T_2^2 (\omega_0 - \omega)^2\right]}{1 + T_2^2 (\omega_0 - \omega)^2 + \gamma^2 B_1^2 T_1 T_2}$$

(A2.12c)

where $\omega_0 = \gamma B_0$ is called the ***Larmor frequency*** and corresponds, in a quantum mechanical description of the experiment, to the (angular) frequency of the energy level transition.

Notice that as B_1 approaches zero, u and v go to zero and M_z approaches M_0, as expected. That is, it is the transverse oscillating field which causes the magnetization to have a nonequilibrium value. On the other hand, as B_1 increases, M_z decreases (moves away from equilibrium); u and v at first increase with increasing B_1, but eventually they decrease as the third term in the denominator begins to dominate.

Recall that u is the transverse magnetization component in-phase with the driving field B_1. In general a response which is exactly in phase with a driving signal does not absorb power from the signal source and in spectroscopy corresponds to ***dispersion***—in optical spectroscopy we are accustomed to thinking of dispersion as resulting from a small reduction of the speed of light as it traverses the medium but the problem can also be formulated so that optical dispersion is described in a way closely analogous to the Bloch equations description. An out-of-phase response, on the other hand, corresponds to ***absorption***. In magnetic resonance, it is usually the absorption mode which is detected and so we confine our attention to eq (A2.12b) in the following.

When the microwave or radio-frequency power, proportional to $B_1{}^2$, is small so that $\gamma^2 B_1{}^2 T_1 T_2 \ll 1$, eq (A2.12b) becomes

$$v = \frac{\gamma B_1 M_0 T_2}{1 + T_2^2(\omega_0 - \omega)^2}$$

(A2.13)

A plot of v *vs.* $T_2(\omega_0 - \omega)$ is shown in Figure A2. Equation (A2.13) corresponds to the classical *Lorentzian line shape* function and the absorption curve of Figure A2.1 is a Lorentzian "line". The half width at half height is easily found to be

$$\Delta\omega = 1/T_2 \quad \text{or} \quad \Delta v = 1/2\pi T_2 \quad \text{or} \quad \Delta B = h/2\pi g\mu_B T_2$$
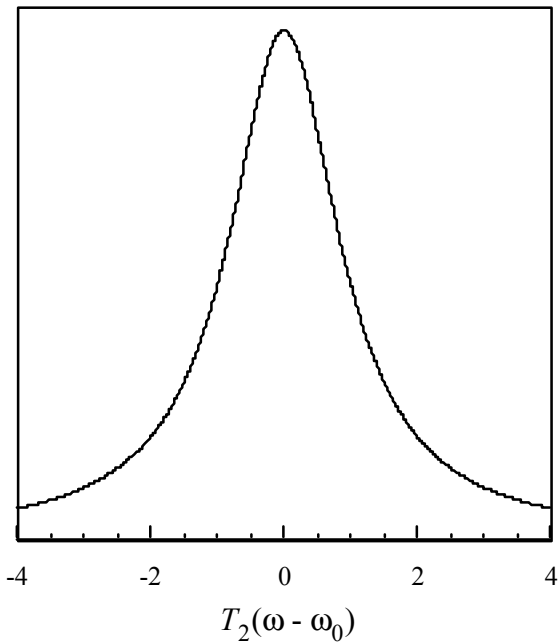

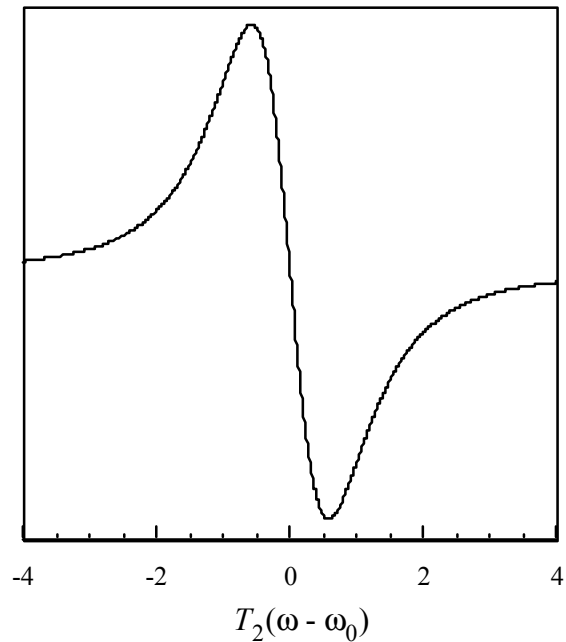**Figure A2.1.** A Lorentzian absorption line.

Figure A2.2. A Lorentzian first derivative line.

where the last form is appropriate when (as in ESR) B_0 is changed keeping ω constant.

When the absorption is detected via small amplitude field modulation, the signal is proportional to the first derivative of absorption,

$$\frac{dv}{d\omega} = \frac{2\gamma B_1 M_0 T_2^3(\omega_0 - \omega)}{\left[1 + T_2^2(\omega_0 - \omega)^2\right]^2}$$

(A2.14)

A Lorentzian derivative line is shown in Figure A2.2. In first derivative spectra, it is most convenient to describe the linewidth as the separation between derivative extrema. This width may be computed by taking the second derivative and finding the zeros, obtaining

$$\Delta\omega = \frac{2}{\sqrt{3}\,T_2} \quad \text{or} \quad \Delta\nu = \frac{1}{\sqrt{3}\,\check{s}\,T_2} \quad \text{or} \quad \Delta B = \frac{h}{\sqrt{3}\,\check{s}g\mu_B T_2}$$

The absorption derivative amplitude is proportional to $T_2{}^2$ whereas the width is proportional to $T_2{}^{-1}$. In other words, the derivative amplitude is inversely proportional to the square of the linewidth. Furthermore, the product of the amplitude and the square of the width is independent of T_2 and is sometimes taken as a measure of the intensity of the line, *i.e.*, proportional to M_0.

Notice that in the limit of small B_1 (where eqs (A2.13) and (A2.14) are valid), the derivative amplitude increases linearly with B_1, that the width is independent of B_1 and that neither width nor amplitude depends on T_1. At higher power, $\gamma^2 B_1{}^2 T_1 T_2$ can not be neglected in eq (A2.12b), the amplitude is no longer linear in B_1 and both amplitude and width depend on T_1. Eventually, the amplitude begins to decrease with increasing B_1 and we say that the resonance is **saturated**. In quantum mechanical language this corresponds to equalization of the energy level populations and reduction of net absorption.

Chemical Exchange – The Modified Bloch Equations

Suppose we have a system in which a spin can exist in either of two different sites A and B, and that these are distinguished by different resonant frequencies, ω_A and ω_B, and/or by different relaxation times, T_{2A} and T_{2B}. If there is no exchange between sites, site A spins and site B spins can be described separately and independently by sets of Bloch equations. When exchange takes place, however, additional rate terms—completely analogous to terms in chemical rate equations—must be added to the Bloch equations.

The algebra we are about to get into can be compacted somewhat by introducing the complex magnetization, $G = u + iv$, so that eqs (A2.11a) and (A2.11b) can be combined to obtain

$$\frac{dG}{dt} = \frac{du}{dt} + i\frac{dv}{dt} = -\frac{G}{T_2} + i(\omega_0 - \omega)G + i\gamma B_1 M_0$$

<div align="right">(A2.15)</div>

In eq (A2.15), we have ignored the difference between M_0 and M_z and so have assumed that B_1 is small.

Spins at site A will have magnetization G_A and those at site B will have magnetization G_B. We assume that A and B are interconverted by first-order kinetics with an A $\varnothing$ B rate constant $\tau_A{}^{-1}$ and a B $\varnothing$ A rate constant $\tau_B{}^{-1}$. The site A magnetization thus decreases with a rate term $-G_A/\tau_A$ and increases with rate G_B/τ_B. Combining these terms with eq (A2.15) for site A:

$$\frac{dG_A}{dt} = -\frac{G_A}{T_{2A}} - \frac{G_A}{\tau_A} + \frac{G_B}{\tau_B} + i(\omega_A - \omega)G_A + i\gamma B_1 M_{0A}$$

<div align="right">(A2.16a)</div>

and a similar expression for site B:

$$\frac{dG_B}{dt} = -\frac{G_B}{T_{2B}} + \frac{G_A}{\tau_A} - \frac{G_B}{\tau_B} + i(\omega_B - \omega)G_B + i\gamma B_1 M_{0B}$$

(A2.16b)

The rather fearsome algebra can be somewhat simplified by defining

$$\alpha_A = T_{2A}^{-1} - i(\omega_A - \omega)$$

$$\alpha_B = T_{2B}^{-1} - i(\omega_B - \omega)$$

and noting that, at chemical equilibrium,

$$p_A/p_B = \tau_A/\tau_B \quad \text{and} \quad p_A + p_B = 1$$

where p_A and p_B are the fractions of the population at sites A and B. Defining a mean lifetime

$$\tau = \frac{\tau_A \tau_B}{\tau_A + \tau_B}$$

several useful relations result:

$$p_A = \frac{\tau_A}{\tau_A + \tau_B} \quad p_B = \frac{\tau_B}{\tau_A + \tau_B}$$

$$\tau = p_A \tau_B = p_B \tau_A$$

Also, if M_0 is the total equilibrium magnetization, we can write

$$M_{0A} = p_A M_0 \quad M_{0B} = p_B M_0$$

With these relations, it is possible to find the steady-state solution to eqs (A2.16):

$$G = G_A + G_B = i\gamma B_1 M_0 \frac{\tau_A + \tau_B + \tau_A \tau_B \left(p_A \alpha_A + p_B \alpha_B \right)}{\left(1 + \tau_A \alpha_A\right)\left(1 + \tau_B \alpha_B\right) - 1}$$
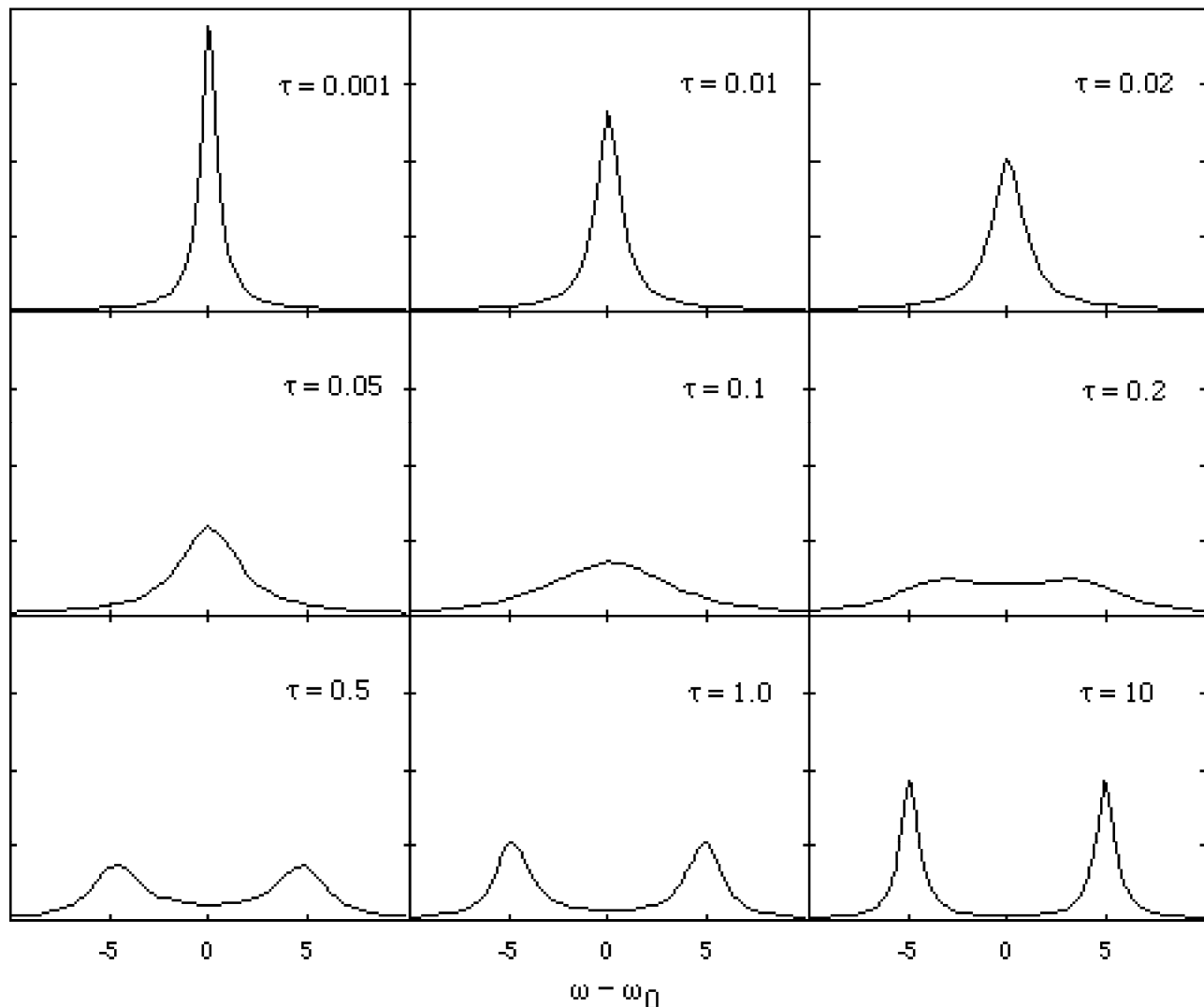
(A2.17)

Figure A2.3. Absorption curves, computed using eq (A2.17) for various values of τ, and $\omega_A = \omega_0 - 5$, $\omega_B = \omega_0 + 5$, $T_{2A}^{-1} = T_{2B}^{-1} = 0.5$, $p_A = p_B = 0.5$.

The absorption signal, of course, is the imaginary part of eq (A2.17); the equation is too horrible to contemplate, but computer-simulations, such as those shown in Figures A2.3 and A2.4, are relatively easy to produce. There are two limiting cases where the equations are easier to understand. In the ***slow exchange limit***, where τ_A^{-1} and τ_B^{-1} are both small compared with $|\omega_A - \omega_B|$, the absorption, $v = \mathrm{Im}(G)$, is

$$v = \frac{\gamma B_1 M_0 p_A \left(T_{2A}^{-1} + \tau_A^{-1}\right)}{\left(T_{2A}^{-1} + \tau_A^{-1}\right)^2 + \left(\omega_A - \omega\right)^2} + \frac{\gamma B_1 M_0 p_B \left(T_{2B}^{-1} + \tau_B^{-1}\right)}{\left(T_{2B}^{-1} + \tau_B^{-1}\right)^2 + \left(\omega_B - \omega\right)^2}$$

(A2.18)

which corresponds to two Lorentzian lines centered at ω_A and ω_B and with widths $(T_{2A}^{-1} + \tau_A^{-1})$ and $(T_{2B}^{-1} + \tau_B^{-1})$. In other words, the lines are unshifted but are broadened by an amount proportional to the reciprocal of the lifetimes.
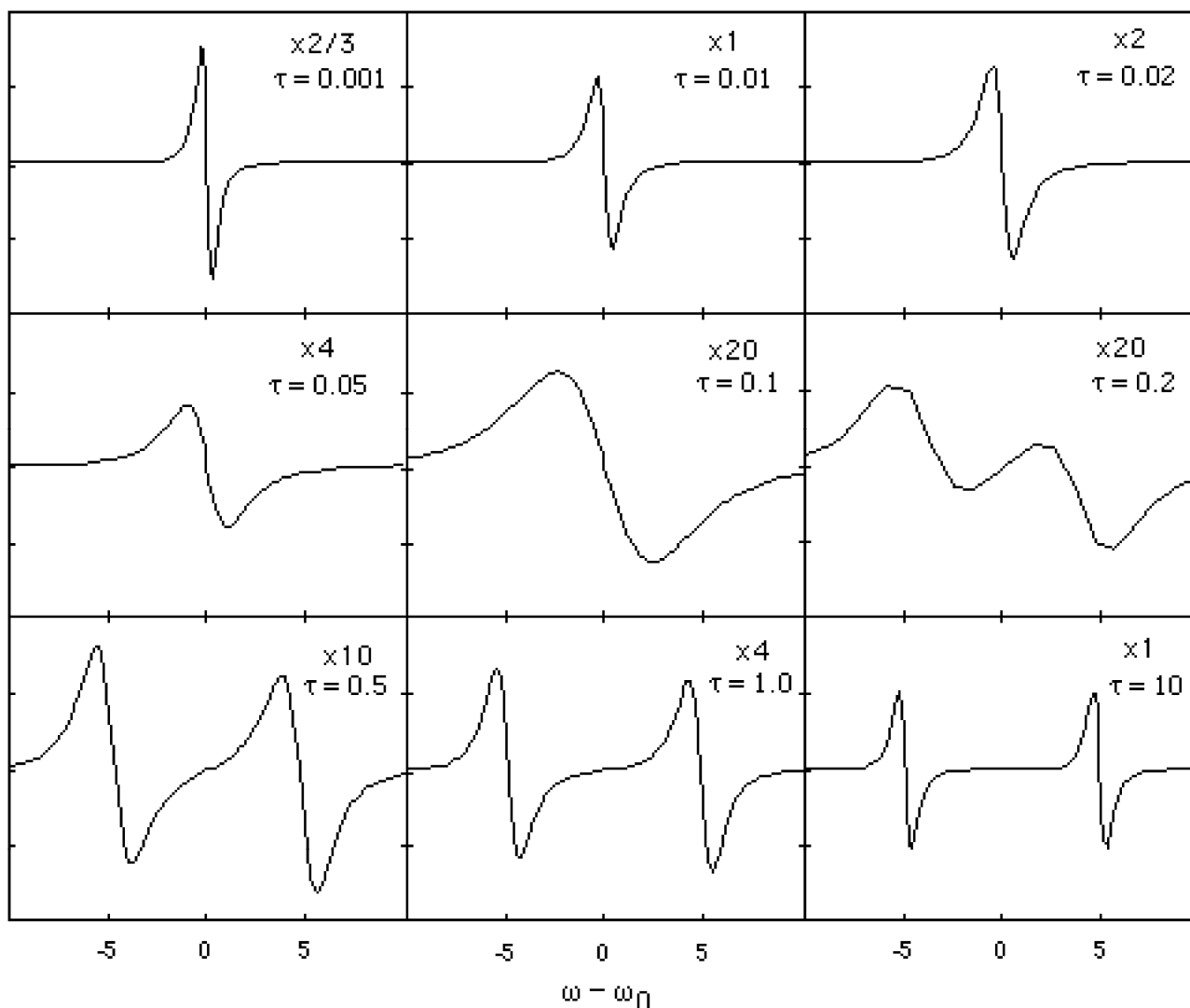
Figure A2.4. First-derivative curves, computed using eq (A2.17) for various values of τ, and $\omega_A = \omega_0 - 5$, $\omega_B = \omega_0 + 5$, $T_{2A}^{-1} = T_{2B}^{-1} = 0.5$, $p_A = p_B = 0.5$; note that the vertical scale differs—the plots are magnified by the factors shown.

In the ***fast exchange limit***, where τ_A^{-1} and τ_B^{-1} are both large compared with $|\omega_A - \omega_B|$, the absorption is

$$v = \frac{\gamma B_1 M_0 T_2^{-1}}{T_2^{-2} + (\omega_0 - \omega)^2} \qquad\qquad \text{(A2.19)}$$

where $\omega_0 = p_A \omega_A + p_B \omega_B$

$$T_2^{-1} = p_A T_{2A}^{-1} + p_B T_{2B}^{-1} + p_A p_B (\omega_A - \omega_B)^2 \tau$$

Thus a single Lorentzian line is obtained which is centered at a weighted average resonant frequency and has a width proportional to a weighted average T_2^{-1} plus a term proportional to the average lifetime and the square of the separation of the slow exchange resonances.

In the so-called intermediate exchange region, eq (A2.17) is not easily tractable and recourse is usually made to computer simulations. Qualitatively, however, it is clear that as the rate increases, the separate resonances of the slow exchange limit broaden, shift together, coalesce and then begin to sharpen into the single line of the fast exchange limit.

Further Discussion of Line Shapes

Lorentzian line shapes are expected in magnetic resonance spectra whenever the Bloch phenomenological model is applicable, *i.e.*, when the loss of magnetization phase coherence in the *xy*-plane is a first-order process. As we have seen, a chemical reaction meets this criterion, but so do a number of other line broadening mechanisms such as averaging of the *g*- and hyperfine matrix anisotropies through molecular tumbling (rotational diffusion) in solution.

There are some sources of line broadening which can not be thought of as first-order rate processes. For example, when the magnetic field is inhomogeneous and varies over the sample, not all the molecules are at resonance at the same nominal field. It is usually reasonable to guess that the field has a ***Gaussian*** distribution (*i.e.*, a normal error distribution), so that the resonance line will also have a Gaussian shape. A variety of other effects can lead to ***inhomogeneous broadening*** and thus to Gaussian line shapes. For example, the instantaneous chemical environment may vary from one radical to another because of different degrees of solvation or ion pairing. Probably for such reasons, Gaussian line shapes are commonly observed in frozen solution ESR spectra. Unresolved hyperfine couplings often give a resonance line an approximately Gaussian shape.

The Gaussian line shape function can be written

$$S(\omega) = e^{-(\omega - \omega_0)^2/2\delta^2}$$

(A2.20)

so that the half-width at half-height is

$$\text{Half width} = \sqrt{2 \ln 2}\, \delta = 0.980\, \delta$$

and the derivative width (between extrema) is exactly 2δ.

A Gaussian line and its first derivative are shown in Figures A2.5 and A2.6. Comparison with Figures A2.1 and A2.2 shows that the Gaussian line is somewhat fatter near the middle but lacks the broad wings of the Lorentzian line.
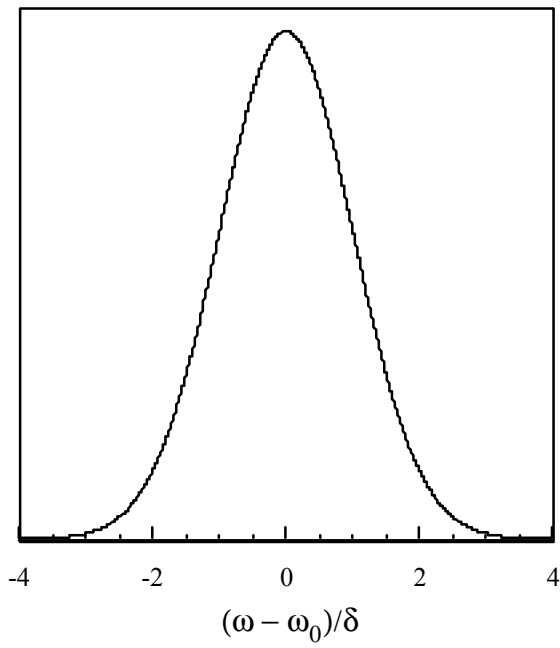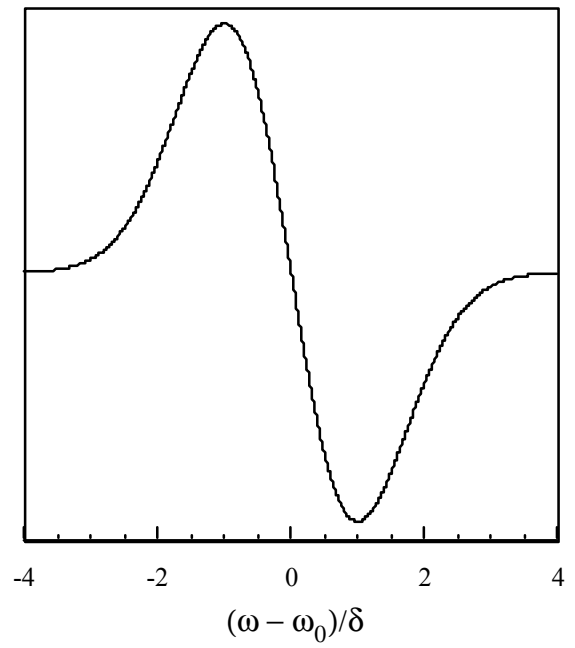
Figure A2.5. Gaussian absorption line. **Figure A2.6**. First-derivative Gaussian line.

Appendix 4

<u>Interpretation of Isotropic ESR Spectra</u>

The interpretation of an isotropic ESR spectrum is relatively straightforward if a systematic approach is used, but it can be a frustrating experience for a beginner. In these notes, an attempt has been made to give a series of steps which, if followed with care, will result in a succesful interpretation for most reasonably well resolved spectra.

Preliminary Examination of the Spectrum

A. Check to see if the spectrum is symmetric in line positions and relative intensities. If it isn't, then most likely there are two or more radical species. Variation of linewidths with m_i may cause the spectrum to appear unsymmetric, but in such a case line positions would still be at least approximately symmetrically distributed about the center.

B. Is there a central line? If there is no central line, then there must be an even number of lines which suggests an odd number of half integral nuclei (*i.e.*, I = 1/2, 3/2, etc.).

C. Are the outermost lines visible above the noise? Observation of the wing lines is often crucial to successful interpretation of ESR spectra. In noisy spectra, it is sometimes difficult to tell if all the lines are actually observed in the wings.

D. How many lines are there? Count them carefully, watching for evidence of unresolved features (shoulders or bumps).

E. What is the ratio of the amplitudes of the biggest to smallest lines in the spectrum?

What do you Expect to See?

A. If the radical was produced by a chemically straightforward procedure, you usually have some idea of the identity of the radical. How many and what kinds of paramagentic nuclei are present?

B. How many lines are expected from this model? The total number of nuclear spin states is $(2I_1+1)\infty(2I_2+1)\infty(2I_3+1)...$ Thus if the model structure has six protons ($I = 1/2$), there should be $(2\infty1/2 + 1)^6 = 2^6 = 64$ nuclear spin states. If some of the nuclei are expected to be equivalent, then the number of lines will be less than the number of spin states, *i.e.*, some of the spin states will be degenerate (to first-order in perturbation theory). Thus if the six protons are in three groups of two, it is as if you had three spin 1 nuclei and you expect $(2\infty1 + 1)^3 = 3^3 = 27$ lines. If there is one group of four equivalent protons and another group of two, then it is as if you had one spin 2 nucleus and one spin 1 nucleus and you expect $(2\infty2 + 1)(2\infty1 + 1) = 15$ lines.

C. What is the expected ratio of intensities of the biggest to smallest line? If all the nuclei are inequivalent, then all lines should have the same intensity (barring accidental superpositions). If there are equivalent sets of nuclei, then the expected ratio is the product of the biggest-to-smallest ratios of the various multiplets. Thus for the above examples, three groups of two spin 1/2 nuclei gives a 1:2:1 triplet of 1:2:1 triplets of 1:2:1 triplets; thus the maximum intensity ratio of $2\infty2\infty2 = 8$. If we have a 1:4:6:4:1 quintet of 1:2:1 triplets, then the maximum intensity ratio will be $6\infty2 = 12$.

Are the Gross Features Consistent with the Model?

A. Compare the number of observed lines with the number expected. If there are more lines than expected, either the model is wrong or there is more than one radical. If the expected and observed numbers are equal, you are in luck—the analysis should be easy. If you see fewer lines than expected (the most common case!), there may be accidental superpositions, small amplitude lines buried under big ones, or just poor resolution. The bigger the discrepancy between expected and observed numbers of lines, the harder the analysis will be.

B. Compare the expected and observed biggest-to-smallest intensity ratios. Accidental degeneracies (or a m_I^2 linewidth dependence) may cause the observed ratio to be bigger than expected. It is rarer (but not unknown) to find a smaller ratio than expected.

C. Is the presence or absence of a central line consistent with the odd or even number of expected lines?

D. If the model still seems plausible after these tests, go on to a detailed analysis. If there are gross inconsistences, the model is probably wrong.

Detailed Analysis

A. Measure the positions and amplitudes of all the lines in the spectrum and list them in order in a table. If convenient, measure the line positions in gauss; if this is inconvenient, use arbitrary units such as inches, centimeters, or recorder chart boxes measured from an arbitrary zero. In your table, provide headings for each of the quantum numbers (m_1, m_2, etc.), for each of the coupling constants (a_1, a_2, etc.), and for the theoretical intensity (degeneracy).

B. The highest and lowest field lines will always have theoretical intensities of 1 and will have minimum or maximum values for all the quantum numbers. It doesn't really matter whether you start with maximum quantum numbers at the high-field or low-field end of the spectrum—the signs of the coupling constants are indeterminant—but for consistency, let's agree to assign maximum quantum numbers to the lowest field line (*i.e.*, pretend that the coupling constants are positive). Enter these assignments in the table. From this point on, you can work from either end of the spectrum or even from both at once. In the following, we assume that we're working from the low-field end.

C. The spacing between the first and second lines will be the smallest coupling constant, a_1. The intensity ratio of these two lines will usually indicate the multiplet to which the coupling constant corresponds. Assign quantum numbers to the second line, compute a_1 and enter these numbers in the table. If you have started into a muliplet, you can then predict the positions and intensities of the remaining lines of the muliplet. Find them and enter the quantum numbers and new estimates of a_1 in the table.

D. After finding all the lines of the first a_1 multiplet, find the first unassigned line. This must correspond to the next larger coupling constant a_2. From the ratio of its amplitude to that of the end line, you can usually figure out which multiplet this coupling constant corresponds to. Assign the quantum numbers and compute the coupling constant a_2. Enter in the table. This line will also correspond to the first line in a second a_1 multiplet, and, knowing a_1, you can predict the positions and intensities of the remaining lines of this multiplet. Find them and enter the quantum number assignments and new estimates of a_1 and a_2 in the table.

E. If a_2 corresponds to a multiplet, the positions of the remaining lines can predicted and located. Continue in this way through the spectrum. Small discrepances may arise through measurement errors or because of overlapped lines. A position discrepancy larger than your estimated measurement accuracy, however, may signal a misassignment or inconsistency with the model. Notice that the spacing between the lowest and highest field lines is equal to the sum of the

coupling constants. Thus if you have found two coupling constants and know the total extent of the spectrum, you can compute the sum of the remaining couplings.

   F. When all the lines have been assigned, average all the measured values of each coupling constant and compute the standard deviation. If an arbitrary position scale was used, convert the coupling constant to gauss. [Note: a least-squares fit of line positions to quantum numbers gives better statistics than this method, but it is impossibly tedious to do by hand in all but the simplest cases.]

Computation of Multiplet Intensity Ratios

   For sets of spin 1/2 nuclei, the multiplet intensity ratios are simply the binomial coefficients found most easily from Pascal's triangle:


```
1
                              1      1
                          1      2      1
                       1      3      3      1
                    1      4      6      4      1
                 1      5     10     10      5      1
              1      6     15     20     15      6      1
           1      7     21     35     35     21      7      1
        1      8     28     56     70     56     28      8      1
```


The spectrum of the naphthalene anion radical, for example, consists of a quintet of quintets, arising from coupling of the four equivalent α-protons and the four equivalent β-protons, as shown in the Figure A7.
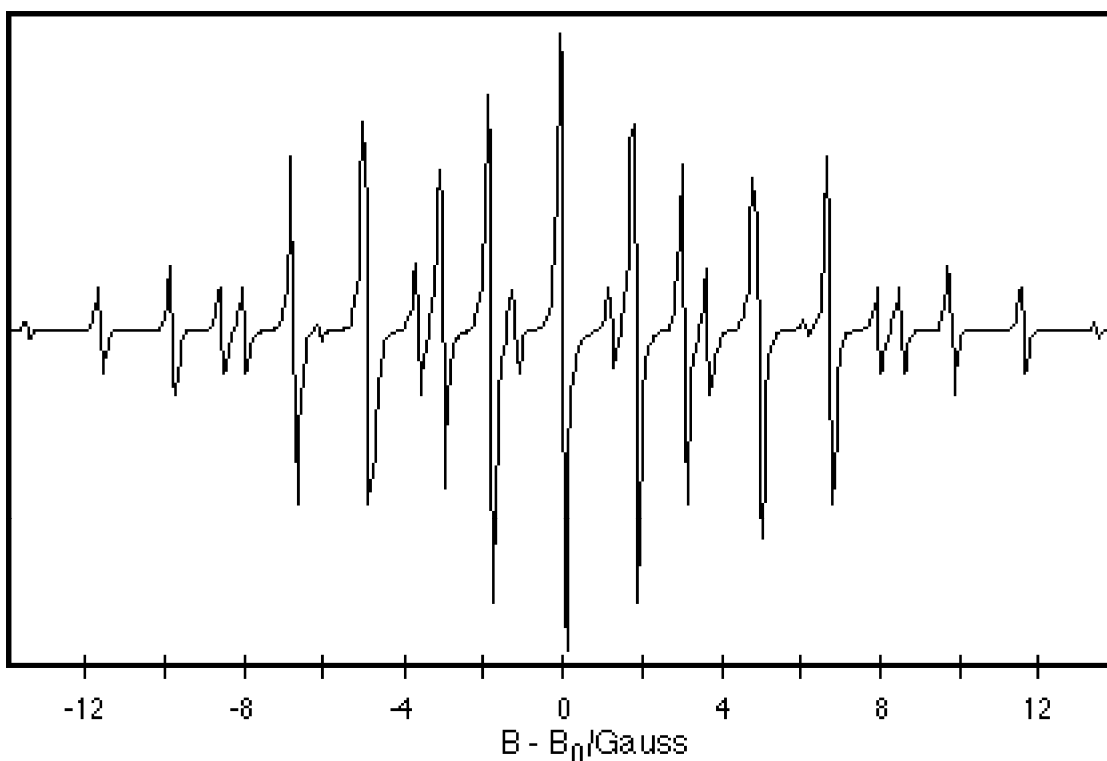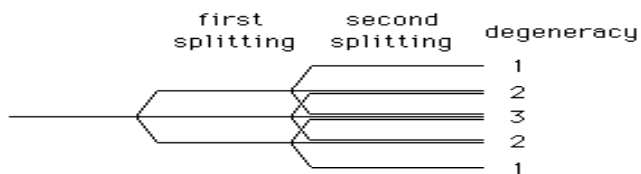
Figure A7. Computer-reconstruction of the ESR spectrum of the naphthalene anion radical.

For higher spin nuclei, one can construct a splitting diagram. For example, for two spin 1 nuclei:

This procedure quickly gets out of hand, however, and a more compact notation is preferable. Thus if we think of each of the three lines resulting from coupling to the first spin 1 nucleus split into a 1:1:1 triplet, we have:

1	1	1			
	1	1	1		
		1	1	1	
Add:	1	2	3	2	1

This procedure can be extended to three spin 1 nuclei by thinking of each line of a 1:1:1 triplet split into a 1:2:3:2:1 quintet:

1	2	3	2	1			
	1	2	3	2	1		
		1	2	3	2	1	
Add:	1	3	6	7	6	3	1

For really complicated situations, this method can be used as the basis for a computer algorithm.

Multiplet Patterns due to Isotopomers

We often encounter cases where an element has one or more isotopes with a nuclear spin and one or more isotopes with zero spin. The most common example is that of carbon where 1.1% of naturally occuring carbon is ^{13}C with $I = 1/2$ and 98.9% is ^{12}C with $I = 0$. Thus in a carbon-containing radical, the probability that any given carbon is ^{13}C is 0.011. Suppose that there are n equivalent carbon atoms in the radical. The probability that all n will be ^{12}C is $(0.989)^n$. The probability that one specific carbon is ^{13}C and the other $n-1$ ^{12}C will be $(0.011)(0.989)^{n-1}$, but, since any one of the n carbons could be ^{13}C, we see that the total probability of finding one ^{13}C is $n(0.011)(0.989)^{n-1}$. Similarly the probability that two specific carbons are ^{13}C is $(0.011)^2(0.989)^{n-2}$, but any one of the n carbons could be ^{13}C and any of the $n-1$ remaining carbons could also be ^{13}C, so that the total probability of having two ^{13}C's is $n(n-1)(0.011)^2(0.989)^{n-2}$. On reflection, we see that the coefficients 1, n, $n(n-1)$, are just binomial coefficients and that the probabilities of finding 0, 1, 2, etc., ^{13}C's out of n equivalent carbon atoms are just the terms in the expansion of the expression:

$$(0.989 + 0.011)^n = (0.989)^n + n(0.989)^{n-1}(0.011) + n(n-1)(0.989)^{n-2}(0.011)^2 + ...$$

For example, in a radical with six equivalent carbon atoms (*e.g.*, benzene anion radical), the probabilities are: $P_0 = 0.936$, $P_1 = 0.062$, $P_2 = 0.0035$, $P_3 = 0.00015$, etc. In practice, we would probably see the central line with intensity 0.936 and a pair of satellites with intensity 0.031 (the intensity is distributed between the two resonances).

More complex patterns can arise from atoms with a higher fraction of magnetic isotopes. Consider the case of a radical species with three equivalent platinum atoms. ^{195}Pt has $I = 1/2$ and is 33.8% in natural abundance. Other Pt isotopes have $I = 0$. Thus the probabilities are: $P_0 = 0.290$, $P_1 = 0.444$, $P_2 = 0.227$, and $P_3 = 0.039$. These four isotopomers will result, respectively, in a singlet, a doublet, a 1:2:1 triplet, and a 1:3:3:1 quartet. However, since the platinum atoms are assumed to be equivalent, the coupling constant will be the same in each pattern and there will be some superpositions. Thus seven hyperfine components are expected with positions and intensities as shown:
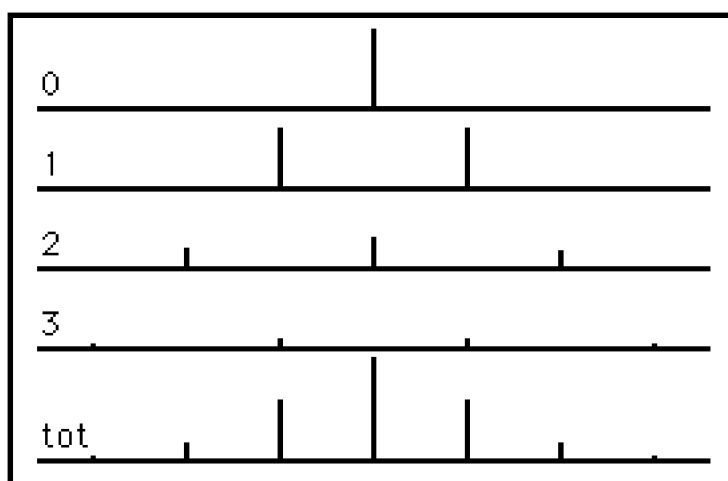
The relative intensities of the seven-line pattern then is expected to be approximately: 1:12:49:84:49:12:1. With luck, all seven lines might be observable. Patterns like this are more complicated to analyse, but they also provide a fingerprint identifying the number of equivalent nuclei involved in the multiplet pattern.

Second-Order Shifts in Line Positions

Our analysis thus far has assumed that solution of the spin Hamiltonian to first order in perturbation theory will suffice. This is often adequate, especially for spectra of organic radicals, but when coupling constants are large (greater than about 20 gauss) or when linewidths are small (so that line positions can be very accurately measured) second-order effects become important. For a single nucleus with nuclear spin I, the hyperfine line positions are given to second order in perturbation theory by:

$$B = B_0 - \langle a \rangle m_I - \frac{\langle a \rangle^2}{2B_0}\left[I(I+1) - m_I^2\right]$$

Thus, for example, a spin 1 nucleus with $\langle a \rangle$ = 20 G and B_0 = 3200 G will have lines at:

B = 3200 − 20(+1) − (0.0625)(2 − 1) = 3179.94 G

B = 3200 − 20(0) − (0.0625)(2 − 0) = 3199.88 G

B = 3200 − 20(−1) − (0.0625)(2 − 1) = 3219.94 G

so that the line spacings are, respectively, 19.94 and 20.06 G, and the spectrum as a whole is shifted to low field (relative to the first-order result) by 0.08 G. This is a rather small effect and would require careful measurements to notice. When $\langle a \rangle$ is larger, the shifts are much more noticeable. Thus, for example, when $\langle a \rangle$ = 100 G, the line spacings become 98.44 and 101.56 G, a much more easily noticable discrepancy.

When a spectrum results from coupling to several equivalent nuclei with couplings large enough to warrant second-order corrections, the situation becomes somewhat more complicated since we must then think of the total nuclear spin J and its components m_J. The second-order corrections then depend on J rather than the individual I's. Thus, for example, two equivalent spin 1 nuclei will give rise to a $J = 2$ state with $m_J = \pm2, \pm1$, and 0. There is only one way of getting $m_J = \pm2$ (each nucleus has $m_I = \pm1$), but there are two ways of getting $m_J = \pm1$ (either of the nuclei can have $m_I = 0$ and the other $m_I = \pm1$), so there must also be a $J = 1$ state with $m_J = \pm1$ and 0. There are three ways of getting a $m_J = 0$ state (either of the nuclei can have $m_I = \pm1$ and the other $m_I = \mp1$ or both nuclei can have $m_I = 0$); thus there must be a $J = 0$ state with $m_J = 0$. Thus, to second-order, the degeneracies of the 1:2:3:2:1 multiplet pattern are lifted. Summarizing these results, we have, for B_0 = 3200 G, $\langle a \rangle$ = 20 G:

m_J	J	$[J(J+1) - m_J^2]/2$	B
2	2	1	3159.88
1	2	5/2	3179.69
	1	1/2	3179.94
0	2	3	3199.62
	1	1	3199.88
	0	0	3200.00
−1	2	5/2	3219.69
	1	1/2	3219.94
−2	2	1	3239.88